UNIVERSIDADE FEDERAL DO CEARÁ

TECHNOLOGY CENTER

DEPARTMENT OF METALLURGICAL AND MATERIALS ENGINEERING

POSTGRADUATE PROGRAM IN MATERIALS SCIENCES AND ENGINEERING

DOCTORAL COURSE IN MATERIALS SCIENCE AND ENGINEERING

YURI CRUZ DA SILVA

MODELING AND SIMULATING OF STAINLESS STEEL JOINTS BY FRICTION STIR WELDING

FORTALEZA

2021

YURI CRUZ DA SILVA

MODELING AND SIMULATING OF STAINLESS STEEL JOINTS BY FRICTION STIR WELDING

> Thesis Submitted to Postgraduate Program in Materials Sciences and Engineering at the Technology Center of the Universidade Federal do Ceará, in partial fulfillment of the requirements for the Degree of Doctor in Materials Sciences and Engineering. Concentration Area: Physical Properties and Mechanics of Materials
>
> Advisor: Prof. Dr. Cleiton Carvalho Silva
>
> Co-Advisor: Prof. Dr. Francisco Marcondes

FORTALEZA

2021

YURI CRUZ DA SILVA

MODELING AND SIMULATING OF STAINLESS STEEL JOINTS BY FRICTION STIR WELDING

Thesis Submitted to Postgraduate Program in Materials Sciences and Engineering at the Technology Center of the Universidade Federal do Ceará, in partial fulfillment of the requirements for the Degree of Doctor in Materials Sciences and Engineering. Concentration Area: Physical Properties and Mechanics of Materials

Approved on:

EXAMINATION BOARD

—————————————————————
Prof. Dr. Cleiton Carvalho Silva   (Advisor)
Universidade Federal do Ceará (UFC)

—————————————————————
Prof. Dr. Francisco Marcondes   (Co-Advisor)
Universidade Federal do Ceará (UFC)

—————————————————————
Hélio Cordeiro de Miranda
Universidade Federal do Ceará (UFC)

—————————————————————
Prof. Dr. Jorge F. dos Santos
Helmholtz-Zentrum Geesthacht (HZG)

—————————————————————
Prof. Dr. José Antônio Esmerio Mazzaferro
Universidade Federal do Rio Grande do Sul
(UFRGS)

ACKNOWLEDGEMENTS

ABSTRACT

Friction Stir Welding (FSW) is a solid-state welding method developed 1991 at The Welding Institute (TWI). This method joins materials through plastic deformation caused by a rotational tool that moves between the materials interface. The scientific community has extensively studied this technique because its unique characteristics allow excellent results compared with conventional fusion welding processes. The low temperatures and high deformation rates during the process favor the existence of the dynamic recrystallization of the grains, improving the welded region mechanical properties. Numerical simulations were performed to understand the phenomena that involve the FSW joining of the AISI 304L and the AISI 410S steels. For this, this thesis was divided into four chapters. The Chapter 5 addressed the viscosity models used in this study and developed a methodology to determine the maximum viscosity to be defined in the simulation. Following the thesis, which comprises three more chapters, the next two have addressed the FSW process simulation applied for two different stainless steels: AISI 304L and AISI 410S. Theses steels ware chosen for their applicability in the industry. The materials were simulated as non-Newtonian fluids, where their viscosity depends on the process temperature and the strain rate. In the Chapter 6, a simulation was made for the similar welding of AISI 304L austenitic stainless steel, making it possible to calculate the extent of the welding zones. A parameter Y was also developed, depending on the minimum viscosity, applied pressure, and rotation. This parameter assists in the choice of conditions with less possibility of burr formation. Particles were injected into the model in order to trace its path along with the plate, and from that, we predict regions where defects of the wormhole type would be formed. Chapter 7 focus was on using the simulated temperature, which presented results very close to the experimental ones and associating it with thermodynamic simulations. In this study, it was possible to predict the formation of martensite and chromium carbides ($Cr_{23}C_6$) in different regions of the weld. The parameter Y was applied to this material, and its effectiveness was observed in all experimental tests, predicting the conditions with more burrs. In the Chapter 8, the Volume of Fluid (VOF) method was applied to the FSW simulation model already used to simulate the mixture of these materials in dissimilar welding and made it possible to observe the materials flow during the welding, and which side each material should be employed to obtain the best results. In this chapter, the simulation with a more realistic model of the tool was also developed, enabling the development of future works in the area.

RESUMO

Friction Stir Welding (FSW) é um método de soldagem de estado sólido desenvolvido em 1991 no The Welding Institute (TWI). Este método une materiais por meio de deformação plástica causada por uma ferramenta rotacional que se move entre a interface dos materiais. A comunidade científica tem estudado extensivamente esta técnica porque suas características únicas permitem excelentes resultados em comparação com os processos convencionais de soldagem por fusão. As baixas temperaturas e as altas taxas de deformação durante o processo favorecem a existência da recristalização dinâmica dos grãos, melhorando as propriedades mecânicas da região soldada. Simulações numéricas foram realizadas para entender os fenômenos que envolvem a união FSW dos aços AISI 304L e AISI 410S. Para isso, esta tese foi dividida em 4 capítulos. O Capítulo 5 abordou os modelos de viscosidade utilizados neste estudo e desenvolveu uma metodologia para determinar a viscosidade máxima a ser definida na simulação. Na sequência da tese, que compreende mais três capítulos, os dois seguintes abordaram a simulação do processo FSW aplicada a dois aços inoxidáveis diferentes: AISI 304L e AISI 410S. Estes aços foram escolhidos por sua aplicabilidade na indústria. Os materiais foram simulados como fluidos não newtonianos, onde sua viscosidade depende da temperatura do processo e da taxa de deformação. No Capítulo 6, foi feita uma simulação para a soldagem similar do aço inoxidável austenítico AISI 304L, possibilitando o cálculo da extensão das zonas de soldagem. Um parâmetro Y também foi desenvolvido, dependendo da viscosidade mínima, pressão aplicada e rotação. Este parâmetro auxilia na escolha de condições com menor possibilidade de formação de rebarbas. Partículas foram injetadas no modelo a fim de traçar seu caminho junto com a placa e a partir disso, prevemos regiões onde seriam formados defeitos do tipo buraco de minhoca. O Capítulo 7 focou no uso da temperatura simulada, que apresentou resultados muito próximos aos experimentais, associada à simulações termodinâmicas. Neste estudo, foi possível prever a formação de martensita e carbonetos de cromo ($Cr_{23}C_6$) em diferentes regiões da solda. O parâmetro Y foi aplicado a este material, e sua eficácia foi observada em todos os testes experimentais, prevendo as condições com mais rebarbas. No Capítulo 8, o método Volume of Fluid (VOF) foi aplicado ao modelo de simulação FSW já utilizado para simular a mistura desses materiais em soldagens dissimilares e possibilitou observar o fluxo dos materiais durante a soldagem e de que lado cada material deve ser empregado para obter os melhores resultados. Neste artigo também foi desenvolvida a simulação com um modelo mais realista da ferramenta, possibilitando o desenvolvimento de futuros trabalhos na área.

Palavras-chave: Friction Stir Welding. Volume of Fluid. Aços inoxidáveis. Soldagem Dissimilar. Simulação numérica

LISTA DE FIGURAS

LIST OF TABLES

LIST OF SYMBOLS

ρ	Density
P	Pressure
μ	Viscosity
U	Weld velocity
T	Temperature
C_p	Specific heat
k	Thermal conductivity
S_i	Source term per unit of volume generated by friction
S_b	Source term per unit of volume generated by plastic deformation
σ_e	Flow stress
σ_p	Flow stress by plastic contributions
σ_v	Flow stress by viscous contributions
$\dot{\varepsilon}$	Strain rate
Z	Zener–Hollomon parameter
α	material constants
R	universal gas constant
Q	temperature-independent activation energy
A_r	Contact area between the tool and workpiece
q_1	heat generated
V	Tensão
δ	Proportion between the heat generated by deformation and friction.
η	Thermal efficient
μ_f	Friction coefficient
r	Radius
R_s	Shoulder Radius
R_p	Pin radius

R_p	Pin radius
h_b	Heat convection coefficients for bottom
h_t	Heat convection coefficients for top
h_s	Heat convection coefficients for sides
T_a	Environment temperature
σ	Boltzmann constant

CONTENTS

1 INTRODUCTION

The Friction stir weld (FSW) is a solid-state welding process developed by The Weld Institute(TWI) in 1991. This process joints the materials through a rotational tool, which penetrates and translates between the material interface. The tool heats and deforms the material, causing its joining by plastic deformation associated with forging.

This process has been considered a significant advance in welding materials, where FSW is a scientific hot spot in materials joining and manufacturing processes due to its broad applicability and performance. FSW has allowed joining materials that were not possible or had difficulties to be welded by traditional fusion welding methods, as aluminum and its alloys (LOMOLINO *et al.*, 2005; BATISTÃO *et al.*, 2020; FERREIRA *et al.*, 2020). Initially, the FSW process has been developed and was widely used for aluminum welding. However, with the intense development of the tool materials and the evolution in the tools' design, this process has been used for welding high melting point metals and alloys, as steels, titanium alloys, nickel-based alloys and there are already studies of joining metallic with non-metallic materials.

Another great advantage of the FSW process is the maximum welding temperature reached that it is lower than the melting temperature. Besides, the movement of the tool can cause dynamic recrystallization. The dynamic recrystallization phenomenon is responsible for promoting an intense grain refinement the welded region for some materials. This mechanism allows increase the grain boundary density, which serves as a barrier for dislocation motion, resulting in an increment in strength, hardness and fracture toughness. which are desired properties for welded components.

Due to the great innovations provided by friction stir welding, the demand for this process has intensified in recent years, intending to provide materials welding solutions for several industry sectors, such as aeronautics, aerospace, nuclear, automotive, oil & gas, and others. Despite the many qualities of the process, it is still very new, and for a better understanding of the physical and metallurgical phenomena involved, the scientific community has been developing techniques to simulate FSW welding. However, heating coupling with materials flow makes the processing by FSW technology highly complex, being essential to understanding various phenomena involved to provide advances in the joined materials performance and in their applications.

Observing this technique's great potential, the *Laboratório de Pesquisa e Tecnologia em Soldagem* (LPTS) in Brazil, in cooperation with the *Helmholtz-Zentrum Geesthacht institute*

(HZG) in Germany, has developed a research project aiming to investigate the similar and dissimilar welding of austenitic and ferritic stainless steels by FSW. The reason for choosing these steels is due to many applications in a wide variety of industries, as the household industry; heavy manufacturing industries such as chemical transportation wagon and passenger wagon; or for construction of processing equipment used in chemical, petrochemical and oil & gas facilities, due to balance between good corrosion resistance for several chemicals combined with good mechanical properties.

The present thesis evaluates the FSW process from the fluid mechanics' point of view, in which the viscosity of the solid material varies with the temperature and the strain rate during the process. This method has been used in the literature to simulate different materials, such as steels, aluminum alloys, titanium alloys, etc. The analysis of the materials' properties allows predicting defects and a better selection of welding parameters, consequently reducing the cost and the service time. The simulations developed in this thesis allowed the prediction of defects, where a parameter was developed to help the best conditions concerning the formation of flashes and voids. The temperatures calculated in conjunction with thermodynamic simulations predicted the phases and regions formed after the simulation. In addition to all the predicted conditions and properties, the fluid volume method (VOF) made it possible to analyze the mixture between the materials in dissimilar welding.

2 OBJECTIVES

This study aims to understand the phenomena involved in the similar and dissimilar welding of AISI 410S ferritic stainless steel and AISI 304L austenitic stainless steel by friction stir welding, using computational tools to predict defects associated with temperature, fluid flow and viscosity change, allowing better choice and control of the welding parameters. Besides the prediction of defects, the simulation can help predict the possible phase transformations and resulting microstructure, helping in best choice of processing parameters to obtain the desired microstructure.

2.1 Specific Objectives

- Evaluate the viscosity models and understand their behavior and the necessary parameters for the simulation.
- Simulate the FSW in AISI 304L stainless steel, predicting the process temperatures and their consequences on the final welding result.
- Predict the possible defect formation in AISI 304L stainless steel during FSW welding as a function of welding parameters from numerical analysis and establish a correlation factor associated with the tendency of defect occurrence.
- Simulate the thermal cycle during the welding of the AISI 410S stainless steel and associate it with the possible phase transformations that occurred in the stir zone, thermomechanical affected zone and heat affected zone.
- Verify the formation of defects in AISI 410S stainless steel from methodology applied on AISI 304L stainless steel, in order to verify its reproducibility in differents materials.
- Simulate dissimilar welding between AISI 304L and AISI 410S stainless steels and predict the correct joint position of each material, and to evaluate the effect of the leading welding parameters: rotational speed, axial force, and translation speed, on the temperature, fluid flow, and viscosity, to ensure enough quality to the welds.

3 THESIS ORGANIZATION

This thesis was split into five main topics, aiming to complete the proposed objectives and fulfill all requirements as part of the doctorate's requisites in Materials Science and Engineering.

The first topic (Chapter 4) is a comprehensive review of the literature, which was performed aiming to cover metallurgical aspects of the materials to be studied, an overview of the FSW process, including general aspects, the main welding parameters, and the tools, a brief comment on different kinds of weld defects and their relationship with the procedure and parameters. Finally, the state of the art on the numerical simulation applied to understanding the friction stir welding phenomena.

The second topic (Chapter 5) was an analysis to understand the viscosity models already used in numerical simulations. All these models have been developed on the dependence of the change in the material's viscosity with temperature and strain rate. However, each material has specific constants and adaptations to fit the equations. Therefore, an extensive literature review has been performed to identify all needed data to the numerical simulation, applied in the viscosity model, and observed how the viscosity functions behave for low values of temperature and strain rates.

It has been observed that the maximum viscosity value was essential to reach good results. Many authors cited the maximum value reached for viscosity on the stir zone. However, none of them has clearly described the values set in the code and their influence on the welded joint response determined by the numerical simulation. To fulfill this gap, Chapter 5 propose a methodology to choose the value of the viscosity.

With the benchmark done, the next step was to apply this numerical simulation for similar welded joints. Therefore, the third topic, Chapter 6, consisted of using the previous model on the simulation for AISI 304L austenitic stainless steel welded by FSW process. The purpose was to understand the influence of the leading welding parameters: rotation speed, axial force, and welding velocity on the tendency to produce weld defects. The results have shown that it is possible to predict the formation of flashes and wormholes in welding.

In the fourth topic (Chapter 7), the model has been applied to evaluate another material, the AISI 410S ferritic stainless steel, also highlighting the influence of the FSW parameters on the heat generation, temperature profile, materials flow, and viscosity. Besides, based on the steel's chemical composition and using a thermodynamic calculation package, the

phase diagram was simulated and used to predict the phase transformations during the welding.

The fifth and last topic (Chapter 8) could be run after the model validation for each steel to be concluded. These previous studies allowed a clear understanding of all aspects of each material's behavior, providing the needed information to advance for a more complicated condition involving a dissimilar welding configuration.

Thus, Chapter 8 has as the main contribution an approach applied to evaluate the models for each alloy, applying the Volume of Fluid (VOF) method. This particular study introduced a more complex geometry of tool that described the real geometry and dimensions of the PCBN tool used in the experimental tests. The equations for the speed applied to the tool contact with the weld material were also rewritten. In this chapter, we consolidated the knowledge of previous chapters.

Finally, the conclusions were listed in Chapter 9. This thesis encourages future works with improvements to more realistic tool geometries and mixture models.

4 LITERATURE REVIEW

4.1 Stainless Steels

Stainless steels are a class of iron alloys with excellent corrosion resistance, which may be combined with good mechanical properties depending on their matrix phase. The chromium is the key element in this case, responsible to produce an very thin, adhered, impermeable, and inert layer formed by chromium oxide (Cr_2O_3). This corrosion resistance is reached when chromium is added as an alloying element in amount greater than 10.5 wt.% (LIPPOLD; KOTECKI, 2005). This element creates a protection layer on iron by formation a surface chromium oxide film(SMITH, 1993). Due to their excellent corrosion resistance, stainless steels have been using on a large scale in the industry.

The chromium oxide layer is spontaneously formed in contact with the air, but can be degraded depending on the steel's condition and the environment in which it is applied. These steels are sensitive to chloride ions' presence in the medium, and the Cl-ions can break down the passive oxide layer, exposing the metal to the corrosive medium, and thus allowing their degradation by different corrosion processes. (COSTA *et al.*, 2010). Other alloying elements can also help the chromium form a more resistant oxide layer, improving the steels' corrosion resistance, like nickel, molybdenum, aluminum, and others (LIPPOLD; KOTECKI, 2005).

The stainless steel classification is based on their primary metallurgical phase and they can have three base phases: martensite, austenite, and ferrite. Additionally, it is possible combine two different phases to produce a duplex microstructure consisting of a well-balanced corrosion and mechanical properties. Besides, it is possible introduce hardener particles within the matrix phase, improving mechanical strength. Therefore, the main classification of the stainless steels consiste of 5 categories: martensitic, ferritic, austenitic, duplex (approximately 50% ferrite and 50% austenite), and the precipitation hardenable (PH), which is done by an aging heat treatment that causes strengthening precipitation (LIPPOLD; KOTECKI, 2005). This thesis will address austenitic and ferritic stainless steel categories; therefore, these types of steels will be reviewed in more detail in the following sections.

4.1.1 Ferritic Stainless Steels

Ferritic stainless steels have their structure formed basically by BCC α-iron solid-solution (ferrite), as predominant phase. This microstructural feature occurs due to the addition of

ferritizing alloying elements, such as chromium, aluminum, titanium, molybdenum and niobium, which inhibit the formation of austenite on heating (O'BRIEN; SOCIETY., 1991). According to Lippold e Kotecki (2005), these steels are preferable for use when the the application requires resistance to corrosion, rather than mechanical properties, such as strength and toughness.

Initially, the ferritic stainless steels were developed and applied for situations where the manufacturing did not involve welding. This limitation is because it must be affected by harmful metallurgical modifications that cause problems, especially on the steel toughness (FOLKHARD, 1988). In fact, the fusion welding increases the grain size, especially in the heat affected zone (HAZ), and promotes in some instances the precipitation of unwanted secondary phases (SMITH, 1993).

An example of this undesirable effect has been reported by Alizadeh-Sh *et al.* (2014), where the authors analyzed the phases formed in welding of AISI 430 ferritic stainless steel. The author showed that there was an intense grain growth in the high-temperature heat affected zone. Martensite may also be formed in ferritic stainless steel depending on the chemical composition, resulting from the welding thermal cycle, which provides intense heating, allowing a partial austenitizing process, followed by a fast cooling which suppresses the diffusion and makes possible a non-diffusional martensitic phase transformation (SILVA C. C., 2006).

Silva *et al.* (2008b) analyzed the microstructural change of AISI 444 ferritic stainless steel and reported an intense grain growth in the thermally affected zone compared to the base metal grain size. The authors also observed the sigma (σ) phase precipitation in the grain boundary and chi (χ) within the grain. These phases must be controlled in the manufacturing process because, in excess, they can cause a localized reduction of alloying elements essential for corrosion resistance.

Caetano *et al.* (2019) identified precipitates rich in chromium in AISI 410S ferritic stainless steel after FSW weld. The authors found precipitates with values of around 16 wt% and 21 wt% of chromium. The base metal has approximately 12,5 wt% of chromium, and consequently, the precipitate stole the alloying element and depleted the adjacent region, as shown in Figure 4.1.

Figure 4.1 – Analysis performed by EDS (energy dispersive X-ray spectroscopy) showing precipitates with a high amount of chromium: a) SEM-SE mode image of the precipitate, b) EDS mapping for the carbon; c) EDS mapping for the iron; and d) EDS mapping for the chromium.
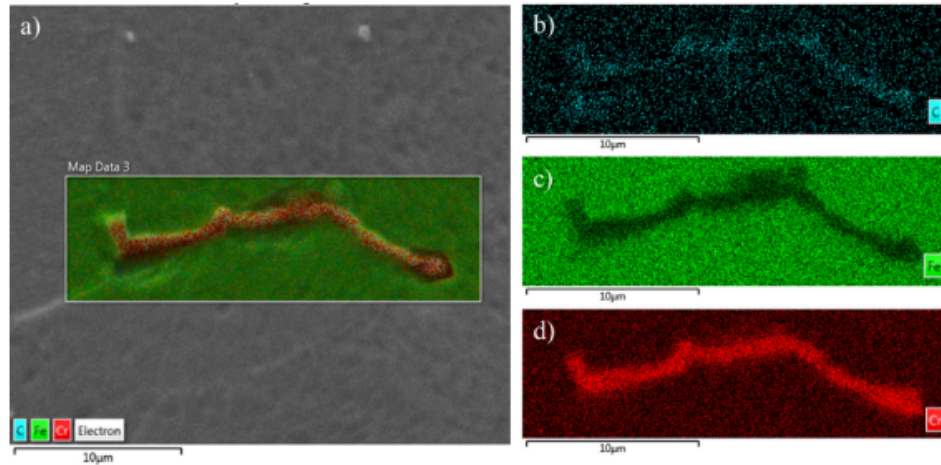
Source: Caetano *et al.* (2019)

4.1.2   *Austenitic Stainless Steels*

Austenitic stainless steels have an iron FCC structure, called austenite, as the predominant microscopic phase. The stabilization of the iron FCC structure at room temperature is attributed to the nickel and other austenitizing elements addition, such as nitrogen, copper, and manganese, restricting their transformation in other metastable phases, over a wide range of temperature, depending on their composition. The nickel is also responsible for providing good mechanical properties, especially concerning ductility and toughness (AMUDA *et al.*, 2016).

The austenitic steels useful properties have spread their use in the most diverse areas, such as structural support and containment, the architecture uses, kitchen equipment, and medical products (LIPPOLD; KOTECKI, 2005).

These steels are divided into 200 series and 300 series, designated by the American Iron and Steel Institute (AISI). The 200 series have lower nickel content than the 300 series and higher carbon and nitrogen level (LIPPOLD; KOTECKI, 2005).

The 300 series are the most common stainless steels, and these series represent variants of the 18Cr and 8-10Ni present in their compositions. When the alloy has besides the number an "L" in its specification, for example: 304L, represents a low carbon alloy version. The variants and the improvement in authentic stainless steels properties make this class one of the most used (LIPPOLD; KOTECKI, 2005).

Despite the excellent properties of austenitic stainless steel, welding, when not

properly adjusted, can cause defects in unwanted metallurgical transformations due to the high thermal input. The high temperatures during welding favor the migration of chromium and other alloying elements that can accumulate in the form of chromium carbides and sigma phase (FOLKHARD, 1988). The sigma phase is rich in alloy elements that are important for corrosion resistance of steel such as chromium and molybdenium (VITEK; DAVID, 1986). Park *et al.* (2004) showed that the formation of a sigma phase (rich in chromium) can cause a decrease in the amount of chromium to levels below 12% in the adjacent regions and, consequently, favor the corrosion of the material.

4.2 Friction Stir Weld (FSW)

The FSW was a great innovation in the fabrication process in the last years. The Welding Institute developed this welding process at 1991 (THOMAS *et al.*, 1991), aiming to join low melting point alloys with difficulties to be performed by conventional fusion welding processes. Since, their applications were expanded for other kinds of materials, including high melting point alloys, such as carbon steels, stainless steels, Ni-based alloys, Cu-based alloys and Ti-based alloys. This welding process has as main characteristics to be performed in a solid-state condition, where a rotational tool translates between the interfaces of two plates of materials, as shown in Figure 4.2.

Figure 4.2 – Schematic view of friction stir welding (FSW)
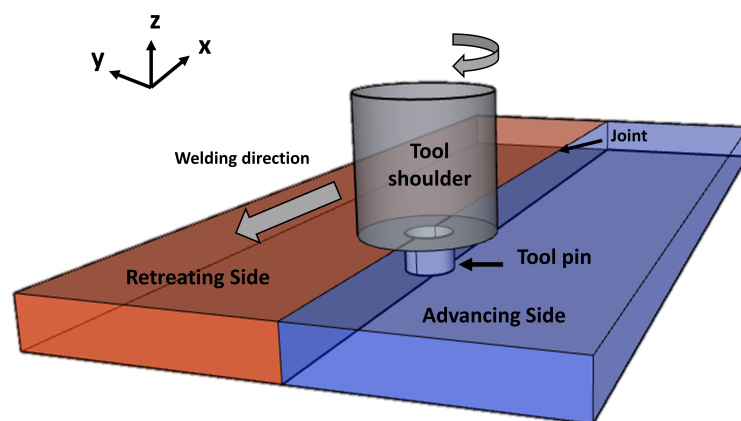
Source: The author

Initially, a rotational tool, with probe (pin) and shoulder, is plunged against the surface materials to be joined, which is rigidly fixed on a backing plate. The backing plate should be designed to withstand high forces and high temperatures during the welding process. When the tool comes in contact with the plates' surface, the friction starts to be done (PRADEEP,

2012). The localized heating softens the material around the pin, and several plastic deformations occurs during the welding by the action of the tool on the plates.

According to the side in the joint regarding the tool rotation and welding direction; the sides of the part are named advancing and retreating sides. The behavior in each side can differ significantly in terms of friction developed, temperatures reached and materials flow during the welding. According to Mishra (2018), the welding direction's side in which the rotating tool moves in the same direction as the welding direction is known as the advancing side and, the other side, where tool rotation is opposite with welding direction is known as retreating side.

Initially, this process caused a revolution in joining aluminum components of aerospace, rail, automotive and shipbuilding industry (MISHRA; SHOESMITH, 2014), because FSW has many advantages compared to the melting process. As FSW occurs at temperatures below the melting temperature, problems due to fusion do not exist, as solidification cracks and porosity. Besides that, the lower heat input minimizes distortions. Also, the process does not generate splashes, ultraviolet radiation, smoke, residues, and has energy efficiency, requiring only 2.5% of the energy required in laser welding (CAETANO, 2012; MISHRA; SHOESMITH, 2014; WILLIAMS, 2001).

Despite this process advantages, there are some limitations, such as the need for sturdy fastening structures and powerful and high melting point tools. Because of this reason, the initial application occurs in aluminum because of its lower melting point, but with the development of other tools material, this process has been applied to the materials with a higher melting point, as will be commented in the next section 4.2.1 (CAETANO *et al.*, 2019; ANDRADE *et al.*, 2015).

4.2.1   *FSW tool*

The purpose of the tool is to generate heat and material flow (UDAY *et al.*, 2010), where the shoulder is responsible for developing significant part of the heat and for plastify the material for weld, and the shoulder and pin make the material flow in the welding (NANDAN *et al.*, 2008b). In this way, the tools must have a higher melting point than the materials that will be welded, and this is one of the reasons for developing different material tools, as M2 tool steel (NANDAN *et al.*, 2008b), tungsten (NANDAN *et al.*, 2006a), Polycrystalline Cubic Boron Nitride (PCBN) (CHO *et al.*, 2013; ANDRADE *et al.*, 2015; CAETANO *et al.*, 2019; CAETANO *et al.*, 2018).

FSW process of materials with a high melting point still requires high abrasion resist, high hot strength, toughness at high temperatures, and loads besides the tool geometry must not change during the process (PACKER, 2013). PCBN is a super abrasive material with high hardness and melting point therefore, there is a high acceptable for FSW tool of welding high melting point materials.

Besides developing tool materials, their geometry is also being developed because the geometry is essential for welding quality. It can reduce force, facilitates penetration, increases the interface between the tool and the plastified material, and, consequently, improve the material flow (GIBSON *et al.*, 2014).

Padmanaban e Balasubramanian (2009) showed in their study the geometry influence on the materials flow and heat generation. The authors verified five different geometries, as shown in Figure 4.3.

Figure 4.3 – Schematic of FSW tools geometry
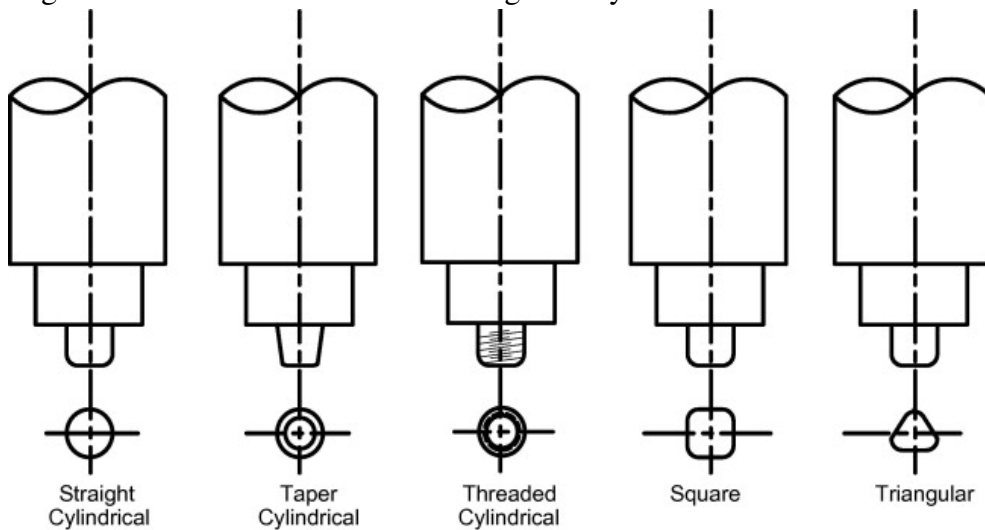
Source: Padmanaban e Balasubramanian (2009)

Figure 4.4 shows that some wormholes can be avoided just by replacing the tool; consequently, the material flow changes and the mixture can be done without defects. It can be noted that weld defects influences the mechanical properties, and all the weldswith defects have failed along with these defects.

Figure 4.4 – Defects on weld joined by different geometric tools

Tool pin profile	Weld cross-section Shows defect location		Probable reasons for defect	Location of failure during tensile test
	AS	RS		
SC			absence of vertical motion of the material	along the defect
TC			absence of vertical motion of the material	along the defect
TH			defect free	AS-TMAZ
SQ			large amount of metal sweeps from the stir zone	along the defect
TRI			insufficient heat generation	along the defect

Source: Padmanaban e Balasubramanian (2009)

Therefore, besides the tool geometry influence heat generation and material flow, it can cause defects on FSW weld if the tool is not appropriately chosen. However, this is not the only cause for poor quality welds.

4.2.2 Defects in FSW
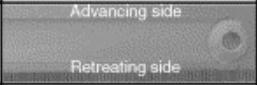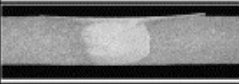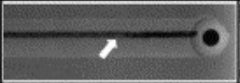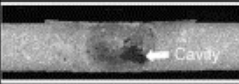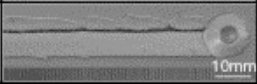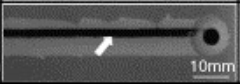
As with any welding process, the FSW may also be defective. The most common defects are tunnel, flash, wormhole, and cracks. The selection of inappropriate parameters also can be responsible for forming these defects.

4.2.2.1 Wormhole / Cavities defect

High welding speed is desired from the point of view of productivity because it results in less manufacturing time and more economical welds. However, when the welding parameter are not well adjusted, the wormholes may appear. Different factors can influence the hollow in FSW, and the wormhole is one type of hollow, whose formation mechanisms is attributed to the incorrect flow of material. However, this defect can be resolved by adjusting the

welding parameters. Welding speed has a strong effect on forming different kinds of cavities, including wormholes, due to abnormal stirring. According to Kim *et al.* (2006), abnormal stirring has been observed when a significant temperature difference is found between the upper surface and the bottom of the weld.

Figure 4.5 – Inspection of FSW joints by visual, X-ray radiography and cross-section.

FSW, ADC12, 4mmt, Stir-in-plate, 1500rpm			
	Bead appearance	X-ray radiography	Cross-section
Sound joint (6.9kN, 250mm/min)	Advancing side / Retreating side		
Inner defect (6.9kN, 500mm/min)			Cavity
Lack of bonding (6.9kN, 750mm/min)	10mm	10mm	2mm

Source: Kim *et al.* (2006)

Other authors(RANJAN *et al.*, 2016; ZHANG; LIU, 2012) classify wormholes as tunnel or groove defects. Tunnel defects are usually formed on the advanced side because of insufficient material flow in this region (SONI *et al.*, 2017; HOU *et al.*, 2014). Mishra e Ma (2005) reviewed the aspects related to tunnel defects and pointed out that this defect has been caused by the insufficient heating produced by the use of low rotational speeds and low axial forces. Another study performed by Kumar *et al.* (2008) has shown that besides low heating, a lower tool shoulder pressure exerted on the material surface can also affect the plasticizing and flow. Caetano *et al.* (2018) have experimentally demonstrated that tunnel defects can be eliminated by choosing the correct parameters directly related to heating and plasticizing, as rotational speed and axial force, which has a strong effect on heat input and material flow, respectively.

Besides, in some instances this problem can also be minimized by decreasing the welding speed, because lower speeds increase the time of friction of the tool at the same region, helping to increase the heat input, and, consequently, the material will become more plastic and prevents tunnel formation(SONI *et al.*, 2017; HOU *et al.*, 2014). Hou *et al.* (2014) showed that increasing the speed can increase the formation of tunnels. Figure 4.6 A and B show an apparent increase in the tunnels' size due to the increase in speed. In this study, the formation took place mainly by a non-threaded tool that caused an inefficient flow in the vertical direction and favored high speed so that the material flow did not have time to fill the remaining space.

Figure 4.6 – Macrographs on cross-sections of experimental FSW T-joints.
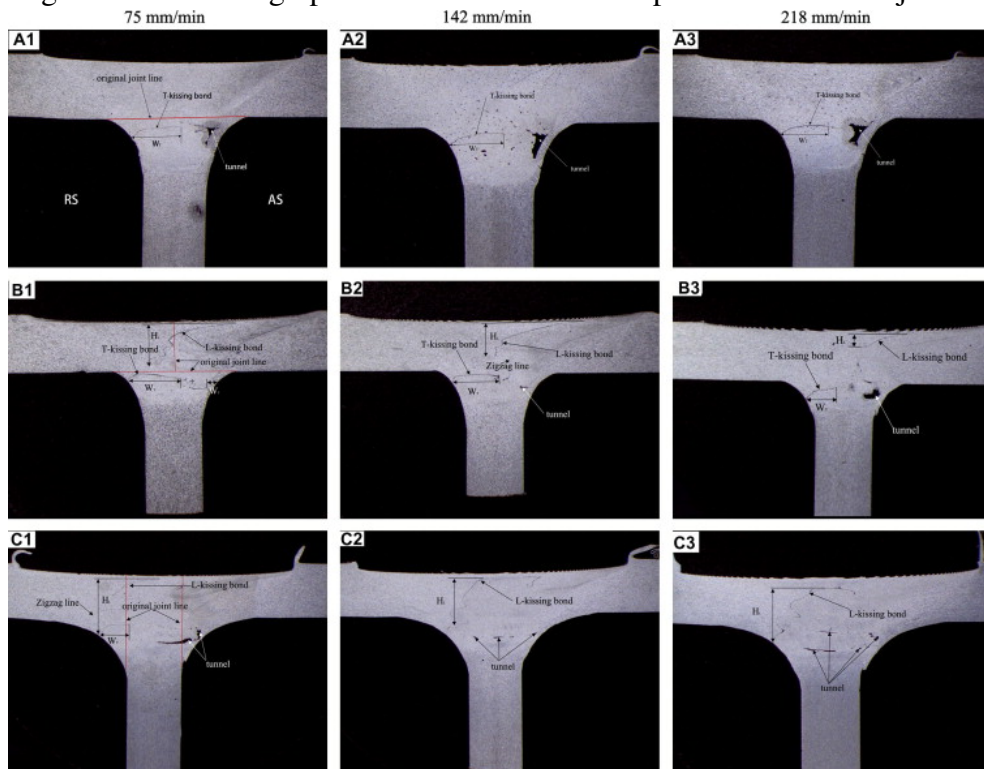
Source: Hou *et al.* (2014)

Another way of avoiding tunnel problems is improving the design and geometry of the welding tool because the tool is responsible for the flow of material in the FSW. Padmanaban e Balasubramanian (2009) already showed how the tool's geometry can influence the flow of the material, as shown in Figure 4.4. The weld produced by the threaded tool (TH) has no defect because the thread generates a vertical flow of material and favors the filling of defects at the pin's base.

4.2.2.2   Flash Defect

The flash defect is formed when occur the softening of material in contact with the shoulder. The excess softening occurs because of the considerable thermal input due to friction, and the excessive pressure expels the material in the form of a flash (KAH *et al.*, 2015; LI *et al.*, 2011).

This defect can be seen in the study of Kim *et al.* (2006) where the authors showed the formation of flashes in the condition of high rotation and low welding speed, exemplified by Figure 8.8. High rotation generate more heat than conditions applying lower rotational speed, and the lower speed means that this thermal input is applied for a longer time at each point of the weld. These combinations of factors increase the welded region's temperature and, consequently,

cause a more intense softening of the material. When the material becomes more soft, it does not resist the tool's axial force and is expelled in the form of flashes.

Figure 4.7 – Example of flash defect.
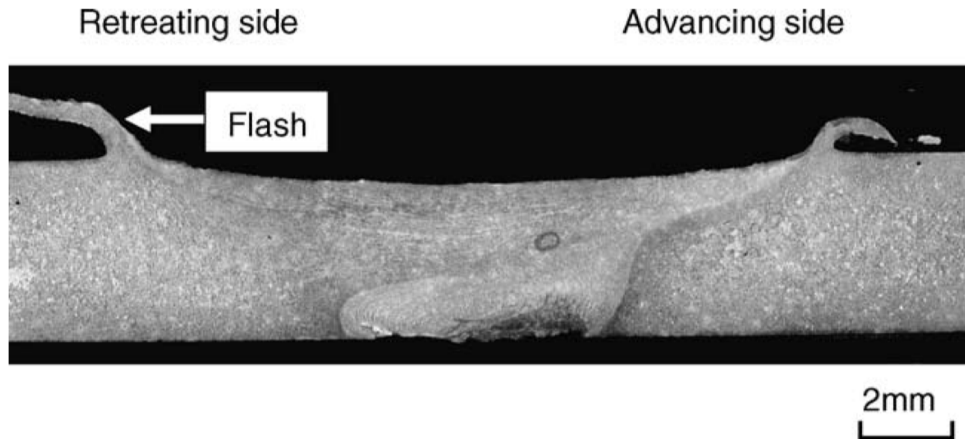
Source: Kim *et al.* (2006)

4.2.2.3 Cracks Defects

Crack root defects are generated by insufficient heat input or when the oxide layer is not entirely broken (SONI *et al.*, 2017). Another situation where this problem occurs is when a too small pin for the thickness workpiece is used. As the pin is small, the workpiece bottom is inaccessible and causes the region to fail, as shown by Li *et al.* (2011) in Figure 4.8.

Figure 4.8 – Microstructure of the crack-like root-defect.
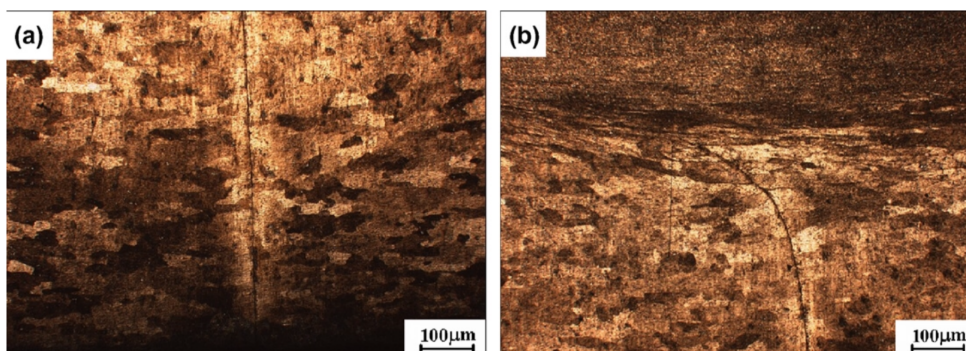
Source: Li *et al.* (2011)

4.2.3 Stainless steel welded by FSW

The welding of stainless steel by FSW started approximately twenty years ago when Thomas *et al.* (1999) demonstrated the feasibility of weld steels, including stainless steel, using

FSW. One of the first studies on the stainless steel FSW welds was published in 2003 by Reynolds *et al.* (2003), which evaluated the properties and residual stress of 304L stainless steel. The results have shown that the welds were overmatched compared with the base metal; however, the residual stresses in FSW welds were quite similar to those produced by fusion welding.

From 2003, the research group at the University of Tohoku published a series of articles on the welding of 304L stainless steel by FSW with a focus on microstructure and corrosion resistance (PARK *et al.*, 2003; PARK *et al.*, 2004; PARK *et al.*, 2006). Kokawa *et al.* (2005) analyzed the microstructure and properties resulting from the FSW of 304 stainless steel. The authors made welds of 2 and 6 mm thick and observed a higher hardness in the weld when compared to the base metal. This higher hardness was associated with a lower grain size produced in the weld zone and high dislocation density. The authors also reported the formation of sigma phase in the weld.

In order to observe the effects of sigma phase precipitation, the same group published further studies investigating the corrosion properties of these welds (PARK *et al.*, 2004; PARK *et al.*, 2006). The authors observed that the heat affected zone had little sensitization, and it was attributed to the short time that the region was exposed to sensitization temperatures. Low temperatures are one of the advantages of the FSW method when compared with fusion weld, because in FSW the good results are obtained in approximately 80% of melt point(SILVA *et al.*, 2020c). However, the grain boundaries were corroded in the advancing side of the stir zone. This effect was due to the formation of the sigma phase, caused by the higher temperature of the weld's advancing side.

Sato *et al.* (2005a) analyzed the recrystallization in 304L steel during FSW welding. In Figure 4.9 an apparent decrease in the grain size of the "CEN" region (lies at the centerline of the stir zone) and "AS2" (located 2.3 mm away from the friction stirring center at the advancing side) is possible when compared with the base metal (BM).

Figure 4.9 – Grain Boundary maps obtained by orientation imaging microscopy analysis of the base material, regions CEN and AS2 on the transverse plane of friction stirring direction
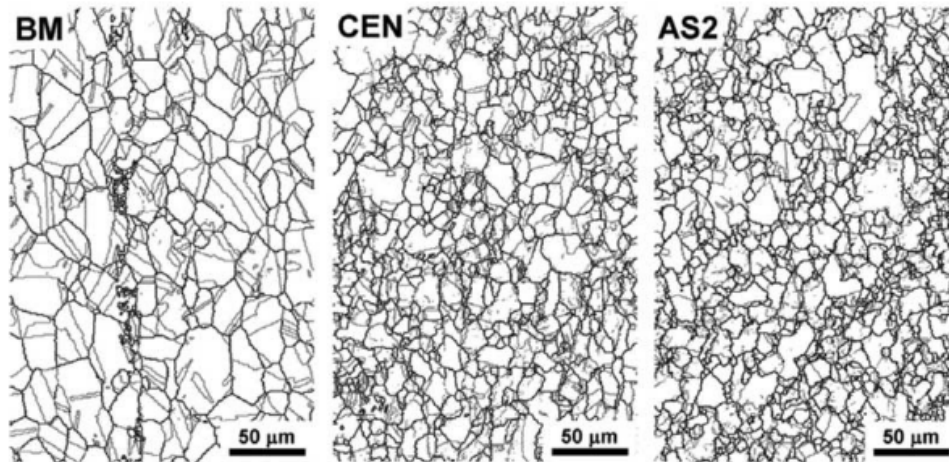
Source: Sato *et al.* (2005a)

Sato *et al.* (2005b) welded duplex stainless steel by FSW and obtained high-quality joints. The technique refined the ferrite and austenite grain, causing the material to increase in strength in the stir zone. Sathiya *et al.* (2007) analyzed the effect of weld parameters on ferritic stainless steel, similar to that applied for austenitic stainless steel. These welds showed better results than welds produced by the fusion process because FSW refined the grain in the welded region.

Several other authors have explored the potential of FSW in stainless steel due to the great potential of the technique and the several gaps in the literature. Bilgin e Meran (2012) analyzed the influence of welding parameters (rotation and transverse speed) in FSW of AISI 430 ferritic stainless steels, and the author and the authors found an increase in the temperature of the tool with an increase in rotation due to the more significant attrition, and a decrease in temperature with an increase in transverse speed.

Caetano *et al.* (2018) also analyzed the influence of weld parameters of FSW, however on of AISI 410S ferritic stainless steel. The author associated more intense pressures to the formation of flashes because greater pressures increase the thermal input, more material is plasticized , and consequently, the material does not resist axial force, and it is expelled in the form of flashes. Based on the results, it was also possible to note that the increase in heat input due to rotation also favors the formation of flashes.

Kim *et al.* (2017) welded 430M2 ferritic stainless steel sheets by FSW, and they obtained a mixing zone had significant grain refining, with grains from 5 to 8 μm, while the grains of the base metal was approximately 20 μm. Another interesting aspect of this study was

the joints that were produced by a tool without a pin, as shown in Figure 4.10.

Figure 4.10 – Schematic illustration for FSW using pinless tool
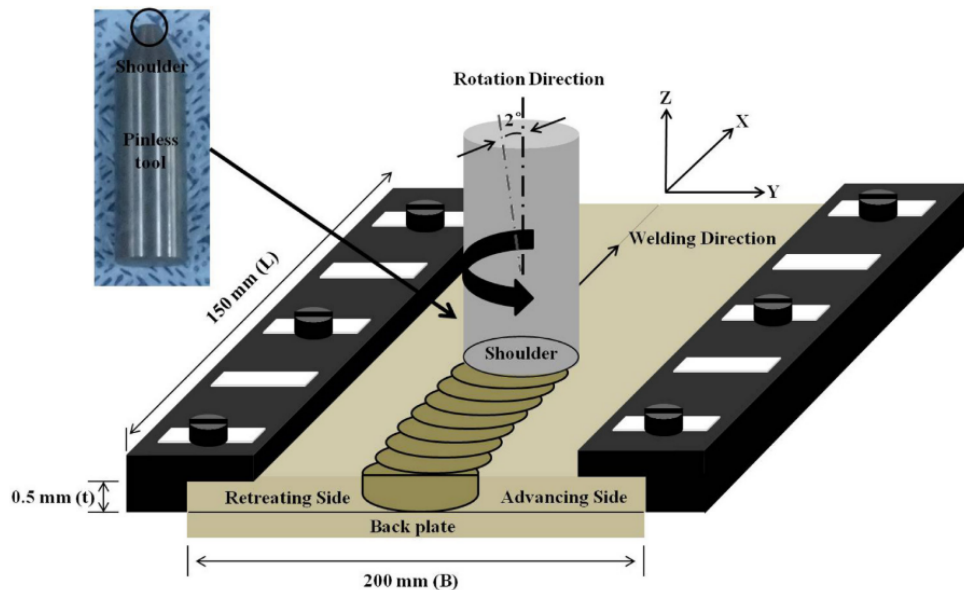
Source: Kim *et al.* (2017)

Despite the complexity of similar FSW welds, joining different materials can be more challenging. Analyzing the FSW parameters and the mixture between materials with such different properties have been the subject of many studies in recent years.

4.2.4   Dissimilar joining by FSW

The FSW, in addition to the several advantages already mentioned in this document, made it possible to combine different materials, which has been widely discussed in this technique over the years. FSW allows the union of different materials with the minimal chemical mixture, making sure that each material's properties are preserved, as there is no formation of an intermediate material due to dilution. In Anaman *et al.* (2019)'s study, it is possible to observe this behavior, in which aluminum alloy was welded with steel and in the analysis whether Dispersive energy spectroscopy(EDS) it is possible to clearly distinguish the two materials, as shown in Figure 4.11.

Figure 4.11 – Cross-section analysis of steel and aluminum dissimilar FSW
weld (a) Backscattered-Electron image in the Scanning Electron
Microscope and (b) EDS chemical map
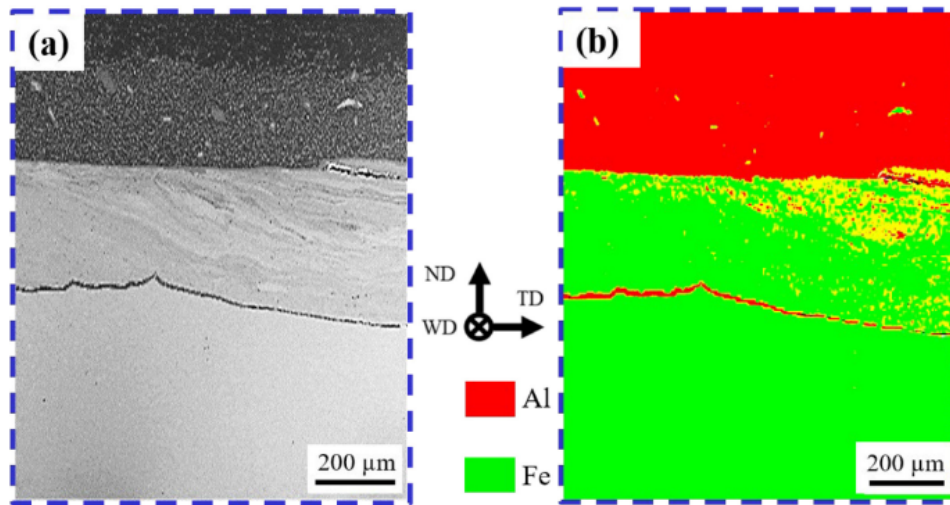
Source: Anaman *et al.* (2019)

Derazkola *et al.* (2020) observed similar behavior in the welding of Al-Mg alloy and low carbon steel, where it is possible to observe a clear division between each material, as shown in Figure 4.12. The authors analyzed the FSW made in air and water, and the environment where the welding takes place influences the peak temperature and cooling speed. They observed that welds with lower peak temperatures and lower cooling speeds had smoother surfaces and little oxidation.

Figure 4.12 – Representative cross-section optical image of the dissimilar
joint
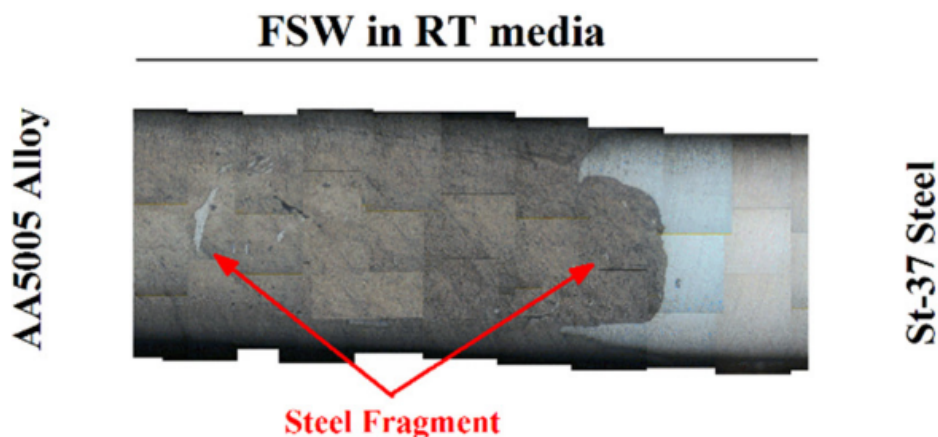
Source: Derazkola *et al.* (2020)

Kwon *et al.* (2008) produced welds from aluminum alloys with magnesium alloys with excellent quality. The author analyzed welds with different rotation speeds, and good quality

welds produced for several of them, showing no single ideal combination of parameters.

FSW proved to be such a versatile technique that even non-metallic materials were joined to metallic materials. Derazkola e Simchi (2019) welded aluminum alloy T joints with methyl methacrylate by FSW. Despite the differences between the two materials, it was possible to perform the union in satisfactorily way with the correct choice of parameters. The various studies presented show the incredible versatility of the FSW method and the infinity of analyzes to be explored concerning materials and their phenomena and the parameters inherent to the process.

4.3 FSW Simulation

Numerical simulation represents a significant role in understanding the phenomena of this welding method. The first simulations addressed only the phenomena of heat conduction, and they disregard the phenomena of plastic flow near the tool. Frigaard *et al.* (2001) simulated the FSW process using friction as the only heat generation source. This heat generation was calculated by Equation 4.1.

$$q_0 = \frac{4}{3}\pi^2 \mu_f PNR^3 \tag{4.1}$$

Where this equation depends on pressure (P), surface radius (R), friction coefficient (μ_f), and the number of rotations by second (N). It used a simplified tool model defined by many squares defined it on x-y plane displaced on z-direction (Figure 4.13). Despite the numerous simplifications of this model, it presented good results with differences of approximately 30 degrees in the peak temperature, a value within the thermocouple's error range.

Figure 4.13 – Schematic representation of the heat source. Only half of the source is considered due to symmetry
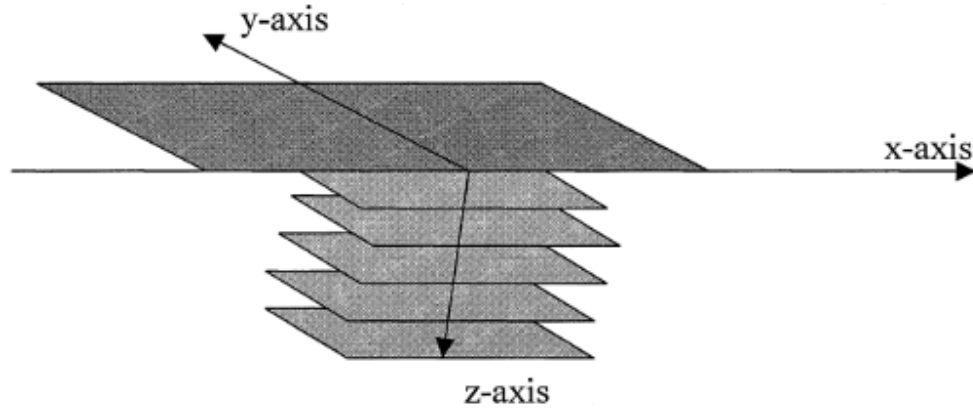
Source: Frigaard *et al.* (2001)

Other study studies began to consider the flow around the tool and heat by plastic deformation with the evolution of numerical simulation. Seidel e Reynolds (2003) simulated FSW based on fluid dynamical, where the authors used Perzyna's viscoplasticity model, in which viscosity ($\mu(T,\dot{\varepsilon})$) was defined by equation 4.2.

$$\mu(T,\dot{\varepsilon}) = \frac{\sigma(T,\dot{\varepsilon})}{3\dot{\varepsilon}} \tag{4.2}$$

Where $\dot{\varepsilon}$ is the strain rate, and σ is effective flow stress proposed by Sellars e Tegart (1972). Furthermore, modified by Sheppard e Wright (1979), the equation 4.3 was developed.

$$\sigma(T,\dot{\varepsilon}) = \frac{1}{\alpha} ln \left(\left[\frac{Z(T,\dot{\varepsilon})}{A} \right]^{1/n} + \left\{ \left[\frac{Z(T,\dot{\varepsilon})}{A} \right]^{2/n} + 1 \right\}^{1/2} \right) \tag{4.3}$$

Using Zenner-Hollomon parameter Z, A, and α are material constants, which is calculated by:

$$Z = \dot{\varepsilon} exp \left(\frac{Q}{RT} \right) \tag{4.4}$$

Where R is a universal gas constant, T is temperature, and Q is the temperature-independent activation energy.

The authors used this viscosity model to simulate a two-dimensional friction stir weld. It used a simulation approach to that presented in this thesis where the pin was kept stationary, and a flow of fluid was placed, as shown in Figure 4.14. This approach makes it possible to use a fixed mesh in the study.

Figure 4.14 – Schematic diagram of flow domain: fluid flows from right to left past clockwise rotation circular cylinder
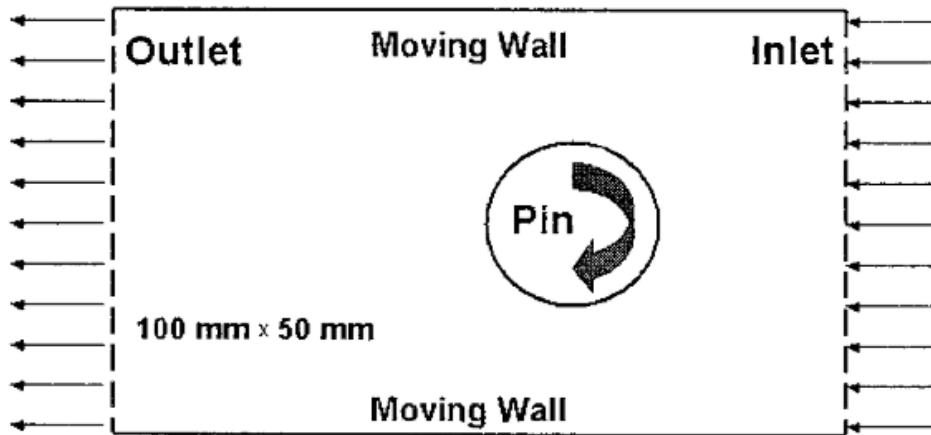
Source: Seidel e Reynolds (2003)

Despite the model's innovation, the authors concluded that simplifying the model to two dimensions decreased the thermal input, because the shoulder was not considered and a three-dimensional simulation with a threaded pin was suggested.

In the same period, Ulysse (2002) simulated FSW in aluminum alloy using the same model, however, applying a tridimentional simulation. The author predicted temperatures satisfactorily, but reported that the model tends to overestimate the values probably because it does not predict the material properties under FSW's strain conditions. The simulation presented also made it possible to calculate the stresses in the tool and predict failures during the process.

With the development of numerical simulation in three-dimensional for aluminum alloys, the simulation of other materials proved to be necessary. Nandan *et al.* (2006b) simulated FSW of 304 stainless steel. The authors used the same models presented by Ulysse (2002), but the tool was omitted from the simulation. In code was considered only the effects of tool. Nandan *et al.* (2006b) and Ulysse (2002) showed an advancing and retreating side's asymmetry, which the advancing side results in superior temperatures.

Nandan *et al.* (2006a) observed that the viscosity range is similar to the viscosity values found in aluminum simulation, between $1 \cdot 10^6$ and $4 \cdot 10^6$ Pa.s. With stream trace was possible to see a reversion point in base of pin and it can cause a wormhole because this region has the smallest recirculation of material.

One year after, Nandan *et al.* (2007) simulated FSW with the same method for mild steel. The authors developed a velocity in *z*-direction ($w = k\frac{\omega}{2\pi}R_p$), which is caused by threads of pins (k), and it depends of pin radium R_p and angular velocity (ω). The coefficient of friction

adopted in their study was not constant, being defined by the Equation 4.5.

$$\mu_f = \mu_0 exp(-\lambda\delta\omega r) \tag{4.5}$$

Where μ_0 and λ are constants, r is the radial distance, and δ denotes the fraction-slip, which can be calculated by equation 4.6.

$$\delta = 1 - exp\left(-\frac{1}{\delta_0}\frac{\omega}{\omega_0}\frac{r}{R_s}\right) \tag{4.6}$$

The authors obtained good results, similar to the previous simulations, such as high convection close to the tool, good results in the prediction of temperatures, the asymmetry between the advancing and retreating sides. The maximum viscosity where there is no more significant movement of the material was $9.9 \cdot 10^6$ Pa.s, slightly higher than that of Nandan *et al.* (2006a) study.

Cho *et al.* (2013) simulated 409 ferritic stainless steel with the same method presented by Nandan *et al.* (2007). It also showed good results in predicting the temperature, and the authors showed that the asymmetry between the sides of the weld increases with increasing welding speed. An excellent analysis carried out in this study was predicting the crystallographic texture of the material. The simulated texture was made from the velocity gradients, and these matched smoothly with the experimental results.

With the consolidation of the simulation models, several authors added new methodologies and analyzes the existing model to extract new results. Zhu *et al.* (2016) simulated the joining of AA2024-T4 alloy plates by FSW, however, the particle tracing methodology was used to map the particles' path inside the welded plate. This mapping of the particles made it possible to observe the places where the material flow would be inefficient and consequently to predict the possible formation of voids as shown in Figure 4.15 of simulation with Non-uniform friction force boundary (Figure 4.15-a). In the simulation with partial sticking velocity boundary, the results did not corroborate with experimental (Figure 4.15-b).

Figure 4.15 – Comparison of the joint area morphology, (a) tracing particle distribution in the observation plane after moving through the tool area (Sim-1.1–1.5), (b) Sim-2.1–2.5, and (c) wormhole defect distribution in the nugget area after the experiment
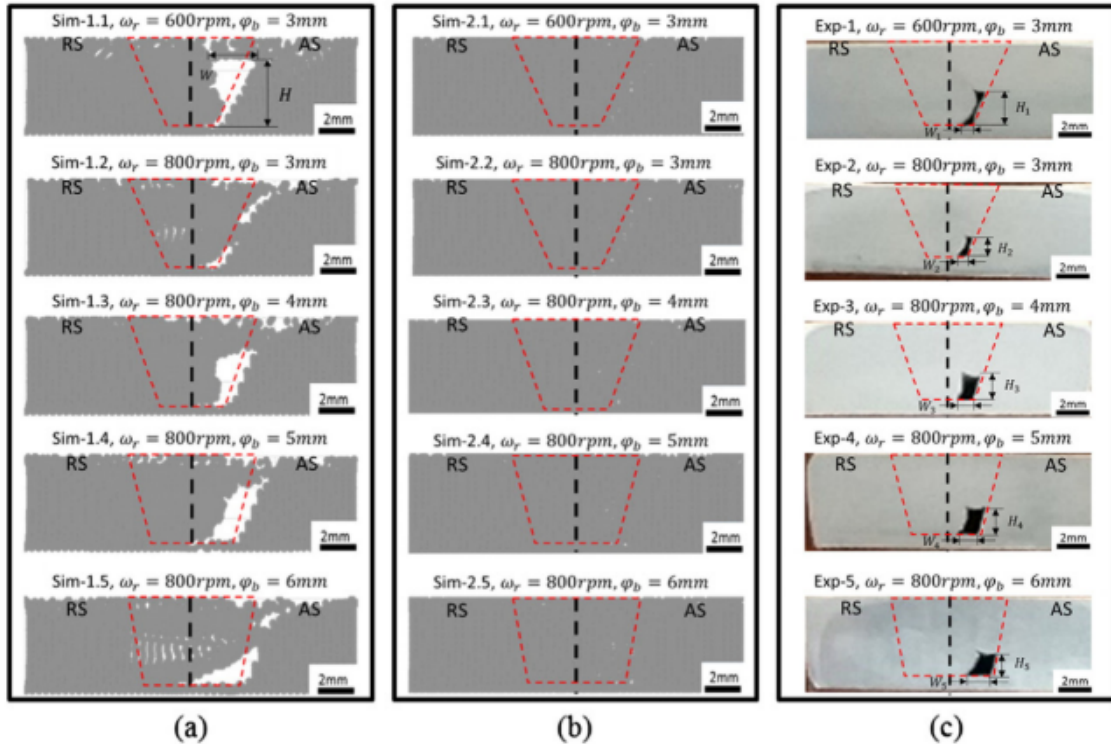
FSW brought significant advances to dissimilar welding, and, consequently, the simulation was required to predict and improve this application. Hernández *et al.* (2017) modeled the FSW between dissimilar steels. The model used does not differ much from the models discussed so far, but conceal welding requires some method for mixing the two materials, and the volume-of-fluid (VOF) was used.

Hirt e Nichols (1981) developed the VOF model for two-phase flows because it is necessary to add in equations the volume fraction accounting for interfacial flow. This method's addition allows the interaction between the two materials and the visualization of the mixture between them as shown in Figure 4.16.

Figure 4.16 – Volume fraction distribution for the *yz*-plane at welding veloci-
ties (U): a) $U = 0.31\ mm \cdot s^{-1}$ and b) $U = 0.42\ mm \cdot s^{-1}$
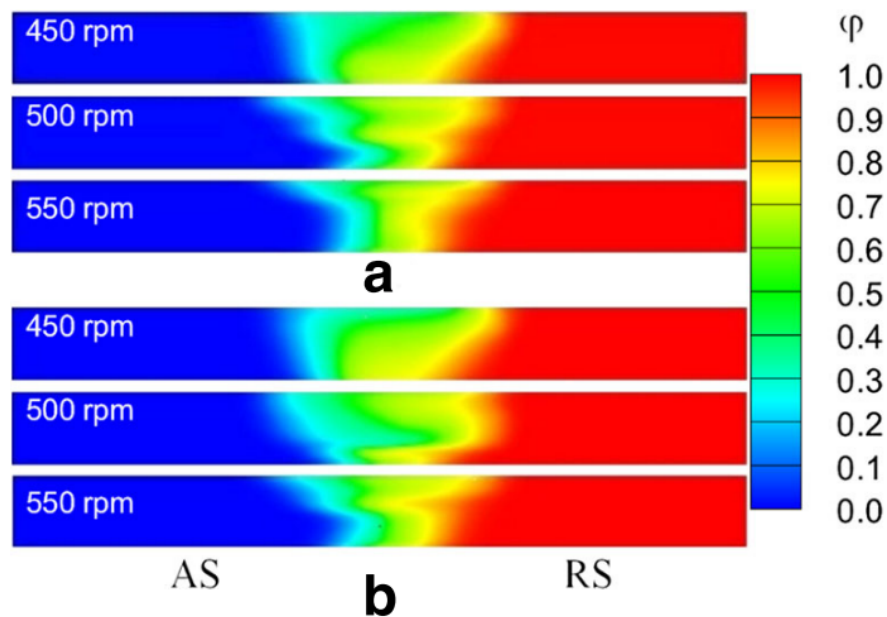
Source: Hernández *et al.* (2017)

VOF was also used by Yang *et al.* (2018) to simulate welding between the aluminum and magnesium alloys. The authors managed to add in the code the reduction of tension caused by the material's recrystallization around the pin, the local chemical composition resulted in the liquefaction due to an eutectic reaction between the solid-solution aluminum and magnesium alloys, resulting in the lower melting point intermetallic compounds. These considerations show the importance of analyzing and modifying the models for each type of material.

In this thesis, the simulation was performed assuming the welded material as a non-Newtonian fluid, where its viscosity varies with the deformation rate and temperature, as commented in this review. However, this study's exact method is better detailed in chapters 5, 6, 7 and 8.

This session was designed to comment on the evolution of FSW simulation by fluid dynamic; however, there are simulation methods not covered in this study that are interesting for future works. Meyghani *et al.* (2020) simulated FSW on a complex curved plane, as shown in Figure 4.17. It was based on finite elements on ABAQUS software. The dynamic mesh was also used during the tool's movement along with the plate. It manages to simulate the tool's movement in curved plates, which was not presented precisely in the literature.

Another difference between Meyghani *et al.* (2020) method and the numerical simulation used in this thesis is the viscosity model. The authors use the Johnson-Cook model to

calculate viscosity, and this thesis used the models presented by Nandan *et al.* (2006a) and Cho *et al.* (2013). These model variations showed that different models could be applied. However, despite the difference between the models, they depend on the temperature and the material's deformation rate.

Figure 4.17 – The mesh and the boundary condition for a complex curved plane
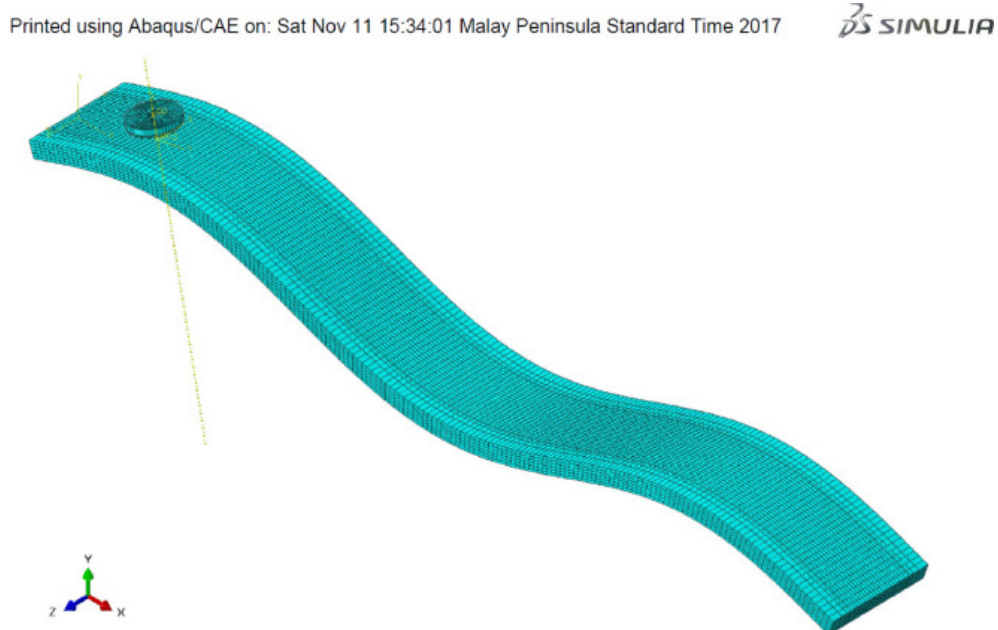
Source: Meyghani *et al.* (2020)

Finite elements also is used by other authors. In a study developed by Zhang *et al.* (2005) this method also was used. However, the authors kept the tool stopped and moved the metal plate. Due to the type of simulation used, the dynamic mesh was necessary. In this thesis's method, finite volumes, the tool was not translated, and the plate was, in the same way as Zhang *et al.* (2005). However, there is no need to use dynamic mesh because in the finite volume method, the tool does not move with the volume of the control.

In addition to the methods already mentioned, there is a third form of simulation used to model the FSW, the simulation by particles. Yoshikawa *et al.* (2012) said that most articles use the finite element and finite difference method but have great difficulty modeling advective terms. As a solution to this problem, the authors proposed the simulation of FSW using the particle method. This method has the potential to predict surface defects, like a flash. Another fact in this simulation is the ease of analyzing the results, because they are visually simple, as shown in Figure 4.18.

Figure 4.18 shows dissimilar materials, on red and blue, in different moments of

FSW welding. It can be noted that on FSW progress, the materials mechanical mixture will be done.

Figure 4.18 – Front view of particles moving near probe: a) $t = 0$s; b) $t = 0.025$ s; c) $t = 0.075$ s; d) $t = 0.175$ s and e) $t = 0.425$ s
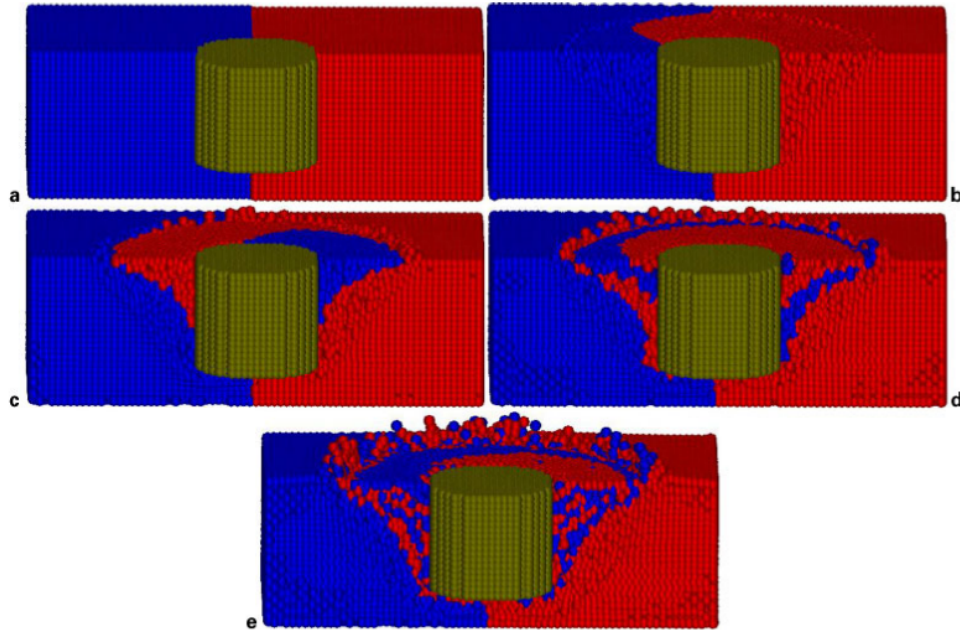
Source: Yoshikawa *et al.* (2012)

5 ANALYSIS OF VISCOSITY FUNCTION MODELS USED IN FRICTION STIR WELDING

5.1 Review

This article analyzed two models of viscosity used in the next chapters, with the objective of solving doubts that arose during the studies made for the construction of this thesis. One of the main analyzes described was the methodology used to choose the maximum viscosity values set in the numerical simulation. The choice of this parameter was not addressed in the literature and was shown to be essential for obtaining good results.

5.2 Introduction

Friction stir welding (FSW) is a solid-state welding system, which was developed by The Welding Institute (TWI, UK) in 1991(THOMAS *et al.*, 1991). This process consists of a tool formed by a shoulder and a pin that rotates between the plates that will be welded by plastic deformation, as shown in Figure 8.1. The heat is generated by friction between the rotating tool and the contact surface, as well as by plastic deformation of the material in the vicinity of the joint line. These materials are joined due to the flow of softened material during the passage of the rotating tool between the plates (CHO *et al.*, 2013).

Figure 5.1 – Schematic diagram used in FSW simulations. a) – the top viewer of tool and b) - velocity boundary conditions.
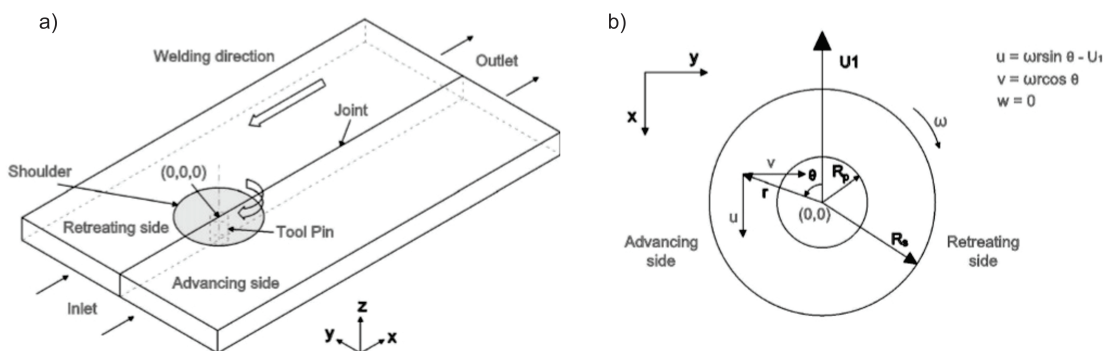
Source: The author

The FSW process has several advantages over traditional fusion welding processes. For instance, low temperature decreases the residual stress and distortion of the welded material. Another advantage is the possibility of grain refining, because of the reduction of temperature and rotation of the tool minimize the grain size or can cause the refining of the grains by dynamic

recrystallization(ANDRADE *et al.*, 2015).

The FSW method involves several coupled physical phenomena such as welding and rotational speed that influences the welding process. Due to the importance and complexity of this process, various numerical simulations have been developed and analyzed in order to understand the influence of each parameters on the results (AL-ARAJI *et al.*, 2011; PATEL *et al.*, 2016; GADAKH; KUMAR, 2018; HE *et al.*, 2014).

The early numerical analyses of the FSW processes were based on heat conduction, but these did not take into account the plastic flow near the tool. Frigaard *et al.* (2001) modeled the heat flow in an aluminum alloy. The authors considered that the heat generated was caused by the friction between the tool and workpiece. In their study, the friction coefficient was adjusted at each time step, because the model did not consider the formation of a liquid film between the tool and workpiece for the conditions analyzed.

As these numerical models evolved, the simulations began to consider the flow of material around the tool. Seidel e Reynolds (2003) developed a 2D model based on fluid mechanics, where the viscosity of the material was a function of temperature and strain rate. This viscosity model was proposed by Sellars e Tegart (1972) and later on was modified by Sheppard e Wright (1979).

Using the viscosity model developed by Sheppard e Wright (1979), Ulysse (2002) developed a 3D model for friction stir welding. Using the same model of Ulysse (2002), Nandan *et al.* (2006a) also performed a 3D investigation, but now for the AISI 304 stainless steel. In this work the commercial software FLUENT was used. Nandan *et al.* (2007) and Nandan *et al.* (2008b) also simulated other materials using the same commercial simulator.

Despite the large number of papers involving the simulation of the FSW process, a detailed analysis of the behavior of the viscosity functions was not found in these previously mentioned papers. A detailed analysis is important because when low temperatures and low strain rates are applied to the current models used to simulate the FSW, the viscosity approaches the infinity. However, it is well known that the viscosity value is finite. Therefore, due to such behavior, the viscosity function must be truncated. This study analyzed two viscosity models used in FSW simulations with different truncation parameters and the results were shown to be sensitive to the maximum viscosity value used.

5.3   Mathematical Modelling

The FSW process consists of three steps. The first step is the penetration of the tool into the workpiece, the second step is when the tool moves through the workpiece, and third step is the withdrawal of the tool from the workpiece. In this study, two distinct materials, Ti-6Al-4V alloy and AISI 304 alloy, were used and only the second step of the welding process was analyzed.

The analysis of the second part of the welding was chosen because this region represents the main part of the weld. This study analyzed the weld under a steady-state condition, where the tool position is fixed and the plate is assumed to move as a continuous fluid flow. It is also assumed that the shoulder was in the top surface of the workpiece, as shown in Figure 5.1. In addition, the pin completely penetrated the workpiece. Throughout the welding the pressure, rotation, and welding speed were considered constant, and the shear stress $\tau = \sigma_{yield}/\sqrt{3}$, where σ_{yield} is evaluated using the distortion energy theory for the plane stress.

The materials were assumed to be non-Newtonian, incompressible, and viscoplastic fluids. A partial sticking condition was assumed between the tool and the workpiece and the tilt angle of the tool was taken to be zero (NANDAN *et al.*, 2006a). The reference coordinates were fixed in the center of the tool and on the top surface of the workpiece. After a grid refinement study, a non-uniform grid composed of only hexahedrons (1,645,020 nodes and 1,763,904 elements for the AISI stainless steel 304 and the Ti-6Al-4V alloy) was modeled using the ICEM-Mesh Software and these grids were used for all simulations.

5.3.1   Governing Equations

The continuity equation for an incompressible, single-phase material is given by

$$\frac{\partial u_i}{\partial x_i} = 0 \; ; i = 1,...,3 \tag{5.1}$$

where u is the velocity of the plastic flow at x-(1), y-(2), and z-(3) coordinates. Equation 8.2 states that the volume variation is null. The momentum conservation equation regarding a co-ordinate system attached to the tool using, the indicial notation again, is given by Cho *et al.*

(2013).

$$\frac{\partial \rho u_j}{\partial t} + \frac{\partial \rho u_i u_j}{\partial x_i} = -\frac{\partial P}{\partial x_j} + \frac{\partial}{\partial x_i}\left(\mu \frac{\partial u_j}{\partial x_i}\right) - \rho U \frac{\partial u_j}{\partial x_1} \tag{5.2}$$

where U is the weld velocity, ρ is the density, P is the pressure, and μ is the non-Newtonian viscosity of the material. Two different models, which will be shown in the next sub-section, were used for the AISI stainless 304 steel and Ti-6Al-4V alloy. The viscosity model was evaluated through two different models for AISI stainless 304 steel and Ti-6Al-4V alloy. The energy conservation equation is given by

$$\frac{\partial (\rho C_P T)}{\partial t} + \frac{\partial (\rho C_P u_i T)}{\partial x_i} = -\rho C_P U_1 \frac{\partial T}{\partial x_1} + \frac{\partial}{\partial x_i}\left(k \frac{\partial T}{\partial x_i}\right) + S_i + S_b \tag{5.3}$$

The simulation was performed under a steady-state regime. However, the transient terms were kept in Equations 8.3-8.4 in order to reach the steady-state through a distorted transient. In Equation 8.4, C_P is the specific heat and k is the thermal conductivity. S_i and S_b are heat sources that are added to the Fluent simulator in the area of the domain between the tool and workpiece. S_i is a source term that denotes the rate of energy per unit of volume dissipated by friction between tool and workpiece, and S_b denotes the rate of energy per unit of volume generated by plastic deformation in the workpiece away from the interface.

5.3.2 Viscosity

In this work, two viscosity plasticity models, based on the works of Nandan *et al.* (2006a) and Nandan *et al.* (2008b), were investigated for AISI 304 stainless steel and Ti-6Al-4V alloy, respectively. In both models, the viscosity (μ) is given by

$$\mu = \frac{\sigma_e}{3\dot{\varepsilon}} \tag{5.4}$$

However, different equations to evaluate the flow stress (σ_e) were used for each material.

5.3.2.1 Flow stress for the Ti-6Al-4V alloy

The viscosity model used in the simulation of Ti-6Al-4V alloy was based on the formulation of the flow stress (σ_e) proposed by Sheppard e Wright (1979), where the flow stress

is a function of the effective strain rate ($\dot{\varepsilon}$) and temperature (T), which is given by

$$\sigma_e = \frac{1}{\alpha}\sinh^{-1}\left[\left(\frac{Z}{A}\right)^{\frac{1}{n}}\right]$$

(5.5)

where α, A, and n are the material constants and Z is the Zener–Hollomon parameter that is a function of temperature and the effective strain rate, and it is given by

$$Z = \dot{\varepsilon}\exp\left(\frac{Q}{RT}\right)$$

(5.6)

In Equation 8.20, Q is the temperature-independent activation energy and $\dot{\varepsilon}$ is the effective strain rate, which with the assumption of infinitesimal deformation is given by

$$\dot{\varepsilon} = \left(\frac{1}{2}\dot{\varepsilon}_{ij}\dot{\varepsilon}_{ji}\right)^{\frac{1}{2}}$$

(5.7)

$$\dot{\varepsilon}_{ij} = \frac{1}{2}\left(\frac{\partial u_i}{\partial x_j} + \frac{\partial u_j}{\partial x_i}\right)$$

(5.8)

The above equations were incorporated into the FLUENT Software using a user definition function (UDF). However, as the UDF does not have the function $\sinh^{-1}$, this function in Equation 8.19 was replaced by

$$\sinh^{-1}\left[\left(\frac{Z}{A}\right)^{\frac{1}{n}}\right] = \ln\left\{\left(\frac{Z}{A}\right)^{\frac{1}{n}} + \sqrt{\left[\left(\frac{Z}{A}\right)^{\frac{2}{n}} + 1\right]}\right\}$$

(5.9)

Figure 5.2 shows the viscosity profiles using the model described above for the Ti-6Al-4V alloy.

Figure 5.2 – Logarithm with a base 10 of the viscosity (Pa.s) profiles for the Ti-6Al-4V alloy as a function of temperature and strain rate.
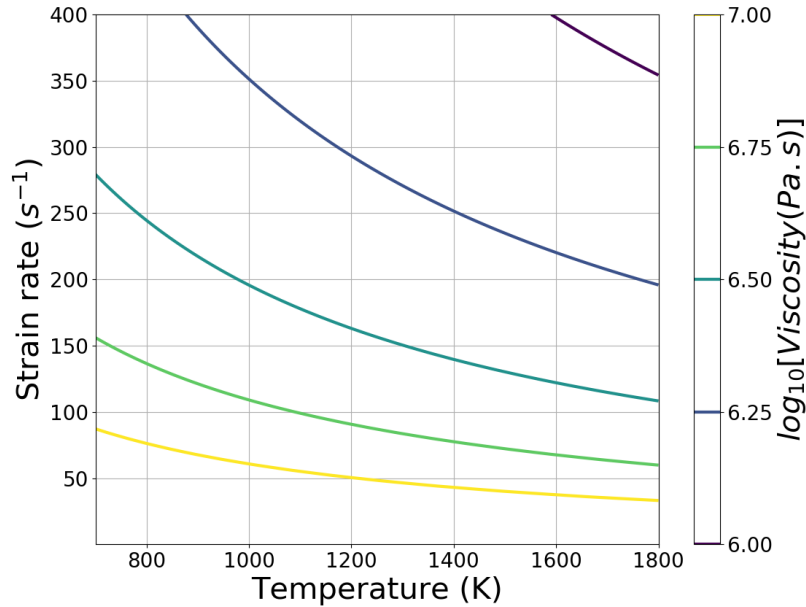
Source: The author

5.3.2.2 *AISI 304 stainless steel flow stress*

The viscosity model for the AISI 304 stainless steel was based on a simplified Hart's model (HART, 1976), where the flow stress (σ_e) is calculated with the sum of σ_p (plastic contributions) and σ_v (viscous contributions).

$$\sigma_e = \sigma_p + \sigma_v \tag{5.10}$$

The plastic contribution is the resistance from the dislocation entanglement and the viscosity contribution represents the frictional force along the slip plane that resists the dislocation glide. In this model, both contributions depend on temperature and strain rate. The plastic and viscosity contributions to the flow stress are given by

$$\sigma_p = k_1 \exp\left[-\left(\frac{b}{\dot{\varepsilon}}\right)^{\lambda}\right] \tag{5.11}$$

$$b = b_0 \left(\frac{k}{G}\right)^N \exp\left[-\left(\frac{Q}{RT}\right)\right] \tag{5.12}$$

$$\sigma_v = G \left(\frac{\dot{\varepsilon}}{G} \right)^{1/M} \tag{5.13}$$

$$a = a_0 \exp \left[- \left(\frac{Q^0}{RT} \right) \right] \tag{5.14}$$

where T is the absolute temperature (K) and R is the universal gas constant. The other constants are material parameters and they are determined from experiments. These parameters were determined by Cho *et al.* (2005), who developed a study about the modeling strain hardening and texture evolution of the 304 stainless steel in FSW.

The k_1 parameter is the maximum value of the viscosity contribution to the stress flow. The saturation value of k_1 depends on the temperature and strain rate, wherein Hart's model it is replaced by one with a Voce-like saturation limited state variable and k_1 can be calculated using Equations 8.29 and 8.30.

$$k_1 = \left(\frac{C}{\varphi} \right)^{m_0} \tag{5.15}$$

where the Fisher factor is given by Fisher (FISHER, 1966) as

$$\varphi = T.\ln \left(\frac{D_0}{\dot{\varepsilon}} \right) \tag{5.16}$$

Figure 6.2 shows the viscosity profiles as a function of the strain rate and temperature using the above described model.

Figure 5.3 – Logarithm with a base 10 of the viscosity (Pa.s) profiles for the 304 stainless steel as a function of temperature and strain rate.
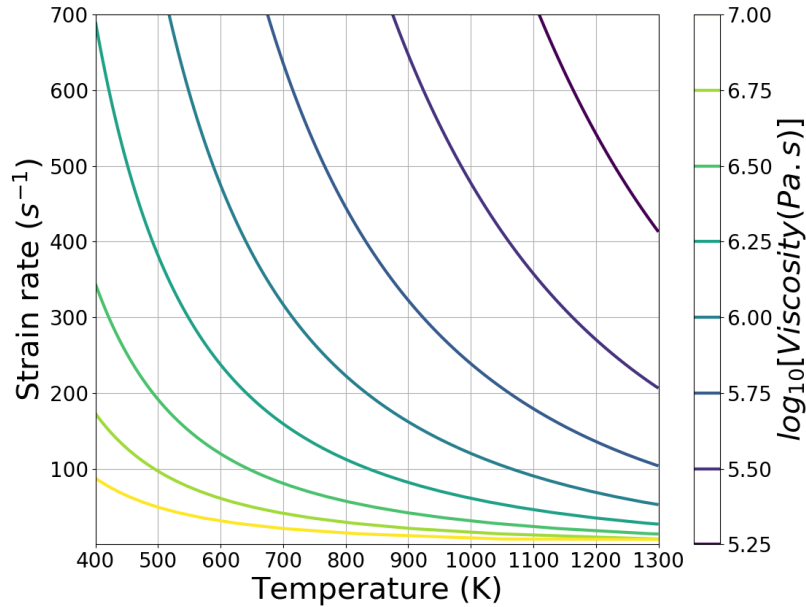
Source: The author

5.3.3 *Heat source models for the Ti-6Al-4V alloy and 304 stainless steel*

The heat source was also added to the commercial software Fluent by means of UDF (user definition functions). The S_i source term is defined by

$$S_i = q_1 \frac{A_r}{V} \tag{5.17}$$

where A_r is the contact area between the tool and workpiece and V is the volume enclosing the area A_r. $q_1 [W/m^2]$ is the heat generated by the contact surface between the shoulder tool and workpiece. In this work, (q_1), is evaluated by the following expressions for the 304 stainless steel and Ti-6Al-4V alloy, respectively (NANDAN *et al.*, 2006b; NANDAN *et al.*, 2008b) :

$$q_1 = \left[\delta n \tau + (1-\delta)\mu_f P\right](\omega r - U_1 \sin \theta) \tag{5.18}$$

$$q_1 = \left[(1-\delta)\eta \tau + \delta \mu_f P\right](\omega r - U_1 \sin \theta) \tag{5.19}$$

In the above equations, P is the pressure of the tool during the welding, ω is the angular velocity, U_1 is the welding speed, η is the thermal efficiency, δ is a constant that will

be defined later, μ_f is a friction coefficient, the term composed of $(\omega r - U_1 \sin\theta)$ represents the relative velocity between the tool and workpiece, and $\sin\theta$ is defined by

$$\sin\theta = \frac{y}{r} \tag{5.20}$$

$$\cos\theta = -\frac{x}{r} \tag{5.21}$$

$$r = \sqrt{x^2 + y^2} \tag{5.22}$$

where r is the radius and the global axis is fixed in the center of the tool.

Equations 5.18 and 5.19 represent the same physical phenomenon, the difference between them is only the way they are written. In the first study performed by Nandan *et al.* (2006a), the equation for 304 stainless steel was written in terms of $(1-\delta)$ and the second study also analyzed by Nandan *et al.* (2008b), the equation for the Ti-6Al-4V alloy was written in terms of δ. These terms determine the quantity of the heat that will be generated by friction or deformation. This small difference between the equations was not modified in the present investigation, in order to maintain agreement with the previous works. For AISI stainless steel 304, δ was kept constant and equal to 0.7, while for the Ti-6Al-4V alloy we used the model defined in Deng *et al.* (2001) that is given by

$$\delta = 1 - \exp\left(-\delta_0 \frac{\omega}{\omega_0} \frac{r}{R_s}\right) \tag{5.23}$$

where R_s is the radius of the shoulder , δ_0 is a constant, and ω_0 is a dimensionless constant for the rotational speed, ω. The friction coefficient (μ_f) was kept constant and equal to 0.4 for the stainless steel and the following expression given in Kong e Ashby (1991) was used for the Ti-6Al-4V alloy:

$$\mu_f = \mu_0 \exp\left(-\delta_0 \frac{\omega}{\omega_0} \frac{r}{R_s}\right) \tag{5.24}$$

In Equation 8.4, $S_b[W/m^3]$ is a heat source term generated by the plastic deformation in the contact of the workpiece and the tool. Alike the S_i term, the UDF from Fluent software was

used to implement S_b in W/m^3 from the above equations. This source term has been calculated as $f_m \mu \Phi$, where μ is the viscosity, f_m is an arbitrary constant that indicates the extent of atomic mixing in the system. In this study, a value of 0.04 was used for f_m and Φ (CHO *et al.*, 2013) is given by

$$\Phi = 2\left(\left(\frac{\partial u_1}{\partial x_1}\right)^2 + \left(\frac{\partial u_2}{\partial x_2}\right)^2 + \left(\frac{\partial u_3}{\partial x_3}\right)^2\right) + \left(\frac{\partial u_1}{\partial x_2} + \frac{\partial u_2}{\partial x_1}\right)^2 \\ + \left(\frac{\partial u_1}{\partial x_3} + \frac{\partial u_3}{\partial x_1}\right)^2 + \left(\frac{\partial u_3}{\partial x_2} + \frac{\partial u_2}{\partial x_3}\right)^2 \tag{5.25}$$

The heat generated by plastic deformation and friction between the contact of the tool and workpiece are split between them. The fraction that is inputted to the plate (f) is defined by Nandan *et al.* (2008b) as

$$f = \frac{J_w}{J_t + J_w} \tag{5.26}$$

where J_w(workpiece) and J_t(tool) are defined by the following equation:

$$J_i = \sqrt{(\rho C_p k)_i} \; ; i = w \text{ or } t \tag{5.27}$$

A convection boundary condition was also established on all faces of the plate. For the top of the plate the loss of heat through radiation was added to the convection. Once these conditions are established, the boundary conditions for the bottom, side, and top of the plate are respectively given by the following equations:

$$k\frac{\partial T}{\partial z} = h_b\left(T - T_a\right) \tag{5.28}$$

$$\pm k\frac{\partial T}{\partial y} = h_s\left(T - T_a\right) \tag{5.29}$$

$$-k\frac{\partial T}{\partial z} = h_t\left(T - T_a\right) + \sigma\varepsilon(T^4 - T_a^4) \tag{5.30}$$

where h_b(125 KW/m^2 for 304 stainless steel and 418 kW/m^2 for Ti-6Al-4V alloy), h_s(30 KW/m^2), and h_t(30 KW/m^2) are the heat convection coefficients for bottom, side, and top of

the workpiece, respectively, T_a is the environment temperature, and k is the thermal conductivity of the workpiece.

At the boundaries, the velocities in the contact regions between the tool and workpiece were set. For the shoulder, the velocity components are given by

$$v_x = (1 - \delta)(\omega r \sin \theta - U_1) \tag{5.31}$$

$$v_y = (1 - \delta)(\omega r \cos \theta) \tag{5.32}$$

The velocity of the contact between the tool pin and workpiece is defined by

$$v_x = (1 - \delta)(\omega R_p \sin \theta - U_1) \tag{5.33}$$

$$v_y = (1 - \delta)(\omega R_p \cos \theta) \tag{5.34}$$

where R_p is the radius of the pin. All velocity components were implemented in the Fluent simulator using the UDF. All experimental parameters such as size of the workpiece, thermal conductivity, welding speed are presented in the Appendix A and B.

5.4   Results and Discussions

In this study, a hexahedral mesh for the simulations of both materials was used. Mesh refinement tests were performed on the geometry used to simulate the AISI 304 stainless steel and the titanium alloy before the tests with different viscosity truncation values. One example of the mesh used in these simulations is shown in Figure 5.4. These meshes have a radial growth because this format allows the region, where the tool is located to have the smallest elements with the rest of the domain having elements of the same size. This mesh model has been observed in other studies(ZHANG *et al.*, 2018). The tool region has a dense grid, with aim of capture the sharp thermal gradients around the workpiece more effectively.

Figure 5.4 – Example of a mesh used in the simulations.
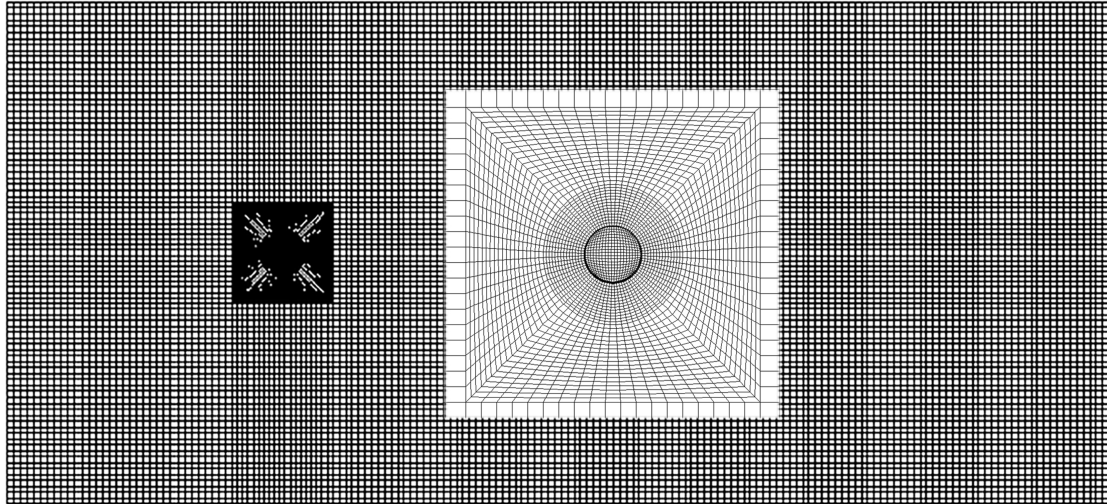
Source: The author

All meshes were constructed as shown in Figure 8.4, changing only the number of elements and keeping the dimensions of the workpiece. Three different meshes were tested for both materials. The titanium alloy simulations were performed using meshes with the following number of elements: 1,038,058, 2,875,307, and 4,467,071.

Figure 5.5 presents the temperature profile for the titanium alloy along the length of the plate and located 3.17 mm from the center of the tool using the three grids. From this figure, it is possible to observe that the temperature profiles do not change much when the number of elements of the grid are increased. There were some minor differences in the temperature peak and a faster cooling of the plate, when the mesh was refined. However, the differences observed in the cooling stage of the welding cycle did not change the phase properties of the workpiece, since the differences as shown in 5.5 were verified for temperatures close to the ambient temperature. To be conservative, the mesh with 2,875,307 elements was chosen for the investigation of the titanium alloy.

Figure 5.5 – Mesh refinement study for Ti-6Al-4V
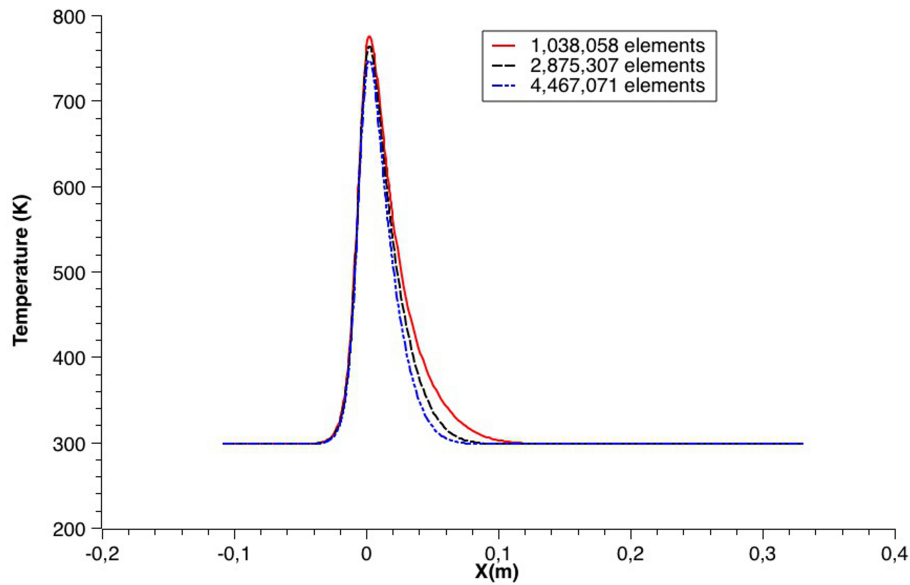
Source: The author

A similar refinement mesh study was carried out for the AISI 304 stainless steel using the same geometry. Once again, three meshes were used, but now the following number of elements were tested: 965,556, 1,767,696, and 2,743,742. The temperature profile at the position already presented for the titanium alloy is shown in Figure 5.6. From this figure, it can be observed that any major variation was observed with all the used grids. However, in order to be conservative for the investigation of the maximum valor of the viscosity performed in this section, the mesh with 1,767,696 elements was chosen. Herein, just to demonstrate that the chosen grid is enough refined, it is important to mention the three-dimensional numerical investigation for the 409 stainless steel performed by Cho *et al.* (2013) using a mesh composed of 356,862 hexahedral elements for a geometry greater than the one investigated in this work.

Figure 5.6 – Mesh refinement study for AISI 304 stainless steel
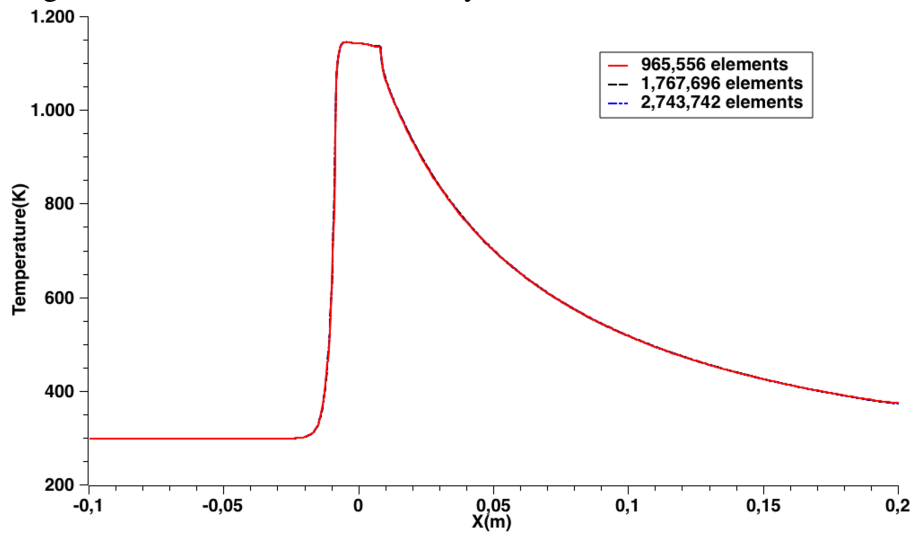
Source: The author

After the mesh refinement study, the simulation results were compared with the ones presented for the AISI 304 stainless steel (NANDAN *et al.*, 2006a) and Ti-6Al-4V alloy (NANDAN *et al.*, 2008b). Figures 5.7 and 5.8 present the temperature profile for the AISI 304 stainless steel and Ti-6Al-4V alloy, respectively. Based on these figures, although minor differences were observed, we can verify a good agreement between our results and the ones from Nandan *et al.* (2006a) and Nandan *et al.* (2008b). Furthermore, no grid refinement study was presented in the above cited works. Finally, the minor difference between the simulated results for both materials did not exceed three percent (3%).

Having performed the grid refinement study and validated the simulations with the numerical results from the literature, it is now investigated the maximum physical value that can be set for the viscosity of the two materials under analysis. Although the maximum viscosity is finite for both investigated materials, the numerical models proposed in the literature result in infinity values when low values of temperature and strain rate are achieved.

Three possible truncation values , shown in Table 7.1 for both materials, were tested in this study.

Material	Truncation
	$10^7 Pa.s$
AISI stainless steel 304	$10^8 Pa.s$
	$10^9 Pa.s$
	$10^7 Pa.s$
Ti-6Al-4V Alloy	$10^8 Pa.s$
	$10^9 Pa.s$

Table 5.1 – Maximum value for the viscosity of each material investigated

Figure 5.7 – Comparison of the temperature profiles for the AISI 304 stainless steel. Data evaluated at y=18mm on the retreating side on the top of the workpiece.
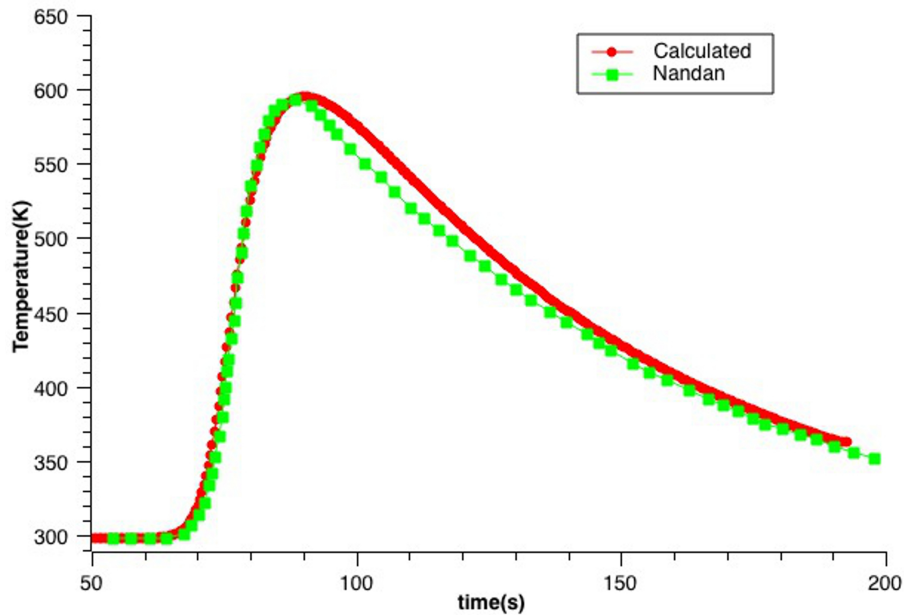
Source: The author

Figure 5.8 – Comparison of temperature profiles for the Ti-6Al-4V alloy. Data evaluated at y=3.17mm on the advancing side on the bottom surface of the workpiece.
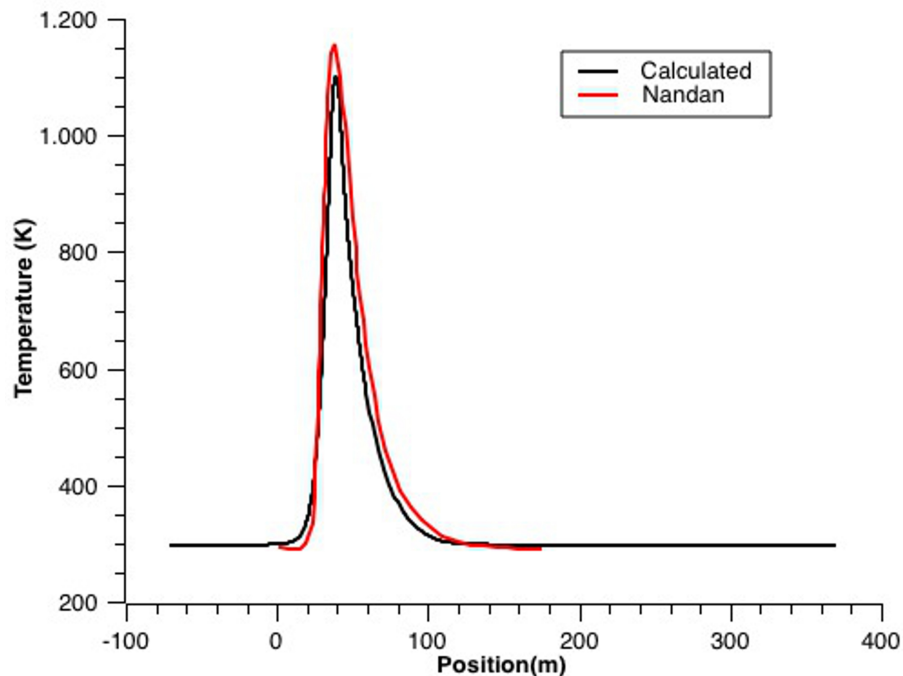
Source: The author

Figure 5.9 presents the temperature field for both materials using the three maximum values of viscosity presented in Table 7.1. The effect of increasing the viscosity is to elongate the temperature field in the axial direction, especially for the AISI 304 stainless steel. It is also noted

that the maximum temperature decreases when the maximum viscosity increases. The maximum viscosity value that results in the closest expected temperature field to the ones presented in the literature was equal to $10^7 Pa.s$. However, in the literature, there is no mention to the maximum viscosity value used (CHO *et al.*, 2013; NANDAN *et al.*, 2007; NANDAN *et al.*, 2008b). Finally, it is important to stress that the expected temperature fields are the ones shown in Figures 5.9a and 5.9b for both materials.

Figure 5.9 – Temperature field for different maximum values of viscosity. (a) and (b) 10^7 Pa.s. (c) and (d) 10^8 Pa.s. (e) and (f) 10^9 Pa.s
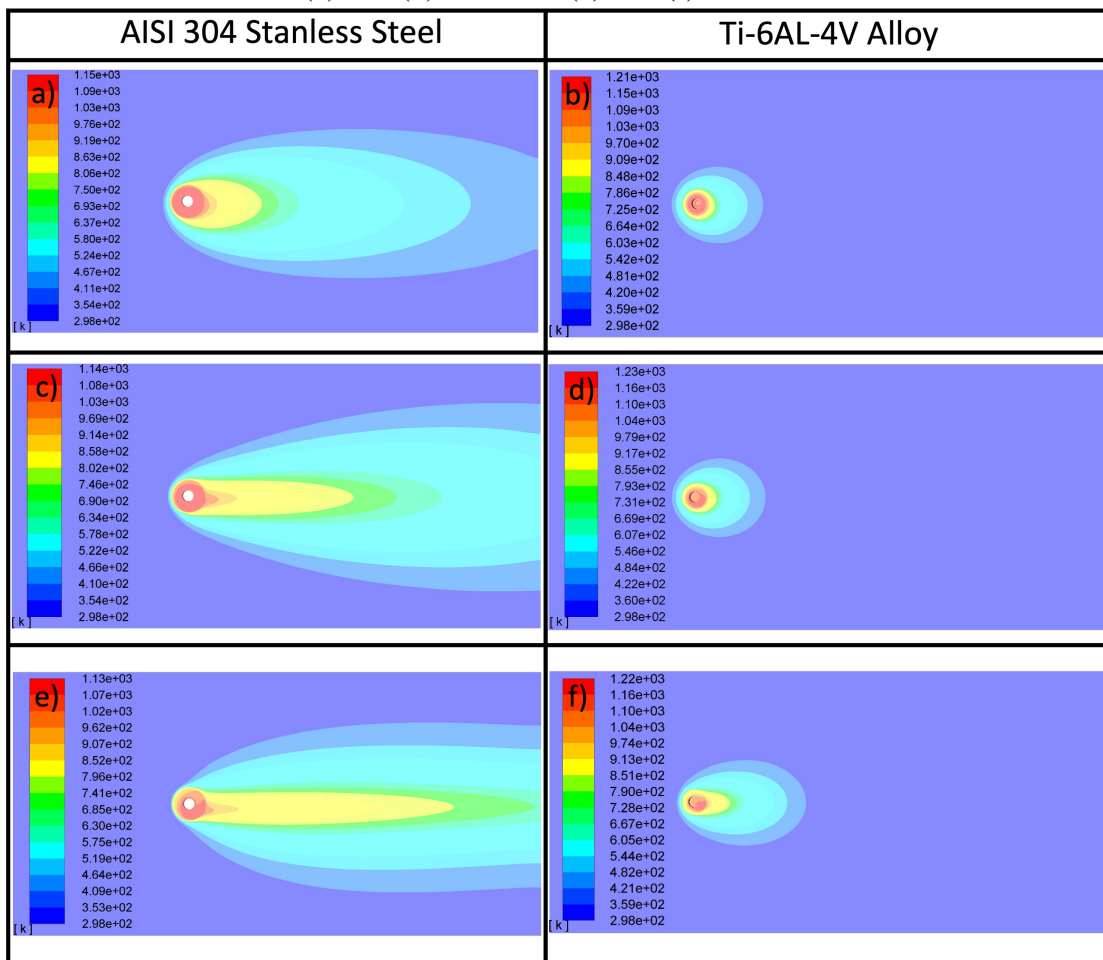
Source: The author

To shed some light on the temperature field behavior, it is presented in Figure 5.10 the viscosity field of each material for the three maximum values of viscosity investigated. From this figure, it is possible to observe that the region where the viscosity field changes also increase away from the tool, especially for the 304 stainless steel. This behavior is justified because the 304 stainless steel is more ductile than the Ti-6Al-4V, and therefore the variation in viscosity has a greater impact on the temperature field and vice-versa. Finally, if a maximum viscosity

equal to $10^7 Pa.s$ is selected, for both materials, the temperature field is in good agreement with the previous results from the literature as it was shown in Figure 5.9. Also, when the maximum viscosity equal to $10^7 Pa.s$ is chosen, it is possible to verify that the viscosity field, for both materials, changes only in the region of the tool, which is the region where the material deformation is expected.

In FSW, the thermo-mechanically affected zone does not propagate to regions far from the tool. The results of Yaduwanshi *et al.* (2016) show that the weld zone has approximately the same size as the shoulder.

Figure 5.10 – Viscosity field for different maximum values of viscosity. (a) and (b) 10^7 Pa.s. (c) and (d) 10^8 Pa.s. (e) and (f) 10^9 Pa.s
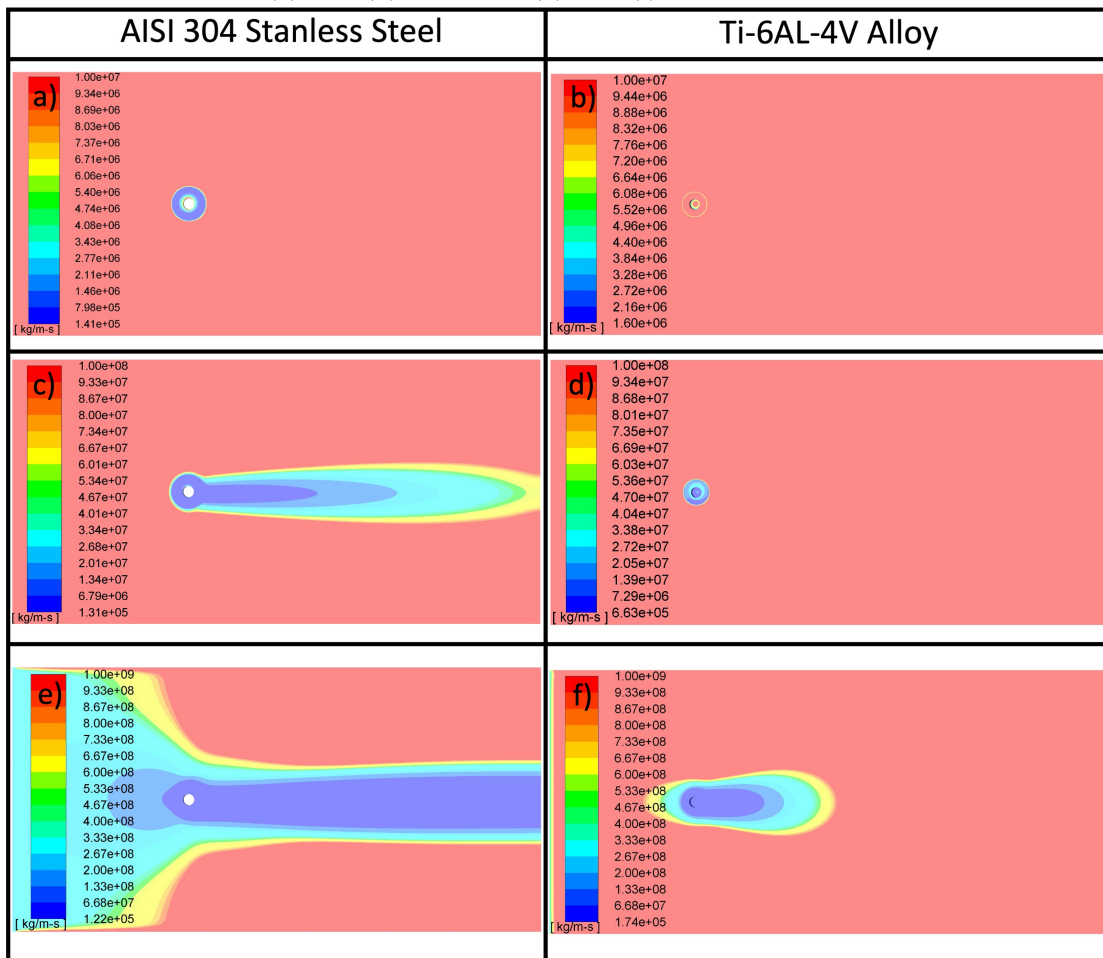
Source: The author

Aiming to investigate the effect of the maximum value of viscosity in the velocity field, the viscosity and velocity profiles (Figure 5.11) are plotted along the welding direction and close to the pin. We choose this line because it is possible to observe the behavior of the two proprieties behind and in front of the tool. Figure 5.11 shows that when the viscosity reaches values close to $10^7 Pa.s$ the velocity tends to zero. These values are in agreement with the results described by Nandan *et al.* (2006a) using AISI 304 stainless steel and Nandan *et al.* (2008b) Ti-6Al-4V alloy. According to the work of Nandan *et al.* (2006a) using 304 stainless steel there is no significant flow of material for viscosities larger than $4 \cdot 10^6 Pa.s$. For titanium alloy, the work performed by Nandan *et al.* (2008b) demonstrated that the flow of the material is negligible for viscosities greater than $10^7 Pa.s$.

Figure 5.11 – Velocity and viscosity profiles as a function of position - maximum value of viscosity equal to $10^7 Pa.s$ (a) AISI 304 stainless steel simulations (b) Ti-6Al-4V alloy simulations.
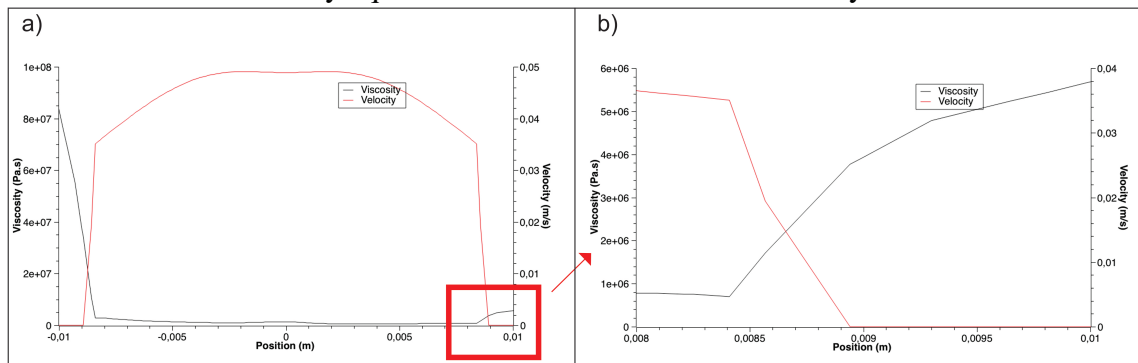
Source: The author

As the maximum viscosity value does not affect the range of where the velocity becomes null, we decided to verify the behavior of the velocity field around the shoulder for both materials; the velocity field in this region is shown in Figure 5.14 at the top of the workpiece and next to the shoulder. As we can see from Figure 5.14, when the maximum value of viscosity is increased there is a region behind the tool that has a velocity different from zero. Therefore, the reason the temperature field presents an elongated shape, see Figures 5.9c-f, is due to the advected energy carried out by this non-null velocity region. As the material remains in solid-state, there is no physical reason to have non-null velocity regions farther away from the tool, as shown in Figures 5.14b and 5.14d, for both materials.

Figure 5.14 – Velocity field at the top of the workpiece. (a) 10^7 Pa.s, (b) 10^9 Pa.s for 304 steel and (c) 10^7 Pa.s and 10^9 Pa.s for Titanium alloy
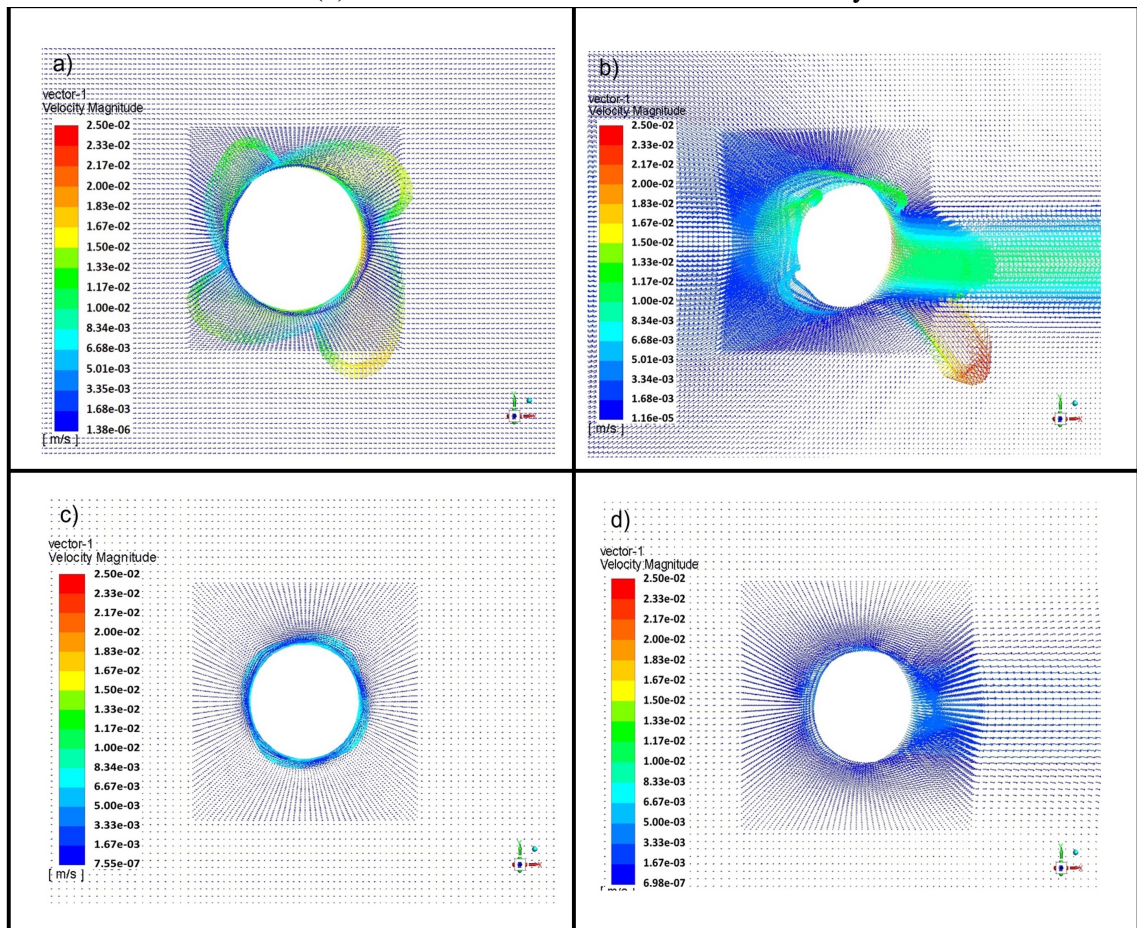
Source: The author

5.5 Conclusions

In this work, the simulation of the friction stir welding (FSW) process of two different materials was investigated. One key parameter in FSW is the maximum viscosity of the material to be used in the simulation for small values of temperature and strain rates of the welded material. In theory, this value goes towards infinity for small values of temperature and strain rate. Herein, we demonstrated using several values of maximum viscosity the point where the viscosity function needs to be truncated and the physical reasons for that truncation. The numerical experiments showed that the temperature and velocity fields depend on the maximum value of the viscosity of the material used, and the maximum value needs to be truncated when the velocity field tends to be null. If we allow the viscosity to be larger than this maximum value, the temperature field will become elongated in the axial direction of the welding due to an increase in the velocity field near the tool.

6 NUMERICAL INVESTIGATION OF THE INFLUENCE OF FSW PARAMETERS ON THE HEAT AND MASS TRANSFER OF THE AUSTENITIC STAINLESS STEELS

6.1 Review

This work analyzed the simulation of austenitic stainless steel, in order to predict defects during the FSW. To predict problems with the material flow, a discrete phase simulation was used, where inert particles were injected into the fluid and observed their paths in the plate. This method proved to be efficient to observe when the material flow becomes inefficient and consequently favoring the formation of defects. A parameter was also elaborated that relates the formation of flashes with the pressure, rotation and minimum viscosity during welding.

6.2 Introduction

Since the advent of Friction Stir Welding (FSW) in 1991, which was developed by The Welding Institute (TWI)(THOMAS *et al.*, 1991), different materials have been welded successfully by this technique including stainless steels. Initially, the FSW technique was used for low melting point alloys such as aluminum and magnesium. Thomas e Nicholas (1997) described the advantages of FSW in aluminum alloys for the transportation industries. However, the development of new materials for the FSW tool has enabled other metals, such as steels, to be welded by the FSW technique. Nandan *et al.* (2006a) described the welding of austenitic stainless steel using a tungsten tool and Cho *et al.* (2013) welded ferritic stainless steel using a PCBN tool.

In addition to the material of the tools used, the geometry of the tools have also been studied (KIM *et al.*, 2017); different geometries can change the mixture between the materials and even develop new techniques, such as the Friction Stir Process (FSP) and stationary shoulder friction stir lap(PATEL *et al.*, 2019b; WEN *et al.*, 2019; SU *et al.*, 2019). FSP uses the plastic deformation caused by the tool to promote dynamic recovery and recrystallization, aiming to improve the mechanical and metallurgical properties of the surface of the materials(PATEL *et al.*, 2019b). The latter uses a tool, in which the shoulder is static and the pin rotates. This technique reduces the welding temperature compared to the conventional FSW, and because most of the heat is generated by the pin this can improve the surface finish (WEN *et al.*, 2019; SU *et al.*, 2019). Therefore, the FSW has been a precursor process, in developing new techniques.

FSW has many advantages over fusion welding processes. When compared to arc welding, FSW has a lower peak temperature, which is on average 80% of the melting temperature of some metals and alloys. FSW can also refine the grain of some materials when welded; for example, Sato *et al.* (2005b) showed that FSW significantly refined the ferrite and austenite phases through dynamic recrystallization. Due to these and other advantages of the FSW process over the traditional welding processes, various studies, have, over the last two decades, simulated these complex phenomena.

Despite the numerous advantages of the FSW, the correct combination of parameters is essential to obtain good results. These parameters are responsible for the heat input and material flow during welding. Low thermal input is known to cause problems in the material mixture, such as voids (MENG *et al.*, 2021), wormholes, and scalloping. On the other hand, excessive high thermal input causes other types of defects, such as root flow, faying surface, and collapsed nugget. Arbegast (2008) studied the influence of FSW parameters on the formation of these defects, classifying them in terms of categories and associating them to parameters such as hot and cold, due to their contribution to the thermal input. According to him an ideal combination of such parameters that prevents the flow-related defects occurs when stick-slip wiping flow takes place and the material flow in front of the pin is exactly balanced with the material flow behind the tool.

These flow-related defects can damage the material properties, decreasing the tensile strength of the weld (KHAN *et al.*, 2015), deteriorate the fatigue lifetime (KAINUMA *et al.*, 2008; ZHOU *et al.*, 2006), favor corrosion and cause problems such as stress concentration and surface finishing (ZHENG *et al.*, 2017).

Observing the various physical phenomena involved and the need to choose the correct parameters to obtain a good weld, simulation appears as an excellent tool to understand and predict problems that could occur during a welding. The first simulations performed by Frigaard *et al.* (2001) with aluminum considered the heat generated by friction but these authors did not take into account the heat generation by plastic deformation.

The evolution of computational tools has enabled other important phenomena to be simulated. The flow of the material around the tool was proposed by Seidel e Reynolds (2003) based on 2D fluid flow. Initially, these authors used the viscosity model proposed by Sellars e Tegart (1972) and later on they used the viscosity model modified by Sheppard e Wright (1979); in this model, the viscosity was a function of the temperature and the strain rate.

Ulysse (2002) used the viscosity model of Sheppard e Wright (1979) to develop a 3D model for friction stir welding. The same approach has been used to investigate the FSW technique in other materials; for example in the studies developed by Nandan *et al.* (2006a) with austenitic steel, by Cho *et al.* (2013) with ferritic steel, by Nandan *et al.* (2008b) with a titanium alloy and by Zhu *et al.* (2016) with welding AA2024-T4.

The significant improvements in the simulation models have also made it possible to predict many defects in the FSW process, which in turn have minimized the number of experimental tests necessary. In this work, the simulations of the AISI 304L are validated through different experimental tests. The validated numerical results were used to forecast the conditions that could give rise to some of the defects frequently found in the FSW of the AISI 304L steel. A parameter was developed to predict flash defects and a new way was used to analyze internal defects due to material flow .

6.3 Materials and experimental data

In this work, seven different welding conditions were simulated with the goal to understand how the axial force, the welding velocity, and the rotational velocity affected the final welded material; the welding conditions are given in Table 7.1. These combinations of parameters were selected from the study developed by Caetano (2016).

Table 6.1 – Experimental parameters investigated

	Axial Force(kN)	Weld Velocity(mm/s)	Rotational Velocity(rpm)
Test 1	35	1	450
Test 2	50	1	450
Test 3	15	1	800
Test 4	20	1	800
Test 5	35	1	800
Test 6	35	1.25	800
Test 7	35	1.50	800

Source: The author

All welds were performed using AISI 304L stainless steel plates of 200x500x4 mm and the samples were joined along the 500 mm side at the Helmholtz Zentrum Geesthacht (HZG) Center, Germany. The FSW equipment used to perform the welds was the HZG gantry system with a PCBN tool and argon as the shield gas. The chemical composition of the AISI 304L stainless steel used in this investigation is given in Table 7.2

The thermal properties of the AISI 304L stainless steel and the tool are in Table

Table 6.2 – Chemical composition of AISI 304L stainless steel(% mass)

Material	Fe	C	Cr	Mn	Ni	P	Si	S	Mo
304L	Bal.	0.026	18.5	1.21	7.94	0.029	0.32	<0.010	0.29

Source: The author

3 and it was constructed using Equations 6.1 (Density), 6.2 (Thermal Conductivity), and 6.3 (Specific Heat).

Table 6.3 – Thermal properties of the materials

Material	Temperature K	Density kg/m^3	Thermal Conductivity $W/m \cdot K$	Specific Heat $J/kg \cdot K$
304L	298	7868.93	15.57150955	505.9717143
	400	7806.18	16.1168	526.13848
	600	7663.80	18.8692	558.05628
	800	7520.51	22.6944	580.02952
	1000	7405.90	26.21	592.243
	1400	7380.96	26.7828	588.12988
	1800	7825.53	9.5284	547.19532
PCBN	298	3450.00	120	750

Source: Almoussawi e Smith (2018)

$$\rho = 7.97 \cdot 10^3 - 6.01 \cdot 10^{-2} \cdot T - 1.12 \cdot 10^{-3} \cdot T^2 + 6.16 \cdot 10^{-7} \cdot T^3 \tag{6.1}$$

$$k = 19.36 - 0.02960 \cdot T + +6.525 \cdot 10^{-5} \cdot T^2 - 2.88 \cdot 10^{-8} \cdot T^3 \tag{6.2}$$

$$C_P = 431.73 + 0.2879 \cdot T - 0.000131237 \cdot T^2 + 3.85 \cdot 10^{-9} \cdot T^3 \tag{6.3}$$

6.4 Physical Model

The main assumptions used in this work are presented here. Due to the heterogeneities at the beginning and end of the weld bead, these regions were not considered in this study. The intermediate section of the weld bead had the same heat input, the same physical properties and cross-section throughout. These characteristics indicate a steady state regime (SONG *et al.*, 2014) throughout the intermediate section of the weld bead; consequently, this study analyzed the FSW considering a steady state regime.

The shoulder was considered to be in contact with the top surface of the workpiece as shown in Figure 6.1. During the welding, the pin is forced to penetrate into the workpiece,

and to a depth that is sufficient to fully stir the workpiece. However, penetration through the plate is undesirable, as the pin should not weld the plate to the backing bar. Thus, a minimum thickness needs to be considered at the bottom of the hole. In this study, the pin length and the thickness of the plate between the tip of the pin and the backing bar were equal to 3.7 mm and 0.3 mm, respectively. Throughout the welding process, the pressure (that is a function of axial force), the rotation, and the welding velocity are assumed to remain constant.

Figure 6.1 – Schematic diagram used in the FSW simulation. a) velocity boundary conditions and b) view of tool from above
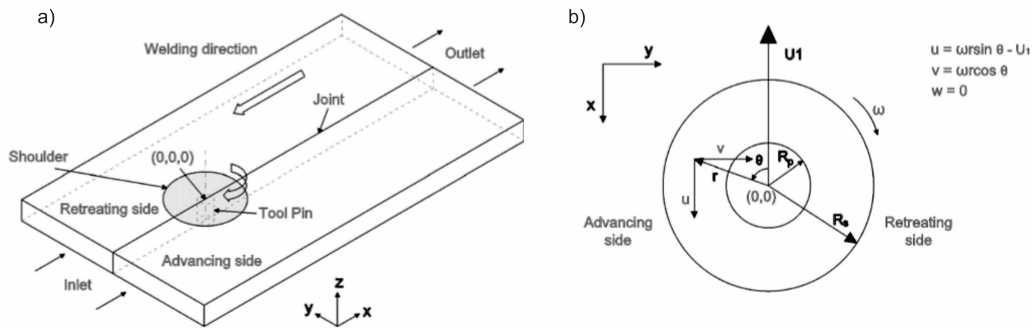
Source: The author

6.4.1 Governing Equations

The material was assumed to be a non-Newtonian, incompressible, and viscoplastic fluid. A partial sticking condition is assumed between the tool and the workpiece and the tilt angle of the tool was equal to zero (NANDAN *et al.*, 2006a). The reference coordinates are fixed in the center of the tool and at the top of the workpiece. The continuity equation is given by

$$\frac{\partial u_i}{\partial x_i} = 0 \; ; i = 1,...,3 \tag{6.4}$$

where u is the velocity of plastic flow in x-(1), y-(2), and z-(3) coordinates. Equation 6.4 states that the volume variation is zero. The momentum conservation equations with reference to a coordinate system attached to the tool using an indicial notation are given by Equation 6.5, where $i = 1, 2$ or 3 (CHO *et al.*, 2013).

$$\frac{\partial \rho u_j}{\partial t} + \frac{\partial \rho u_i u_j}{\partial x_i} = -\frac{\partial P}{\partial x_j} + \frac{\partial}{\partial x_i}\left(\mu \frac{\partial u_j}{\partial x_i}\right) - \rho U \frac{\partial u_j}{\partial x_1} \tag{6.5}$$

where U is the weld velocity, ρ is the density, P is the pressure and μ is the non-Newtonian viscosity of the material. The conservation energy equation is given by

$$\frac{\partial(\rho C_P T)}{\partial t} + \frac{\partial(\rho C_P u_i T)}{\partial x_i} = -\rho C_P U_1 \frac{\partial T}{\partial x_1} + \frac{\partial}{\partial x_i}\left(k\frac{\partial T}{\partial x_i}\right) + S_i + S_b \tag{8.4}$$

The simulations were performed using a steady-state regime. In Equation (8.4) C_P is the specific heat and k is the thermal conductivity. S_i is a source term that denotes the rate of energy per unit of volume dissipated by friction between the tool and workpiece, and S_b denotes the rate of energy per unit of volume generated by plastic deformation in the workpiece away from the interface.

6.4.2 Boundary Conditions and Heat Source

The heat source, Si, is added to the commercial software Fluent by means of UDF (user-defined functions) as a heat flux (q_1) as described by

$$q_1 = \left[\delta\eta\tau + (1-\delta)\mu_f P\right](\omega r - U_1\sin\theta) \tag{6.6}$$

where P is the pressure of the tool during the welding, ω is angular velocity, δ is slip rate, U_1 is welding speed, η is the thermal efficiency, $\tau = \sigma_{yield}/3$ (where σ_{yield} is evaluated using the distortion energy theory for the plane stress) and μ_f is a friction coefficient. The term $(\omega r - U_1\sin\theta)$ represents the relative velocity between the tool and workpiece. The $\sin\theta$ is defined by

$$\sin\theta = \frac{y}{r} \tag{6.7}$$

$$\cos\theta = -\frac{x}{r} \tag{6.8}$$

$$r = \sqrt{x^2 + y^2} \tag{6.9}$$

where r is the radius with the global axis fixed at the center of the tool.

The source term per unit volume, generated by plastic deformation in the workpiece away from the interface (S_b), is defined in Fluent as the heat generation rate in the boundary condition section. This source term is calculated as $f_m \mu \Phi$, where μ is the viscosity, f_m is an arbitrary constant that indicates the extent of atomic mixing in the system. In this study, a value of 0.04 was used for f_m and the viscous dissipation function Φ (CHO *et al.*, 2013) is given by

$$
\begin{aligned}
\Phi = 2\left(\left(\frac{\partial u_1}{\partial x_1}\right)^2 + \left(\frac{\partial u_2}{\partial x_2}\right)^2 + \left(\frac{\partial u_3}{\partial x_3}\right)^2 \right) + \left(\frac{\partial u_1}{\partial x_2} + \frac{\partial u_2}{\partial x_1}\right)^2 \\
+ \left(\frac{\partial u_1}{\partial x_3} + \frac{\partial u_3}{\partial x_1}\right)^2 + \left(\frac{\partial u_3}{\partial x_2} + \frac{\partial u_2}{\partial x_3}\right)^2
\end{aligned}
\tag{6.10}
$$

The S_i and S_b are split between the tool and workpiece. The fraction inputted into the workpiece (f) is defined by (NANDAN *et al.*, 2008b)

$$
f = \frac{J_w}{J_t + J_w}
\tag{6.11}
$$

where J_w(workpiece) and J_t(tool) are defined by the following equation:

$$
J_i = \sqrt{(\rho C_p k)_i} \; ; \; i = w \text{ or } t
\tag{6.12}
$$

In Eq. 8.12, $i = w$ or t for the workpiece and tool, respectively. A convection boundary condition is established for all faces of the plate. For the top of the plate, in addition to the convection heat loss, the thermal radiation is added to the convection flux. After establishing these conditions, the boundary conditions for the bottom, side, and top of the plate are respectively given by the following equations:

$$
k\frac{\partial T}{\partial z} = h_b \left(T - T_e\right)
\tag{6.13}
$$

$$
\pm k\frac{\partial T}{\partial y} = h_s \left(T - T_e\right)
\tag{6.14}
$$

$$
-k\frac{\partial T}{\partial z} = h_t \left(T - T_e\right) + \sigma\varepsilon(T^4 - T_a^4)
\tag{6.15}
$$

where h_b, h_s and h_t are the coefficient heat convection for bottom, side and top of the workpiece, respectively, T_e a is the environment temperature, and k is the thermal conductivity.

The velocities in the contact region between tool and workpiece were set in the boundary conditions. For the shoulder, the velocity components are given by

$$v_x = (1 - \delta)(\omega r \sin\theta - U_1) \tag{6.16}$$

$$v_y = (1 - \delta)(\omega r \cos\theta) \tag{6.17}$$

For the contact between the tool pin and workpiece, the velocity components are defined by

$$v_x = (1 - \delta)(\omega R_p \sin\theta - U_1) \tag{6.18}$$

$$v_y = (1 - \delta)(\omega R_p \cos\theta) \tag{6.19}$$

where R_p is the radius of the pin. All velocity components were implemented in the Fluent simulator using UDF. All experimental parameters such as size of the workpiece, thermal conductivity, welding speed are shown in Appendix C.

6.4.3   AISI 304 stainless steel flow stress

The flow stress for the AISI 304L stainless steel followed a viscosity model based on the simplified Hart's model (HART, 1976). In this model the flow stress (σ_e) is calculated using the sum of σ_p (plastic contribution) and σ_v (viscous contribution).

$$\sigma_e = \sigma_p + \sigma_v \tag{8.24}$$

The plastic contribution is the resistance of dislocation entanglement and the viscosity glide. In this model, both plastic and viscosity contributions depend on the temperature and strain rate, and are given by

$$\sigma_p = k_1 \exp\left[-\left(\frac{b}{\dot{\varepsilon}}\right)^\lambda\right] \tag{8.25}$$

$$b = b_0 \left(\frac{k}{G} \right)^N \exp\left[-\left(\frac{Q}{RT} \right) \right] \tag{8.26}$$

$$\sigma_v = G \left(\frac{\dot{\varepsilon}}{a} \right)^{1/M} \tag{8.27}$$

$$a = a_0 \exp\left[-\left(\frac{Q^0}{RT} \right) \right] \tag{8.28}$$

where T is the absolute temperature (K) and R is the universal gas constant. The other constants are material parameters and they are determined from the experiments. These parameters were determined by Cho *et al.* (2005), who developed a study about the modeling of strain hardening and texture evolution of the 304 stainless steel in FSW. The k_1 parameter is the maximum value of viscosity contribution for the stress flow. The saturation value of k_1 depends on temperature and strain rate; however in Hart's model it is replaced by Equations 8.29 and 8.30 (CHO *et al.*, 2005).

$$k_1 = \left(\frac{C}{\varphi} \right)^{m_0} \tag{8.29}$$

where the Fisher factor φ is given by (FISHER, 1966):

$$\varphi = T.\ln\left(\frac{D_0}{\dot{\varepsilon}} \right) \tag{8.30}$$

Figure 6.2 shows the viscosity profiles as a function of the strain rate and temperature.

Figure 6.2 – Logarithm base 10 of the viscosity (Pa.s) profiles for the 304
stainless steel as a function of temperature and strain rate.
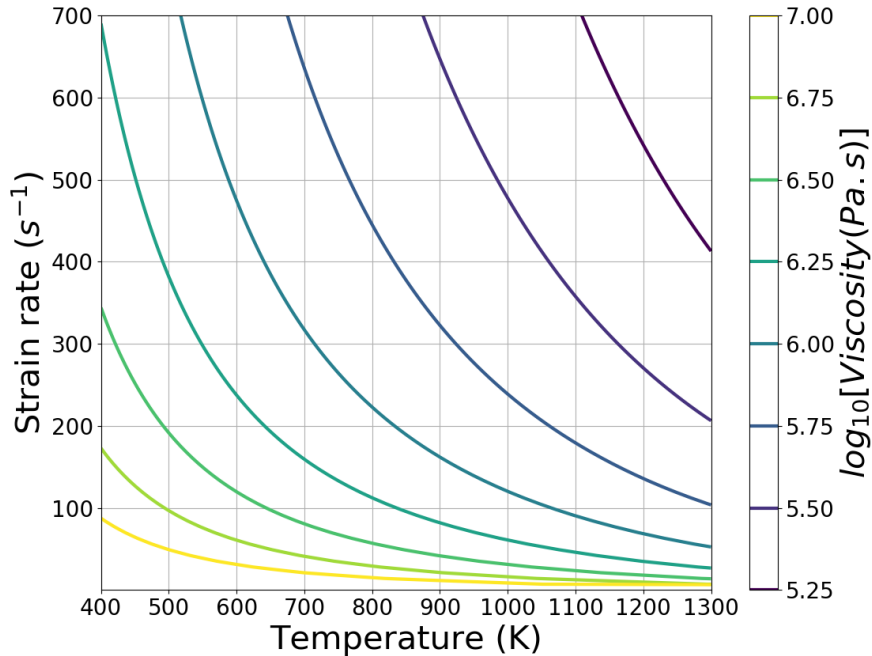
Source: Silva *et al.* (2020b)

6.5 Results and Method

All simulations performed in this work used a non-uniform grid composed of only hexahedron elements that was modeled using the ICEM-Mesh Software. As shown in Figure 6.3, local grid refinement was performed in the tool region, since this is the area where the gradients are expected to be higher. Therefore, based on the work of Silva *et al.* (2020b), a grid refinement study with 1,227,002 volumes and 1,296,068 nodes was chosen for all simulations presented in this section.

The numerical results in terms of temperature cycles of this work were compared with the experimental results of Caetano (2016), who evaluated the temperature cycles during the welding of AISI 304 stainless by FSW. In the experimental study performed by Caetano (2016), six thermocouples were positioned on the top surface of the steel plate, at positions 15, 20, and 25 mm away from the weld centerline; three thermocouples were positioned on the advanced side and the other three were placed on the retreating side of the weld. The weld bead width was equal to 23.6 mm; consequently, the distance from the tool to thermocouples was 3.2 mm, 8.2 mm, and 13.2 mm, respectively. Figure 6.4 shows the comparison in terms of the temperature cycles between experimental and simulation results for Test 1. This Figure

Figure 6.3 – Hexahedron grid with 1,227,002 volumes and 1,296,068 nodes used for all
    simulations.
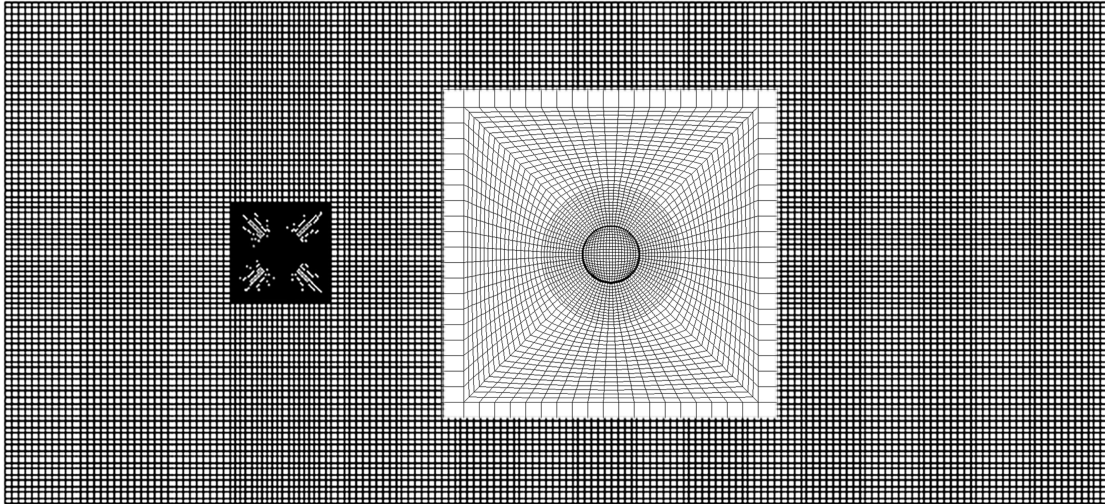
Source: The author

shows that the temperature peaks reached in the simulated results were very close to the peaks
determined experimentally, for both sides of the weld bead. Although some minor differences
between the numerical and the experimental results were observed, especially those furthest
away from the pin, the differences did not exceed $50K$.

Figure 6.4 – Comparison between thermocouples and simulation in different positions
    along the welding line.
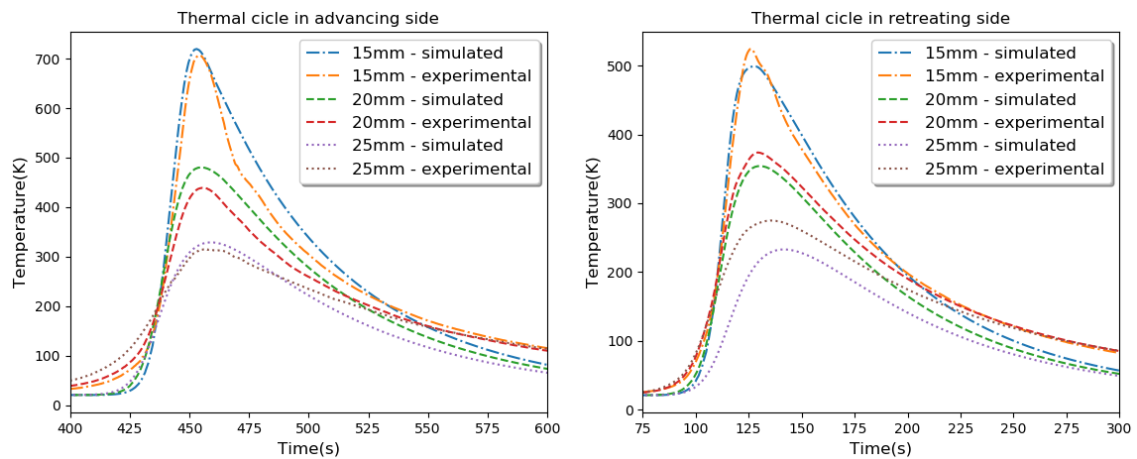
Source: The author

After the validation of the numerical approach used in this work, we investigated the effect of different welding conditions presented in Table 7.1 on the material and weld bead quality.

As shown in Section 8.5.4, the viscosity depends on the strain rate and temperature. Table 6.4 presents the maximum temperature and viscosity on the top of the workpiece and stain rate at the same point in order to observe the influence of each combination of parameters of Table 7.1 on the viscosity. The results showed that the strain rate and temperature have a great influence on the minimum viscosity.

Comparing Test 1 and Test 4 that have approximately the same temperature (only 2.39 % difference) but have a large difference in terms of strain rate (approximately 76.58 % difference), the variation in viscosity is 42.24 %. However, when comparing Test 1 with Test 2 that have the same strain rate and difference in temperature of almost the reverse of the previous case (temperature difference of 16.04 %) and strain rate (variation of 1%), the viscosity changes about 43.24%. Although, the influence of temperature in the viscosity is larger than the strain rate, the effect of both on viscosity cannot be neglected.

Table 6.4 shows that some tests reached temperatures above or close to the melting point of the steel. These overheated regions occur in thin layers, especially those close to the contact surface with the tool because the simulation does not predict the loss of mass caused by excessive axial force or intense plasticizing. In addition, the friction coefficient used in the current model is constant. Consequently, extreme temperatures should be carefully analyzed because previous studies have shown that in extreme conditions the maximum temperature should be artificially defined (MA *et al.*, 2018). However, in practice, those regions in which the simulation predicted temperatures as high as the melting point would reach a visco-elastoplastic state capable of allowing the material to escape from the nugget in the form of flashes.

The physical model applied in this work has been successfully used to predict the temperature distribution for the group of parameters in which there was a low heat generation or low tendency for flash production, as shown in Figure 6.5. However, when this model is applied to a set of parameters that resulted in high heat generation, it fails to predict a reasonable temperature. Depending on the combination of high rotation speed, high intensity of axial force, or low welding velocity, the heat generated is too high, indicating that the temperatures are too high for practical purposes.

Therefore, in this later case, where it failed to predict the temperature field correctly

in the contact region between the workpiece and the pin, because it did not consider that the plasticized material will be forced to flow out of the nugget. However, it physically expected that the material in the regions mentioned above is expelled in a solid-state before reaching the extremely high temperatures. Some aspects of these problems are commented on in the text of this section.

Table 6.4 – Investigation into the effect of the temperature and stain rate on the viscosity. *The higher temperatures do not occur in practice, they occur due to the method limitations, as discussed in the text

Test	Maximum temperature	Maximum strain rate	Minimum viscosity
1	1383.87 K	$235.12s^{-1}$	$1.85 \cdot 10^4 kg/m.s$
2	1606.05* K	$249.24s^{-1}$	$1.07 \cdot 10^4 kg/m.s$
3	1325.33 K	$425.99s^{-1}$	$1.47 \cdot 10^4 kg/m.s$
4	1426.57 K	$428.65s^{-1}$	$1.08 \cdot 10^4 kg/m.s$
5	1875.66* K	$471.97s^{-1}$	$0.46 \cdot 10^4 kg/m.s$
6	1777.18* K	$474.49s^{-1}$	$0.47 \cdot 10^4 kg/m.s$
7	1733.79* K	$477.13s^{-1}$	$0.40 \cdot 10^4 kg/m.s$

Source: The author

Figure 6.5 presents the temperature distribution at the center of the pin for all welding conditions presented in Table 1. The results clearly verified that the heat generated for high rotation, axial force, and low weld velocity will contribute to a temperature above the melting point close to the contact surface.

Figure 6.5 – Temperature cross section at the center of the pin. a) Test 1, b) Test 2, c) Test 3, d) Test 4, e) Test 5, f) Test 6, g) Test 7
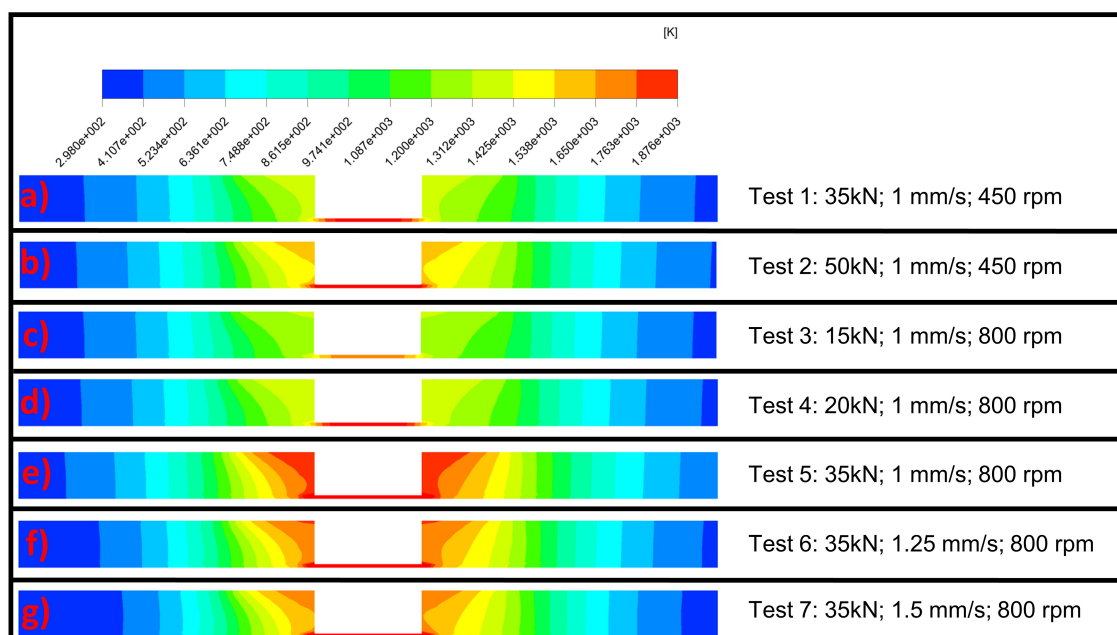
Source: The author

As previously mentioned, the model used in this work does not take into account the loss of mass that occurs during the welding under certain conditions. In addition, it does not consider the reduction of the friction coefficient. Thus, the effect of the friction coefficient on the temperature field was evaluated in additional tests. The reduced friction coefficient of test 5 (1 mm/s, 35 kPa and 800 rpm) is shown in Figure 6.6. These additional tests were designed to observe how the friction coefficient can influence the maximum temperature reached. Figure 6.6 shows that the temperature of the welded region has decreased to levels close to 80% of the melting temperature, as can be seen in Figure 6.6c. Su *et al.* (2014) simulated the FSW welding of aluminum alloy under different conditions and their friction coefficient (μ_f) and slip rate(δ) were not constant and changed with the welding conditions, which represents the slip ratio between the tool and the base metal. When $\delta = 1$ is a sticking condition, when $\delta = 0$ is a sliding conditions and only values between 0 and 1 is a sticking/sliding condition(SCHMIDT *et al.*, 2003). In the present study, there are no experimental results taken from the hotter tests which would permit adjustments and correction in this model; thus ensuring accuracy for the entire range of parameters tested, specifically from the temperature distribution point of view. However, the goal of the above tests is to show that the friction coefficient (μ_f) will have a significant influence on the maximum temperature reached, and that future studies on the FSW process of stainless steel are still necessary to develop functions for variable friction and slip rate coefficients.

Figure 6.6 – Temperature cross section at the center of the pin of Test 5 with different μ_f values
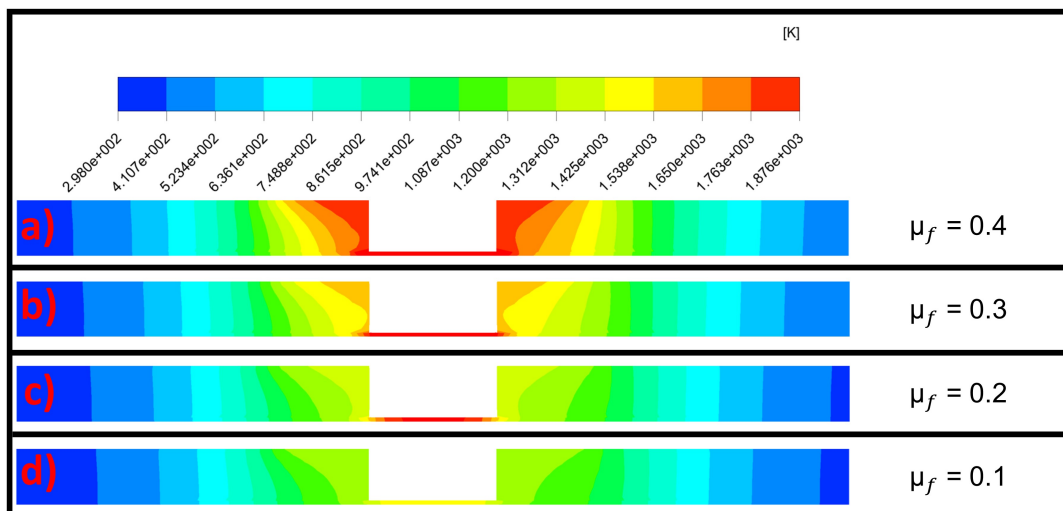
Source: The author

The high temperatures observed in Figures 6.5 and 6.6 are due to the contribution of different welding parameters and may be related to defects in the weld. Figure 6.5, with lower rotation, shows that when the axial force is increased from 35 to 50 kN (Tests 1 and 2), the temperature does not rise as much as was observed for the increase of rotation from 450 to 800 RPM (Tests 1 and 5). This indicates that rotation is the main parameter responsible for the generation of heat. In fact, from the Test 5 results, which was performed applying an axial force of 35 kN and a rotation of 800 rpm, the temperature distribution along the cross-section presented some regions that tended to reach extremely high temperatures (Figure 6.5e). This result corroborates with the experimental results for this condition that indicated an intense production of flashes and poor surface finish, as shown in Figure 6.7.

Figure 6.7 – Top (a) and Transverse (b) section for test 5 - 800 rpm, 1 mm/s and 35 kPa

Source: The author

The above results cannot possible mean that defects such as flashes will only occur when the temperature rises dramatically, as observed in the tests 5 through 7. For instance, for Test 2 that was welded with the highest axial force (50 kN) but using a lower rotation (450 RPM), such high temperatures were not found. Nonetheless, when tested experimentally, this condition showed an excessive flash formation (Figure 6.8). These previous results suggest that the combination of low viscosity and high pressure is also very detrimental, contributing to the formation of flashes. Therefore, there is an axial force limit at which the heated material, whose viscosity has decreased due to the contribution of heating, does not have enough strength to withstand the pressure applied by the tool, and therefore is expelled from the weld in the form of flashes.

Since these several tests performed with different welding parameters showed similar behavior concerning the formation of flashes and considering that the main parameters associated

Figure 6.8 – Transverse section for Test 2 - 450 rpm, 1 mm/s and 50 KPa

5000 µm
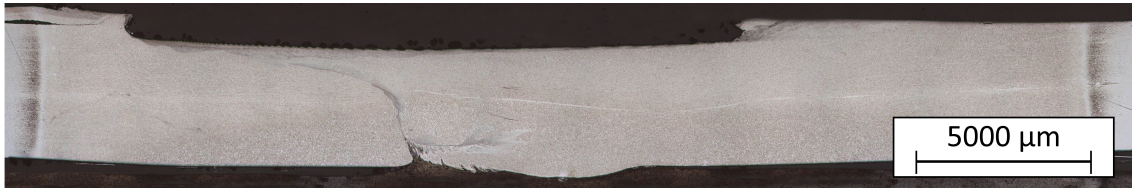
Source: The author

with these defects are pressure (axial force) and rotation speed, a new empirical parameter has been proposed. The Y parameter was developed to correlate the tendency to form flashes on FSW welds, considering the two main welding parameters responsible for the heating and stirring, as stated in Equation 6.20. According to this parameter, the higher the Y value, the greater the tendency to form flashes during welding.

$$Y = \frac{P}{\omega . \mu_{minimum}} \tag{6.20}$$

where P is the axial pressure calculated from the experimental tool area. Table 6.5 shows all the Y values for the tests performed.

Table 6.5 – Y values for all tests

Test	Y
1	87.07
2	213.91
3	26.27
4	47.68
5	223.08
6	193.81
7	190.13

Source: The author

There is a gradual increase in the Y parameter for the rotation and pressure change for Tests 3 (15 kN and 800 rpm), 4 (20 kN and 800 rpm) and 1 (35 kN and 450 rpm) . Therefore, there is a tendency to generate flash when the Y parameter increases. An example of this tendency can be observed in Figure 6.9. However, the Y parameter cannot predict other welding problems such as wormholes, as can be seen in Figure 6.9a for Test 3. The wormholes are discussed next.

Figure 6.9 – Macrography results. a) Test 3 with $Y = 26.27$, b) Test 4 with $Y = 47.68$, and c) Test 1 with $Y = 87.07$.
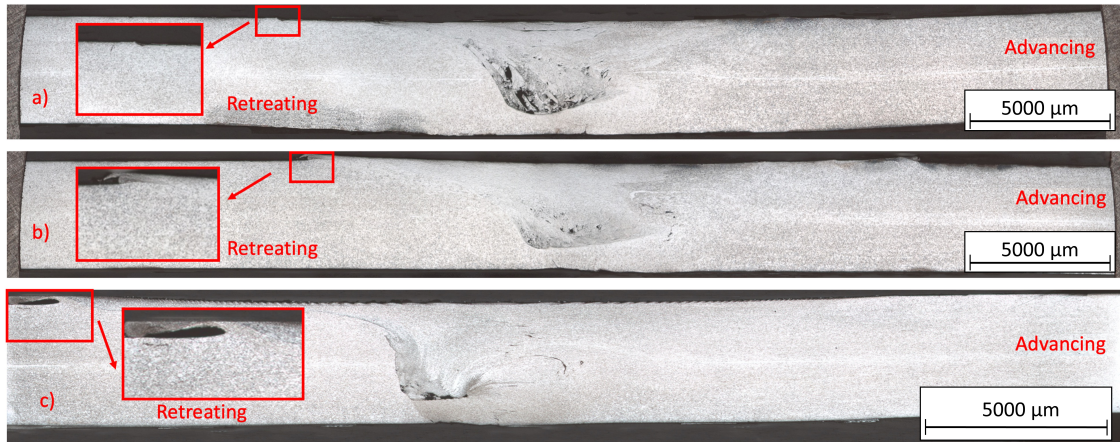
Source: The author

The wormholes were analyzed using a discrete phase simulation. Inert particles were injected into the fluid and their paths on the plate were recorded. The results of this investigation were plotted in terms of the density plane of the particles after they passed over the tool; we associated the density of the particles that crossed the plane with the tendency to form wormholes. Figure 6.10 shows a general path of particles in the material. In this and the following figures, "inlet plane" denotes the plane where particles enter the material and "outlet plane" denotes the plane after the tool, where it is possible to see the particle density. The using of discrete phases to predict wormholes was used by other authors to forecast the wormholes in other materials using FSW, see for example, Zhu *et al.* (2016) who used this approach to predict the formation of wormholes in an aluminum alloy.

Figure 6.10 – The route of the particle(s) in the material.
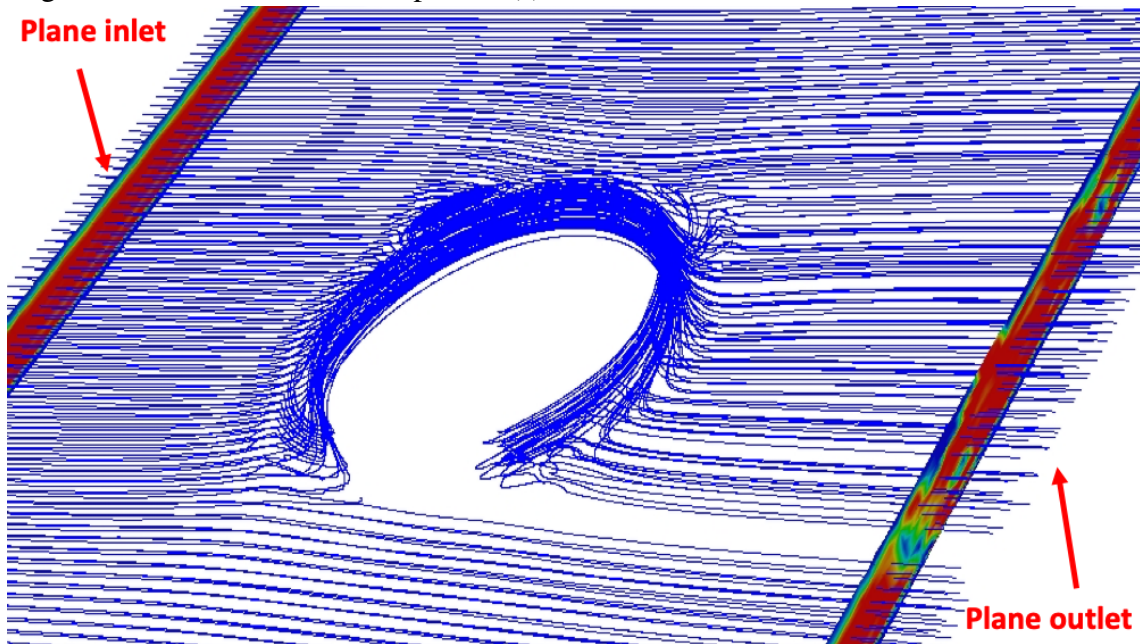
Source: The author

       The difference between the real tool geometry and simulated tool geometry changes the wormhole position. However, this change does not affect the prediction of wormhole formation. Figure 6.11 shows the cross section of Test 1. The experimental results confirmed that a small wormhole at the base of the pin existed, as highlighted in Figure 6.11a. The wormhole is predicted in the numerical result by the reduction of particle density as verified in Figure 6.11b. As mentioned before, there is a difference in the position of the experimental and numerical wormholes due to the difference in shape of the real and simulated tool. In Figure 6.11 this difference was evidenced by the red lines (Real format) and the black lines (Simplified format of the simulation).

Figure 6.11 – Concentration of Particles in the plane of Test 1.
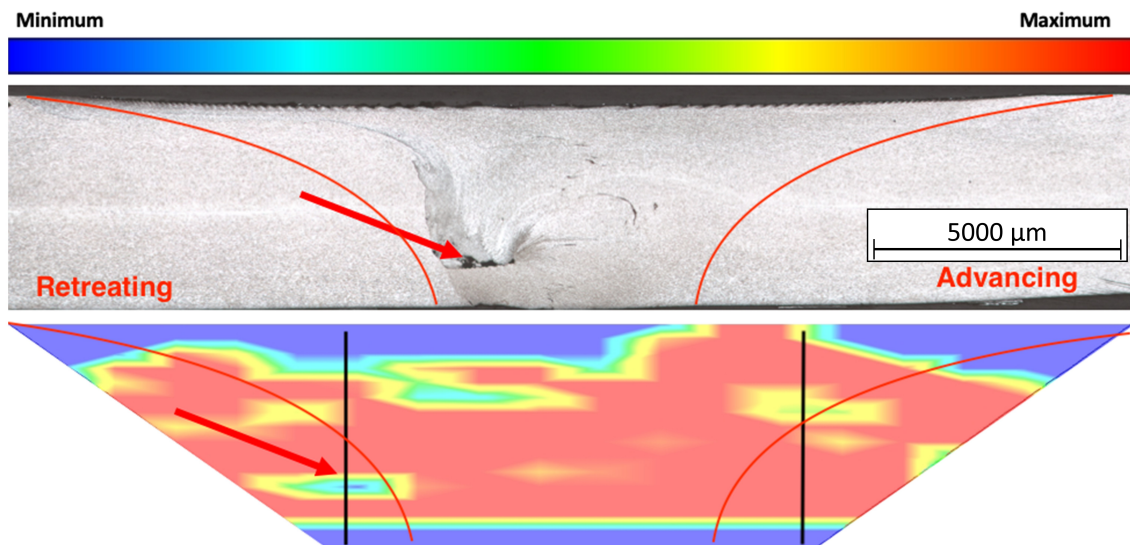
Figure 6.12 compares the differences among the Tests 5, 6, and 7, in which the welding speed is changed and other parameters are kept constant. Test 6 verifies that a small wormhole is formed in the simulation results (see Figure 6.12d), which is compatible with the experimental result that shows the wormhole in the highlighted region (see Figure 6.12c). Test 7 also shows the formation of wormholes in the same region as the simulation. However, the simulation indicated a large area of low particle density throughout the plane when compared with the simulated results of Test 6. This achievement is once again collaborated by the experimental result (Figure 6.12e) that presents a large wormhole in the same location. The experimental test 5 (Figure 6.12a) did not have any wormholes; however, the simulation has a lower particle density when compared to Tests 6 and 7. This occurred because this experimental test had other mechanisms of mass loss, such as the flashes previously analyzed.

Figure 6.12 – Experimental and simulated wormholes. a) Test 5 – experimental, b) Test 5 – numerical, c) Test 6 – experimental, d) Test 6 – numerical, e) Test 7 – experimental, and f) Test 7 – numerical.
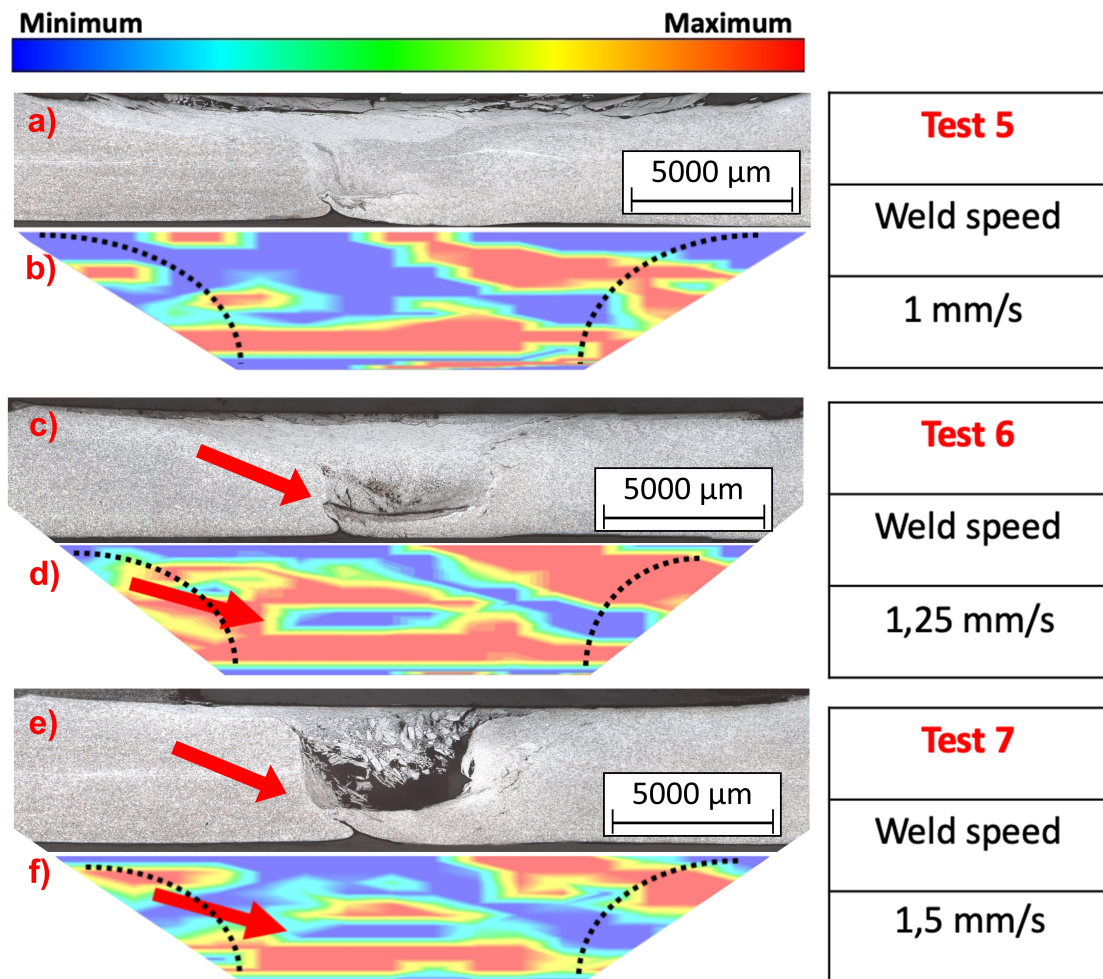
Source: The author

6.6 Conclusions

In this work, we performed a numerical investigation of FSW for the AISI 304L stainless steel using the commercial simulator ANSYS-Fluent. The numerical thermal cycles were in good agreement with the experimental thermal cycles of the test analyzed; the maximum difference observed between the experimental and numerical thermal cycles was about 50 K for the conditions simulated. We also investigated the effect of several parameters, such as, the axial force, the welding speed, and the rotation on the FSW process for the AISI 304L stainless steel. The numerical analyzes were able to predict two important defects commonly found in the FSW process: the flashes and the wormholes. In order to investigate the flashes, we proposed the use of parameter Y, which depends on the minimum viscosity, the axial force, and the deformation rate. We verified that the flashes increased when the parameter Y increased and

this was directly connected to the axial forces. In addition, the discrete phase simulation was an efficient technique to predict wormholes and the welding speed is one of the main factors in the formation of wormholes.

7 NUMERICAL INVESTIGATION OF THE INFLUENCE OF FRICTION STIR WELDING PARAMETERS ON THE MICROSTRUCTURE OF AISI 410S FERRITIC STAINLESS STEEL JOINTS

7.1 Review

This article analyzed the simulation of ferritic stainless steel in order to observe the temperatures reached and, consequently, observe the possible phases formed. The Zener-Hollomon parameter was calculated and compared with the literature in order to observe its relationship with the grain size.

7.2 Introduction

Stainless steels are widely used in manufacturing industries for items such as refrigerators, washing machines, cookwares, and automotive exhaust systems, among others. Ferritic stainless steels are a class of stainless steel that have corrosion resistance superior to carbon steels and close to that of austenitic stainless steels. However, the former stainless steels are cheaper than the austenitic because they do not have nickel in their chemical composition (AMUDA *et al.*, 2016; HU *et al.*, 2007). When mechanical strength is of lesser importance, ferritic steels are an excellent choice to replace the expensive austenitic steels. Other advantages besides the cost of ferritic stainless steels over austenitic stainless steels are the high thermal conductivity, the low thermal expansion, and the lower susceptibility to pitting and stress corrosion cracking (LIPPOLD; KOTECKI, 2005; ANTUNES *et al.*, 2013).

The use of ferritic stainless steels has grown in recent decades, including for industrial equipment and components for transportation (automobiles, railways and subways), food and breweries, alcohol and sugar, chemical processing, as well as the petroleum and gas industries (SANTACREU *et al.*, 2011; SILVA *et al.*, 2008b; TOIT *et al.*, 2007; SILVA *et al.*, 2008a; KNUTSEN; BALL, 1991). However, to consolidate this growth, there must be a continuous improvement in the manufacturing process to increase the performance of these steels when applied to different types of equipment and subjected to different environments. Additionally, welding, which is currently one of the leading manufacturing processes used to construct and repair these steels (LAKSHMINARAYANAN *et al.*, 2009), must be taken into consideration.

There are several studies in the literature that have evaluated the effect of welding processes on the welded joint in terms of the microstructure, mechanical properties, and corrosion

resistance (TABAN *et al.*, 2009; LAKSHMINARAYANAN *et al.*, 2009; SILVA *et al.*, 2008b; WARMELO *et al.*, 2007). Fusion welding can cause unwanted metallurgical transformations that are harmful to various applications of ferritic stainless steels. Sundqvist *et al.* (2018) showed, for example, that welding thermal cycles in low chromium ferritic stainless steels can increase the hardness by martensite formation, which in turn can cause the region around the weld to become brittle. Controversially, Deleu *et al.* (2009) pointed out that in some ferritic steels, a small amount of martensite has a beneficial effect on the toughness at low temperatures. The authors stated that a ferrite/martensite balance associated with the control of the carbon content helps to improve the mechanical strength and toughness of these materials.

Another problem that affects the weldability of ferritic stainless steels is the intense grain growth in the fusion zone and in the heat affected zone (SILVA *et al.*, 2008b), which impairs ductility, toughness, and fatigue resistance(LAKSHMINARAYANAN *et al.*, 2009; SHANMUGAM *et al.*, 2009). The welding procedures recommend the use of austenitic stainless steel consumables to overcome the unwanted grain growth in the fusion zone (SILVA *et al.*, 2013; AGUILAR *et al.*, 2013; LAKSHMINARAYANAN *et al.*, 2009). Recently, studies have developed metal-cored welding wires that provide refined microstructure and good mechanical properties for fully ferritic stainless steel welds (VILLARET *et al.*, 2013). Another possibility is the choice of an appropriate welding process combined with a low heat input (BALASUBRA-MANIAN *et al.*, 2008). However, this problem will persist in the heat affected zone (HAZ) for various different ferritic steels and various applications.

A third welding problem that has been reported in the literature for these steels is the risk of sensitization caused by the precipitation of chromium carbides ($Cr_{23}C_6$) along the grain boundaries (SILVA *et al.*, 2008b; NIEKERK *et al.*, 2012). This phenomenon is activated by the thermal welding cycle when, during heating and cooling, the steel is exposed to a critical temperature range. Even when this exposure is only for a short time, it is sufficient to provide the necessary thermodynamic conditions to nuclear and grow the $Cr_{23}C_6$ carbides(MEYER; TOIT, 2008). Intergranular precipitation of the $Cr_{23}C_6$ carbides results in a chromium depletion zone in the matrix that surrounds the grain boundaries (BOND; LIZLOVS, 1969; DEVINE; RITTER, 1983; KIM *et al.*, 2009) and significantly impairs the corrosion resistance (KIM *et al.*, 2009; LAKSHMINARAYANAN; BALASUBRAMANIAN, 2012).

Many of these problems are related to the high temperatures reached using conventional welding processes; that is the temperature where the melting point of the welding

material is reached. In order to overcome the former problems during the welding processes, in 1991, The Welding Institute (TWI) developed a new solid-state joining method named Friction Stir Welding (FSW)(THOMAS *et al.*, 1991). FSW provides a lower peak temperature, where the welding occurs close to 80% of the melting point of the materials, thus allowing the metal to be joined without reaching the liquid state (TANG *et al.*, 1998). FSW is performed by a non-consumable rotating tool that penetrates and moves between the interfaces of the materials to be welded (MISHRA; MA, 2005). The tool is made up of a wide section called the shoulder and an elongated part called the pin. The design of the tool is an essential variable of the process since it influences the heat generation, material flow, and other features introduced into the welded joint(NANDAN *et al.*, 2008a). The heat is promoted by friction between the tool and workpiece. As a consequence of the increase in temperature, the viscosity of the material is reduced, making the material softer and allowing it to flow around the pin. It is precisely this material flow that enables the continuous filling of the cavity formed by the penetration of the pin against the parts, as the tool moves in the welding direction. Figure 7.1 shows a schematic of the process. where it is possible to see the region in which the tool penetrates the workpiece, which is a region of intense plastic deformation.

Figure 7.1 – Schematic illustration of the FSW process
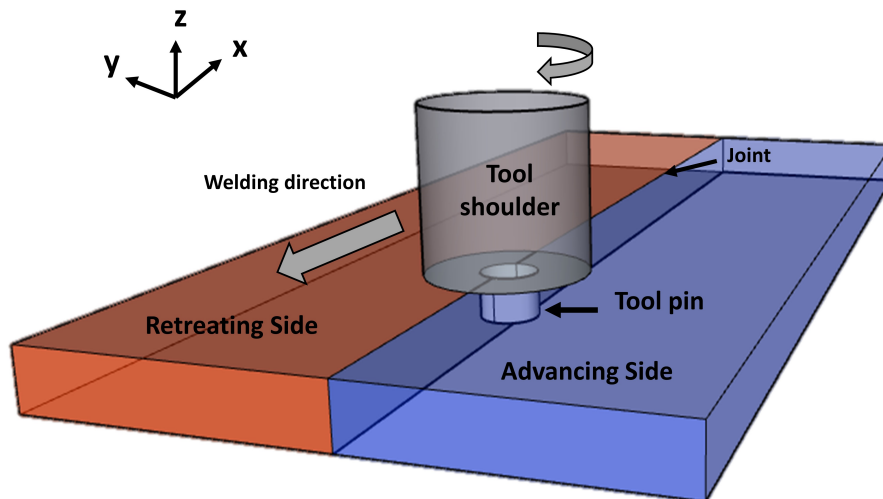
Source: The author

Besides the material flow due to the movement of the tool, the combination of temperature and strain rate imposed during the FSW welding can also cause an increase in the dislocation density and, consequently, dynamic recrystallization (DRX) (ROLLETT *et al.*, 2004). This phenomenon is responsible for a remarkable decrease in the grain size, which is a desirable feature of the FWS process. Welds that undergo DRX enhance their mechanical properties and

toughness significantly (DEHGHAN-MANSHADI; HODGSON, 2008).

Dynamic recrystallization in FSW was studied by Emami e Saeid (2019) using different stainless steels. They analyzed the microstructural changes of the following materials after welding 304 austenitic, 430 ferritic, and SAF 2205 duplex stainless steels using the FSW process. They verified that the grain refining in different regions of the weld was Due to the peak temperature and deformation reached in the welded joint.

As observed in several works , the FSW process can cause changes in the material microstructure. Understanding and predicting the mechanisms presented and how the main FSW parameters affect the microstructure is of great importance for good quality welds and also reduces the number of experiments needed. The main goal of this work is to analyze the possible structural changes in the material and to provide the factors that most influence the quality of welds when using the FSW process, such as temperature, strain rate, and changes in the viscosity of the material.

A partnership between the Solid State Joining Processes group at the Helmholtz-Zentrum Geesthacht (HZG) in Germany and the Welding Research and Technology Laboratory group at UFC in Brazil started an international scientific and technological cooperation on the welding of stainless steels with FSW processes. This joint research has focused on the development of experimental studies in FSW using the above aforementioned steels, especially the ferritic stainless steels due to the importance of these alloys and restrictions of their applications imposed by the welding metallurgy (ANDRADE *et al.*, 2015; CAETANO, 2012). As a complete investigation of all parameters that affect the quality of FSW welds using only experimental investigation is expensive and time consuming, we also applied simulation tools to understand and predict the dynamic recrystallization and the influence of welding parameters on the ferritic stainless steel joints using FSW.

The advantages found during the experimental evaluation motivated the use of simulation tools to understand the effect of the welding parameters on phase transformation and other microstructural related features . This study aims to simulate the FSW processes to predict and assist the experimental results. Also simulations can predict dynamic recrystallization and the influence of the welding parameters on the results.

7.3   Materials and Experimental

In this study, six different welding conditions were simulated to understand how the axial force and the rotational velocity affect the final welded material. The welding conditions are presented in Table 7.1. A constant weld speed equal to 1 mm/s was used for all investigations. The combinations of parameters used were selected from a previous study performed by Caetano (2016).

Table 7.1 – Experimental parameters used

	Axial Force(kN)	Rotational Speed(rpm)
Test 1	10	450
Test 2	15	450
Test 3	20	450
Test 4	22	800
Test 5	25	800
Test 6	30	800

Source: The author

All welds were performed using AISI 410S ferritic stainless steel plates of 200x500x4 mm and the samples were joined along the 500 mm side at the Helmholtz Zentrum Geesthacht (HZG) Center, Germany. The welds were performed using a PCBN (Polycrystalline Boron Nitride) tool as shown in Figure 7.2 and argon was the shielding gas. Six thermocouples were installed on the top surface, three on either side (advanced side and retraction side) of the welding centerline at 15, 20, and 25 mm from it for Test 1.

Figure 7.2 – PCBN tool geometry with scale in millimeters and inches
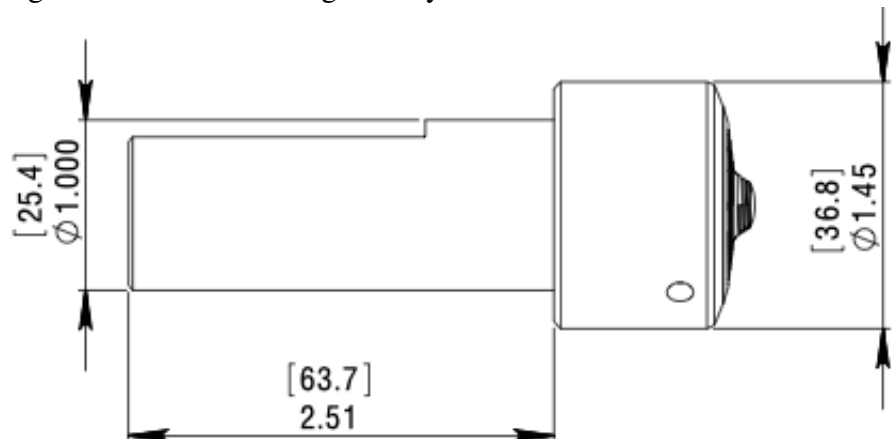
Source: The author

The chemical composition of the AISI 410S ferritic stainless steel used in this investigation is given in Table 7.2, and the thermal properties of the tool and steel are shown in Tables 8.3, and 7.4, respectively.

Table 7.2 – Chemical composition of the AISI 410S stainless steel(% mass)

Material	Fe	C	Cr	Mn	Ni	P	Si	S	Mo
410S	Bal	0.025	12.8	0.3	0.21	0.023	0.37	<0.010	0.014

Source: The author

Table 7.3 – Thermal proprieties of the AISI 410S stainless steel

Temperature (K)	Density (Kg m^3)	Specific heat capacity (J kg^{-1} K^{-1})	Thermal conductivity (J kg^{-1} K^{-1})
298	7800	-	-
373	7794	473	27.6
473	7786	515	27.6
673	7768	607	26.4
873	7749	-	25.1
1073	7730	691	-
1273	7712	-	21.8

Source: Cho *et al.* (2013)

Table 7.4 – Thermal proprieties of the material of the tool

Material	Density (kg/m^3)	Thermal Conductivity ($W/m \cdot K$)	Specific Heat ($J/kg \cdot K$)
PCBN	3450	120	750

Source: Almoussawi e Smith (2018)

7.4 Physical model

All simulations performed in this study are related to the steady-state regime. The start and end of the weld beads do not acquire a steady-state regime and therefore were not considered in this study. The intermediate section, considered in this work, was assumed to be heated under steady heat generation. We also assumed similar properties, geometry, and structure for the cross-section of the weld. According to Song *et al.* (2014), the similarities mentioned above are enough to warranty the steady-state regime. In addition to the previous assumptions, the shoulder was considered to be in contact with the top surface of the workpiece as shown in Figure 8.1. During the welding, the pin is forced deep enough into the workpiece to stir the workpiece fully. However, in order to avoid the workpiece being welded to the backing bar, a gap of 0.3 mm was maintained between the tip of the pin and the base of the plate. Pressure, rotation, and shear stress ($\tau = \sigma_{yield}/\sqrt{3}$), where σ_{yield} is evaluated using the distortion energy theory for the plane stress) at the contact between the pin and the workpiece were kept constant during the welding process.

Figure 7.3 – Schematic diagram used in the FSW simulation. a) velocity boundary conditions and b) top view of the tool.
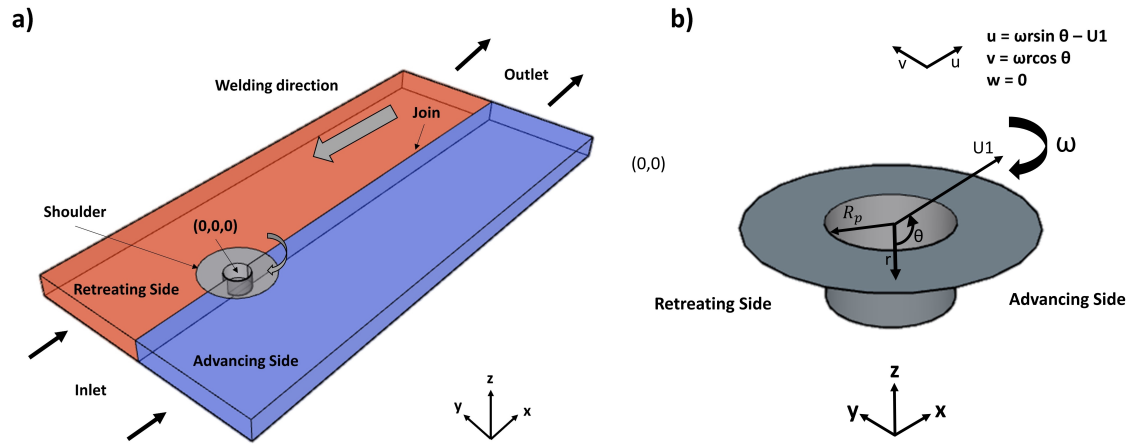
Source: The author

7.4.1 Governing Equations

The workpiece was assumed to be a non-Newtonian, incompressible, and viscoplastic fluid. We also considered a partial sticking condition between the tool and the workpiece and the tilt angle of the tool was set equal to zero (NANDAN *et al.*, 2006a). The reference coordinates were fixed at the center of the tool and the top of the workpiece. The continuity equation is given by

$$\frac{\partial u_i}{\partial x_i} = 0 \; ; i = 1, ..., 3 \tag{7.1}$$

where u_i is the velocity of the plastic flow at the x-(1), y-(2), and z-(3) coordinates. Equation 8.2 states that the volume variation is null. The momentum conservation equation for the coordinate system attached to the tool using an indicial notation is given in Cho *et al.* (2013) as

$$\frac{\partial \rho u_j}{\partial t} + \frac{\partial \rho u_i u_j}{\partial x_i} = -\frac{\partial P}{\partial x_j} + \frac{\partial}{\partial x_i}\left(\mu \frac{\partial u_j}{\partial x_i}\right) - \rho U \frac{\partial u_j}{\partial x_1} \tag{7.2}$$

where U is the weld velocity, ρ is the density of the workpiece, P is the pressure, and μ is the non-Newtonian viscosity of the welded material. The viscosity model for the AISI 410S stainless steel is described in a later section. The conservation energy equation is given by

$$\frac{\partial(\rho C_P T)}{\partial t} + \frac{\partial(\rho C_P u_i T)}{\partial x_i} = -\rho C_P U_1 \frac{\partial T}{\partial x_1} + \frac{\partial}{\partial x_i}\left(k \frac{\partial T}{\partial x_i}\right) + S_i + S_b \tag{7.3}$$

Although our goal is to find the steady-state regime, the transient term was kept in Eqs. (8.3) and (8.4) because the commercial simulator FLUENT from Ansys uses a distorted transient to reach the steady-state solution. In Equation (8.4), C_P is the specific heat and k is the thermal conductivity, S_i is a source term that denotes the rate of energy per unit of volume dissipated by friction between the tool and the workpiece, and S_b denotes the rate of energy per unit of volume generated by plastic deformation in the workpiece away from the interface.

7.4.2 Boundary conditions and heat source

The heat source, S_i, was added to the FLUENT commercial software by means of UDF (User-Definition Function) as a heat flux. Therefore, the S_i is defined by

$$S_i = q_1 \frac{A_r}{V} \tag{7.4}$$

where A_r is the contact between the tool and workpiece and V is the volume surrounding A_r. $q_1 [W/m^2]$ is the heat flux generated by the contact of the shoulder tool and the workpiece, which is evaluated by

$$q_1 = \left[\delta n \tau + (1 - \delta) \mu_f P \right] (\omega r - U_1 \sin \theta) \tag{7.5}$$

In the above equation, P is the pressure of the tool during the welding, ω is the angular velocity, U_1 is the welding speed, η is the thermal efficient, $\tau = \sigma_{yield}/3$ (where σ_{yield} is evaluated using the distortion energy theory for the plane stress), and μ_f is a friction coefficient. The term $(\omega r - U_1 sin\theta)$ represents the relative velocity between the tool and workpiece, where the parameters involved are defined by

$$\sin \theta = \frac{y}{r} \tag{7.6}$$

$$\cos \theta = -\frac{x}{r} \tag{7.7}$$

$$r = \sqrt{x^2 + y^2} \tag{7.8}$$

where r is the radius with the global axis fixed at the center of the tool.

The source term per unit volume, generated by plastic deformation (S_b), is defined in Fluent as the heat generation rate in the boundary condition section by UDF. This source term is calculated as $f_m \mu \Phi$, where μ is the viscosity, f_m is an arbitrary constant that indicates the extent of atomic mixing in the system. In this study, a value of 0.04 was used for f_m and the viscous dissipation function Φ (CHO *et al.*, 2013) is given by

$$
\Phi = 2 \left(\left(\frac{\partial u_1}{\partial x_1} \right)^2 + \left(\frac{\partial u_2}{\partial x_2} \right)^2 + \left(\frac{\partial u_3}{\partial x_3} \right)^2 \right) + \left(\frac{\partial u_1}{\partial x_2} + \frac{\partial u_2}{\partial x_1} \right)^2 \\
+ \left(\frac{\partial u_1}{\partial x_3} + \frac{\partial u_3}{\partial x_1} \right)^2 + \left(\frac{\partial u_3}{\partial x_2} + \frac{\partial u_2}{\partial x_3} \right)^2
\tag{7.9}
$$

The heat generated by the contact of the tool and workpiece ($S_i + S_b$) is split between the workpiece and the tool. The fraction that is inputted into the workpiece (f) is defined by (NANDAN *et al.*, 2008b)

$$
f = \frac{J_w}{J_t + J_w}
\tag{7.10}
$$

where J_w(workpiece) and J_t(tool) are defined by the following equation:

$$
J_i = \sqrt{(\rho C_p k)_i} \; ; i = w \text{ or } t
\tag{7.11}
$$

In Eq. (8.12), $i = w$ or t for the workpiece and tool, respectively.

Convection and radiation were considered for the top of the plate, while only convection was considered for the bottom and sides. The boundary conditions described are, respectively, defined by the following equations:

$$
-k\frac{\partial T}{\partial y} = h_t (T - T_e) + \sigma \varepsilon (T^4 - T_a^4)
\tag{7.12}
$$

$$
k\frac{\partial T}{\partial z} = h_b (T - T_e)
\tag{7.13}
$$

$$
\pm k\frac{\partial T}{\partial y} = h_s (T - T_e)
\tag{7.14}
$$

where h_b, h_s, and h_t are the convective heat transfer coefficient for bottom, sides, and top of the workpiece, respectively, T_a is the environment temperature, k is thermal conductivity, σ is the Stefan-Boltzmann constant, and ε is the emissivity of the workpiece.

The velocities in the contact region between tool and workpiece were set in the boundary conditions. For the shoulder, the velocity components are given by

$$u = (1 - \delta)(\omega r \sin\theta - U_1) \tag{7.15}$$

$$v = (1 - \delta)(\omega r \cos\theta) \tag{7.16}$$

For the contact between the tool pin and workpiece, the velocity components are defined by

$$u = (1 - \delta)(\omega R_p \sin\theta - U_1) \tag{7.17}$$

$$v = (1 - \delta)(\omega R_p \cos\theta) \tag{7.18}$$

where R_p is the radius of the pin. All velocity components were implemented in the Fluent simulator using the UDF. All experimental parameters such as size of the workpiece, thermal conductivity, and welding speed are presented in Appendix C.

7.4.3   AISI 410S stainless steel flow stress

The viscosity model used for the simulation of the AISI 410S stainless steel was based on the formulation of the flow stress (σ_e) proposed by Sheppard e Wright (1979), where the flow stress is a function of the effective strain rate ($\dot{\varepsilon}$) and temperature (T), which is given by

$$\sigma_e = \frac{1}{\alpha} \sinh^{-1}\left[\left(\frac{Z}{A}\right)^{\frac{1}{n}} \right] \tag{7.19}$$

where α, A, and n are the constants of the materials and Z is the Zener–Hollomon parameter that is a function of temperature and the effective strain rate, and is given by

$$Z = \dot{\varepsilon} \exp\left(\frac{Q}{RT}\right) \tag{7.20}$$

where Q is the temperature-independent activation energy and the $\dot{\varepsilon}$ effective strain rate, which with the assumption of infinitesimal deformation is given by

$$\dot{\varepsilon} = \left(\frac{1}{2} \dot{\varepsilon}_{ij} \dot{\varepsilon}_{ji} \right)^{\frac{1}{2}} \tag{7.21}$$

$$\dot{\varepsilon}_{ij} = \frac{1}{2} \left(\frac{\partial u_i}{\partial x_j} + \frac{\partial u_j}{\partial x_i} \right) \tag{7.22}$$

The above equations were incorporated into the FLUENT Software using a User-Definition Function (UDF). However, as the UDF does not have the function $\sinh^{-1}$, Eq. (8.19) was replaced by

$$\sinh^{-1} \left[\left(\frac{Z}{A} \right)^{\frac{1}{n}} \right] = \ln \left\{ \left(\frac{Z}{A} \right)^{\frac{1}{n}} + \sqrt{ \left[\left(\frac{Z}{A} \right)^{\frac{2}{n}} + 1 \right] } \right\} \tag{7.23}$$

Figure 8.3 shows the viscosity profiles using the model described above for the AISI 410S stainless steel. The maximum value of viscosity in this study was approximately 10^7 Pa.s, which was defined by the methodology presented in the study carried out by Silva *et al.* (2020c).

Figure 7.4 – Profiles of the logarithm with base 10 of the viscosity function of temperature and strain rate
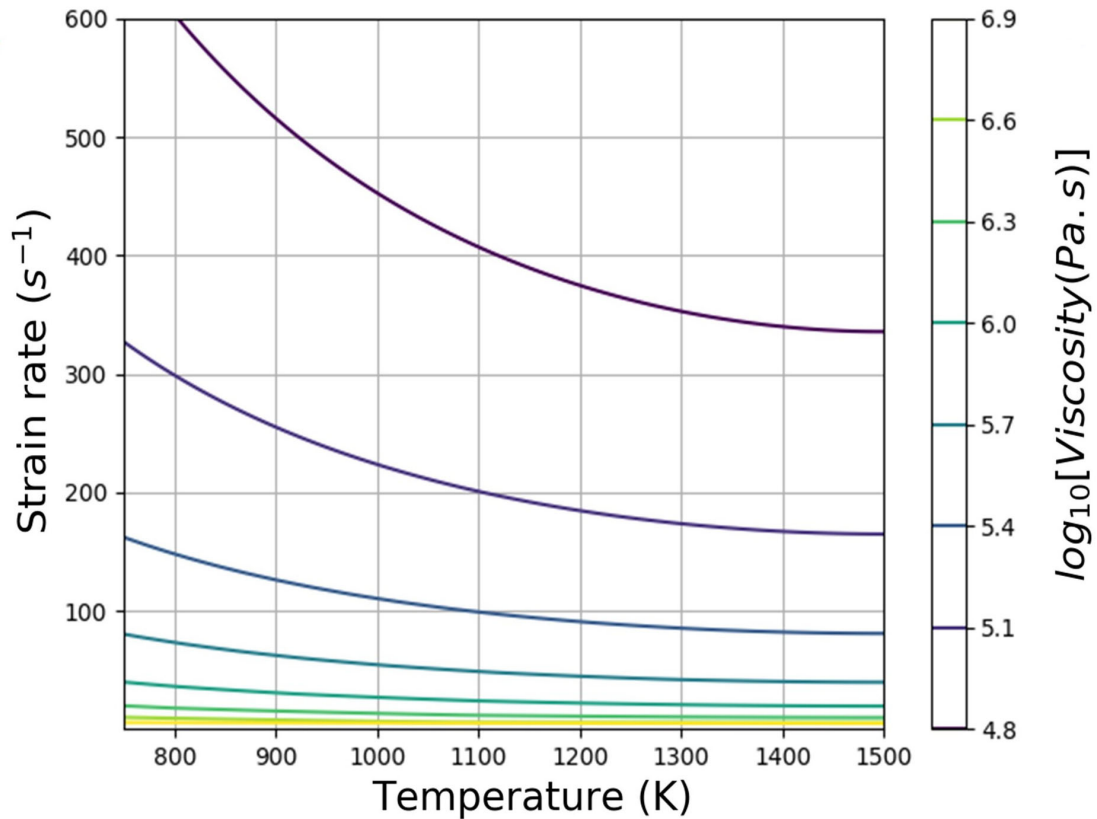
Source: The author

7.5 Results

The Ansys Fluent was used to solve Eqs. (8.2) through (8.4) along with the boundary conditions described above. A non-uniform grid shown in Figure 8.4, composed of only hexahedrons (1,227,002 elements and 1,296,068 nodes) was generated using the ICEM Mesh Software; this mesh was used for all simulations. From tests using several meshes than the one presented in Figure 8.4, we found that the aforementioned mesh was refined enough to produce mesh independent results.

Figure 7.5 – Hexahedron mesh used for all simulations.
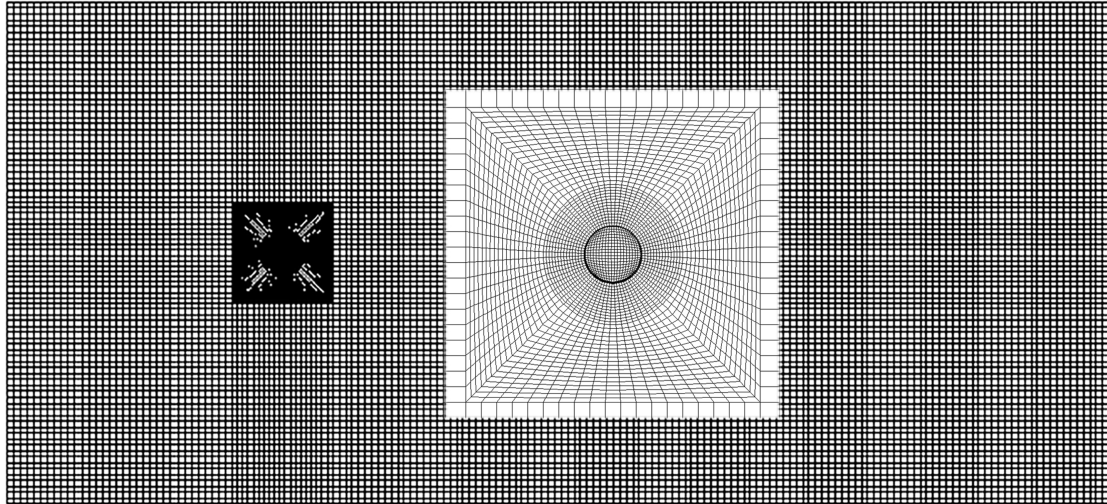
Source: The author

The simulation results in terms of the welding cycles were compared with the experimental results obtained by Caetano *et al.* (2019). The thermal cycles on the advancing and retreating side of the tool are shown in Figure 8.6. The difference between the experimental and simulated profiles occurred mainly at the maximum temperature peak on the retreating side and at the final stage of the cooling curve for both sides of the pin. However, these minor differences are less than 50 K and can be justified by minor variations in the positions of the thermocouples and small displacements caused by the welding process itself. Although the results presented in Figure 8.6 refer to Test 3 (see Table 7.1), the other tests shown in Table 7.1 had similar behaviors.

Figure 7.6 – Comparison between experimental and simulated results of Test 3
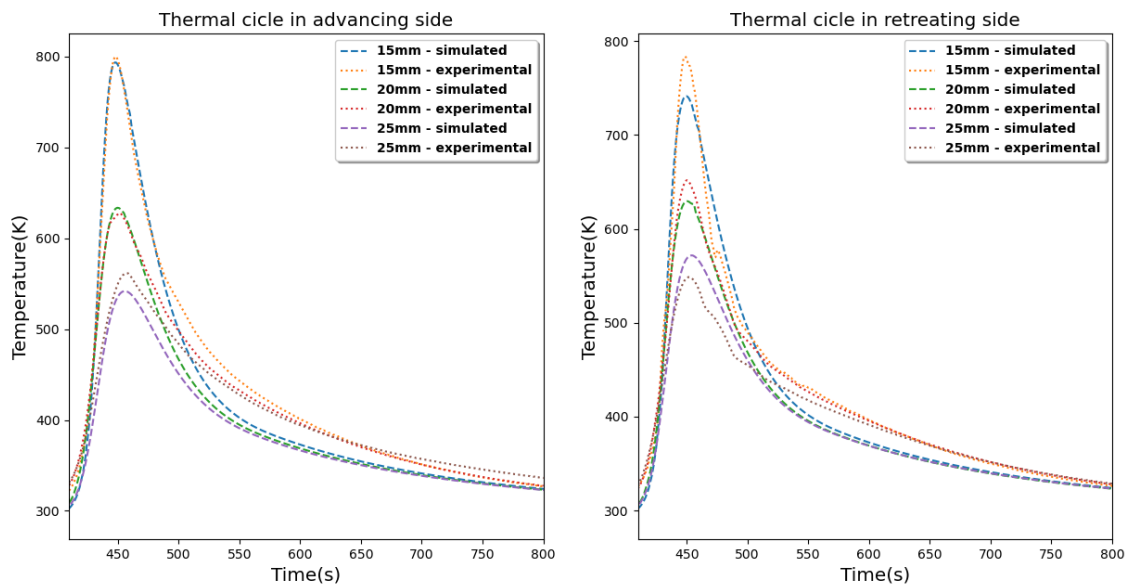
Source: The author

After validating the numerical results in terms of welding cycles with the available experimental results, the temperature field for the conditions of Table 7.1 was investigated. Figure 7.7 shows the temperature field at the top of the workpiece. Also, four more conditions designed to increase the range of force at each investigated rotation were included in this Figure.

The heating does not propagate very far in front of the tool, as the material is initially cold. However, behind the tool the temperature profile is much more elongated due to heat convection and (due to) the passage of the rotating tool (that caused the material to heat up). Such behavior was observed for all tests analyzed in this study.

Although in FSW the maximum temperature expected is close to 85% of the melting point, values beyond this point were found for some conditions presented in Figure 7.7 (see e, g, h, j). These extremely high temperatures occurred due to the limitation of the model and also to the friction coefficient that does not decrease sufficiently for extreme conditions. In a previous study, we analyzed the effect of the friction coefficient on the maximum temperature; we found that under extreme conditions, the friction coefficient decreased and this effect needs to be consider in the model (SILVA *et al.*, 2020c).

The temperature behavior of the material under FSW lap was discussed by Hattel *et al.* (2009), where the authors comment that due to the slip and stick effect when the material is close to solidus temperature the yield stress is drastically reduced, developing fluid characteristics at the tool/matrix interface. This reduction in material resistance decreases δ and τ parameters of the equation 7.5 to values close to zero and, consequently, the friction coefficient will also be reduced to values close to zero, resulting in a low thermal input at high temperatures. This behavior has been pointed out as a strong contribution to avoid the melting of the steel.

Figure 7.7 – Temperature contour of the top. a) 450 rpm-10 kN, b) 450
rpm-15 kN, c) 450 rpm-25 kN, d) 450 rpm-30 kN e) 800
rpm-10 kN, f) 800 rpm-15 kN g) 800 rpm-22kN h) 800
rpm-25 kN i) 800 rpm-30 kN
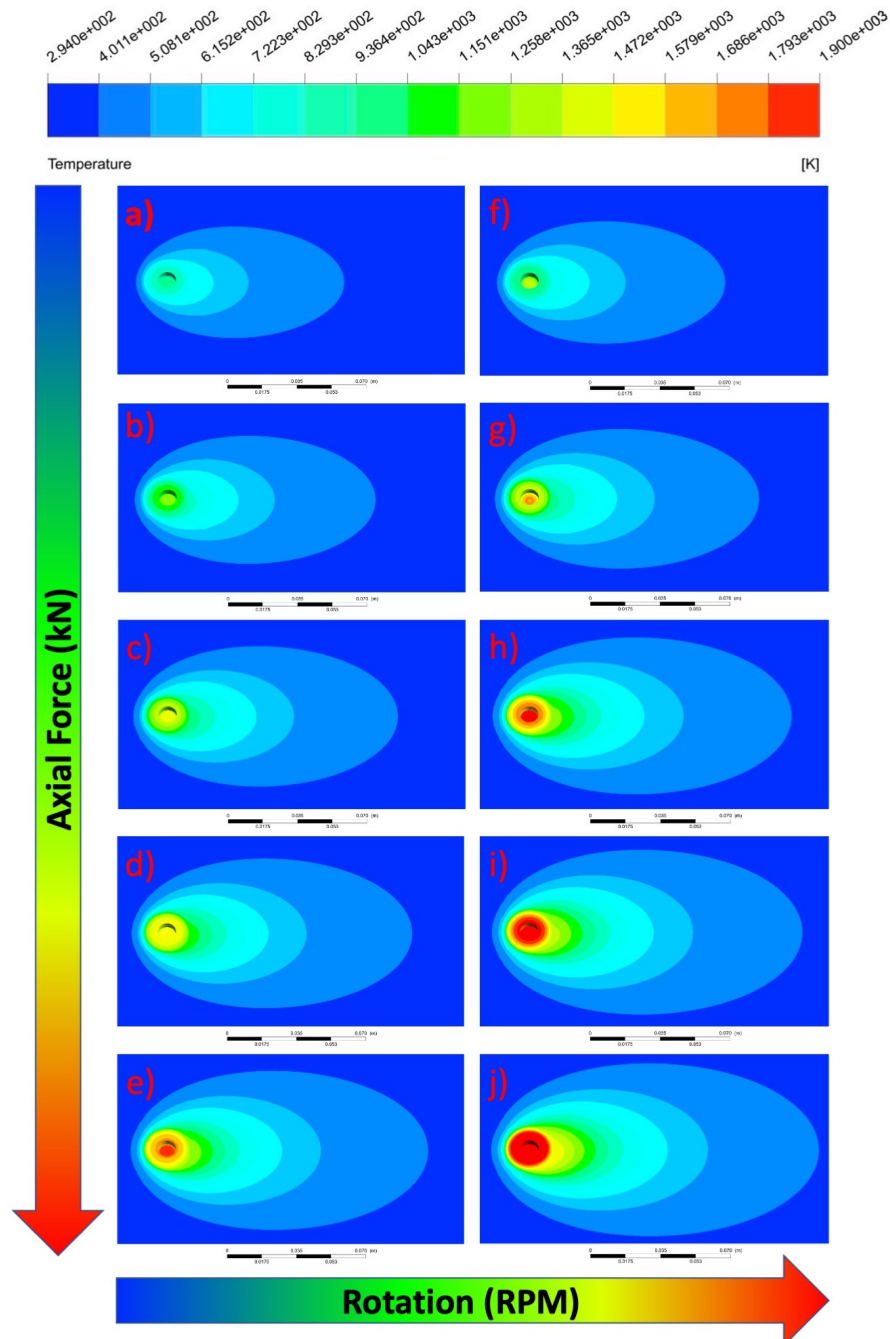
Source: The author

Figure 7.8 shows the macrography, viscosity, velocity, and the temperature of the
weld along the cross-section in the central region of the tool for Test 3. This figure clearly shows
the velocity gradient between the pin wall and the rest of the plate. Temperature and deformation
rate modify the viscosity of the material and a less viscous material is directly associated with

the stir zone of the material. The green line in Figure 7.8a represents the stir zone determined experimentally. The scale of the numerical results presented in Figures 7.8b, 7.8c, and 7.8d is the same scale shown in Figure 7.8a. The red line outlines the transition between the light blue and dark blue regions, where the minimum viscosity starts to increase. In Test 3, which was chosen due to the absence of welding defects, the stir zone represents the region with the lowest viscosity in Figure 7.8b. The simulation presented an excellent forecast of the stir zone, showing a divergence only at the base of the pin, as shown in Figure 7.8a by the green line. This difference can be caused by the simplified shape of the tool used to simulate the weld.

Compared to the other properties of Figure 7.8, the temperature field presented a variation over a large region. Considering the red line as the reference to delimit the stir zone, the thermomechanically affected zone (TMAZ) can be classified as the transition region between the stir zone and the thermally affected zone, which is a region that only suffers thermal effects. In Figure 7.8-b, there is a transition region between the low and high viscosities (light blue and yellow regions) that represent the TMAZ, because there is a low velocity (Figure 7.8-c) and a low viscosity, which represents a region that was affected by heat and deformation.

Figure 7.8 – Weld cross-section on the tool region of Test 3: a) Macrography; b) viscosity;
c) velocity; d) temperature field.
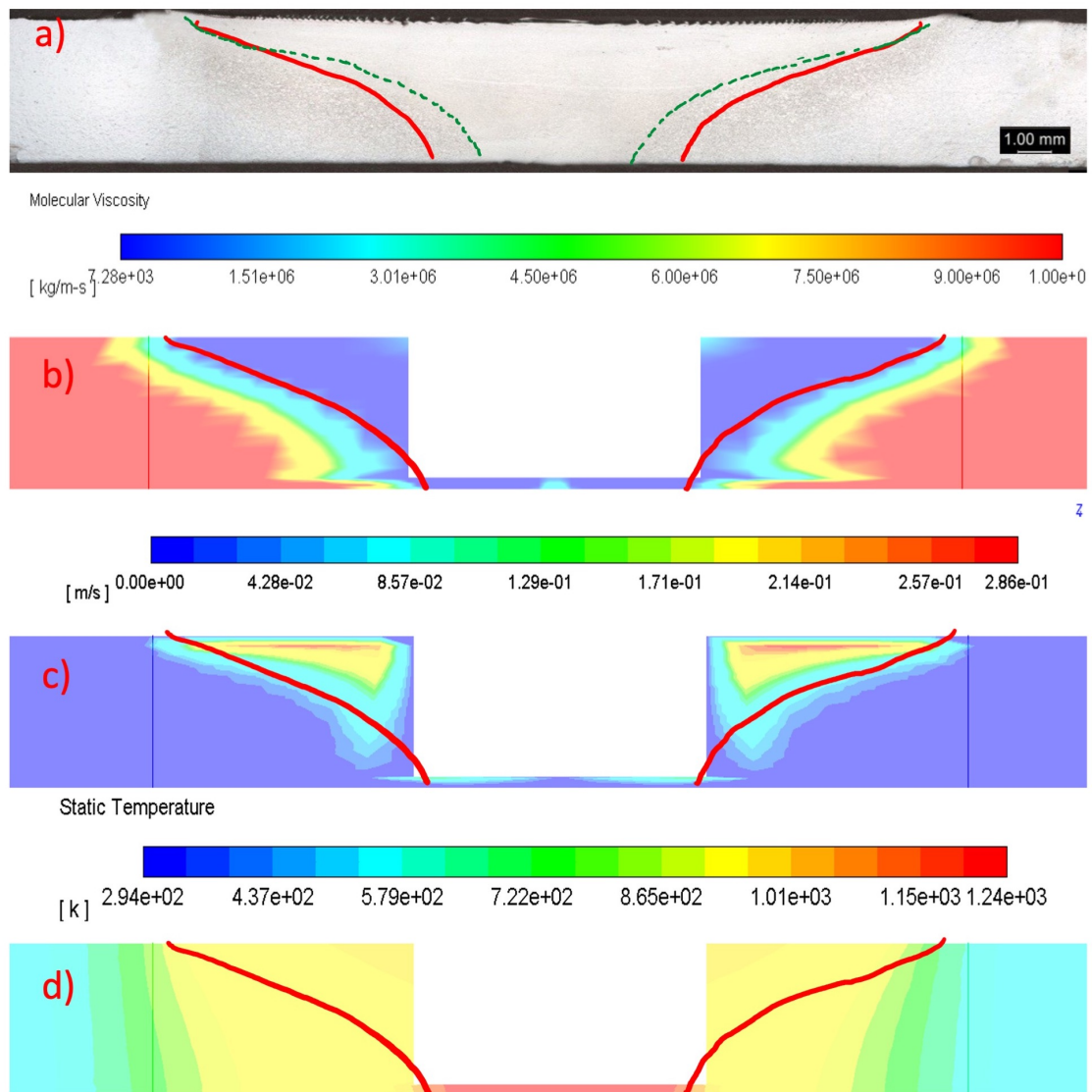
Source: The author

Phase transformations are of great importance in welding, due to their intrinsic relationship with mechanical properties and corrosion resistance. Therefore, the thermodynamic simulation provides useful information to identify the temperature peaks reached in specific regions, and the temperature profile over time. This information can be associated with diagrams of phase equilibrium transformation and experimental evaluations conducted by microscopic analysis to verify the correlation between the micro-structural changes during the welding process. Figure 7.9a shows the temperature field as well as the micrographic results along the cross-section of the weld for Test 3 and Figure 7.9b and c show the Thermo-Calc analysis for the AISI 410S stainless steel. Figure 7.9b shows that when the temperature is approximately 1073 K the transformation of ferrite into austenite starts, and when the temperature is approximately

1173 K, only austenite is present. Carbides ($Cr_{23}C_6$) can also be formed at temperatures below 1173 K; as highlighted in Figure 9c. The analysis of carbides is a critical issue because it can be, in some instances, the leading source of corrosion for these materials. Caetano *et al.* (2019) studied the micro-structure and susceptibility to corrosion in AISI 410S stainless steels. These authors concluded that when rotation is increased, the material becomes more susceptible to intergranular corrosion, due to the precipitation of chromium carbides.

The micro-structural results in Figure 7.9 for the $(1)\alpha + \gamma$ microstructure, which is the region with the highest temperature, show that the light and dark regions becomed ferrite and martensite, respectively, when the material was cooled. When the temperature is above 1462 K, the Thermo-Calc(ANDERSSON *et al.*, 2002) analysis predicts a two phase region composed of ferrite and austenite with almost the same phase fraction. When the material is cooled at a high rate, the ferrite is maintained but the austenite can be transformed into martensite. Another important aspect in this region is that the grain size is larger than the one in the $(2)\gamma/(\alpha + \gamma)$ microstructure region. These extremely high temperatures cause intense grain growth and the dynamic recrystallization is not enough to fully refine . This growth is very harmful in conventional welding, which unlike FSW does not have a high deformation rate and consequently the grain grows even more.

The Thermo-Calc simulation of the $(2)\gamma/(\alpha + \gamma)$ microstructure region in Figure 7.9, which is between 1163 K and 1353 K, shows 100% of austenite and as a consequence the final microstructure after a rapid cooling is mostly martensite. Although the micro-structure is almost entirely made up of austenite, it is still possible to find a small amount of ferrite; this is explained by the rapid heating and cooling that does not allow enough time for a complete formation of the austenite. In addition, from 1353 K to 1462 K, the austenite experiences a phase transformation to ferrite, reaching in equilibrium a balanced phase fraction at 1462K . This region, $(2)\gamma/(\alpha + \gamma)$, has the smallest grain size, because the temperature is not high enough to promote grain growth and the deformation rates also allow the dynamic recrystallization. Although similar behavior is observed in the $(1)\alpha + \gamma$ region, the higher temperature in this region promotes a larger grain growth than the $(2)\gamma$ region.

Kim e Yoo (2002) investigated the continuous dynamic recrystallization (CDRX) at high temperatures ranging from 900 $°C$ (1173 K) to 1100 $°C$ (1373 K) of the 430 ferritic stainless steel by torsion tests. The authors reported that CDRX was responsible for the grain refining and that even for temperatures as high as 1100 $°C$, CDRX occurred due to severe deformation.

In another study on dynamic recrystallization, Marchattiwar *et al.* (2013) investigated the 304 austenitic stainless steel behavior when subjected to hot compression at high temperatures, ranging from 900 to 1200 $°C$ (1173 to 1473 K). The results of Electron backscatter diffraction (EBSD) for the sample deformed at 1200 $°C$ (1473 K) showed that the microstructure consisted of large grains when lower strains were applied. However, the authors found a critical strain; beyond which, the DRX takes place, and small-recrystallized grains appear in the microstructure. Furthermore, the density of these tiny grains increases with increasing strain. Both studies have shown that even for temperatures as high as 1100$°C$ (1373 K) or 1200 $°C$ (1473 K), the DRX phenomenon can occur, which is in accordance with the results of the numerical simulation, the microstructural evidence, and the thermodynamic analysis presented here. Therefore, the deformation levels provided by the movement of the FSW tool can provide a microstructural grain refining.

According to Zhao *et al.* (2016), another promising mechanism able to promote grain refinement for ferrite structures is dynamic transformation (DT). This phenomenon occurs when the austenite transforms to ferrite during continuous plastic deformation. This is in accordance with other studies such as those developed by Lee *et al.* (1995) and Park *et al.* (2013). Some studies have reported that both phenomena: dynamic recrystallization and dynamic transformation, can occur simultaneously during the processing of the steel, resulting in grain refinement of the ferritic structure, as pointed out by Abdollah-Zadeh e Eghbali (2007) and Beladi *et al.* (2007). This behavior could explain why even for the transition temperature, when the austenite starts to transform into ferrite at high temperatures (above 1353 K), the grain refining process takes place.

The other regions, ($(3)\alpha + \gamma + Cr_{23}C_6$ and $(4)\alpha + Cr_{23}C_6$), do not show dynamic recrystallization because they do not deform. The $(3)\alpha + \gamma + Cr_{23}C_6$ region reaches temperatures for partial austenitization and the final microstructure consists of martensite (dark gray grains), formed during cooling, and ferrite (light gray grains). There is also the precipitation of chromium carbides ($Cr_{23}C_6$ - black regions). The $(4)\alpha + Cr_{23}C_6$ region does not undergo austenitization, but the heat causes the growth of the ferritic grains and the precipitation of carbides.

The thermodynamic simulation using Thermo-Calc was performed under the equilibrium condition; however, the welding process does not follow this equilibrium condition due to the high heating and cooling speed, and therefore the percentages indicated in Figure 7.9b and 7.9c may not be reached.

Figure 7.9 – Equilibrium phase calculation of AISI 410S stainless steel. *Austenite (γ-phase) is indicated but it only forms at high temperatures. However, during the cooling this austenite becomes a metastable martensite phase (not indicated on the equilibrium diagram).
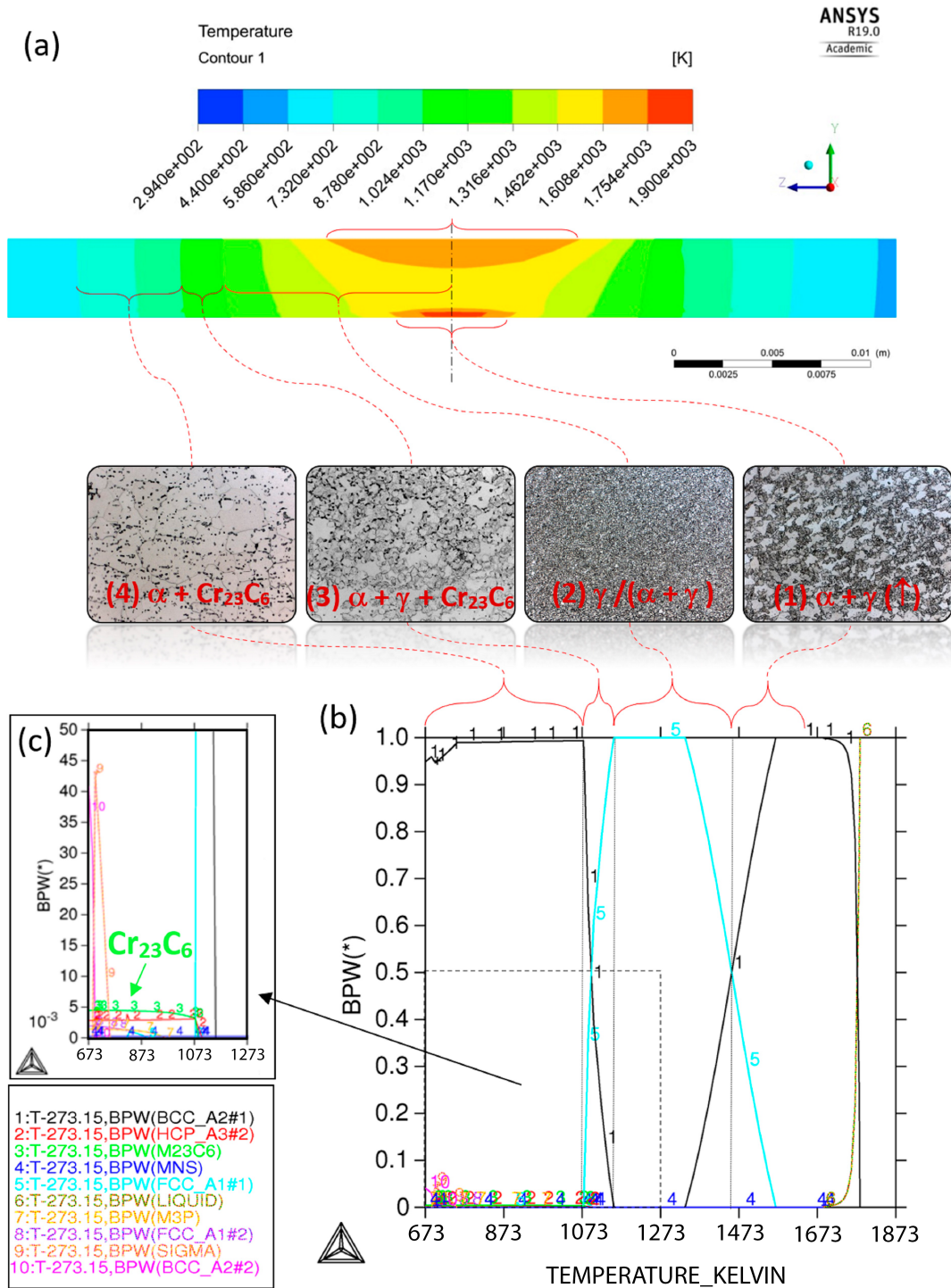
Source: The author

Figure 7.10 shows the temperature field along the cross section of the middle of the pin keeping the rotation constant at 450 rpm and varying the axial force. The axial forces of 10

kN, 15 kN, and 20 kN represent the experimental Tests 1, 2, and 3, respectively. The results with 25 kN and 30 kN were just simulated to observe the effects of higher forces on the temperature field and also on the micro-structure formed.

The test at 450 rpm and 10 kN (Figure 7.10a) was the only one that did not reach the austenitization temperature. This test reaches temperatures of approximately 50% of the melting temperature of the material. Such a low temperature can be harmful to the FSW because the material does not mix appropriately due to the high viscosity of the material .

In Figure 7.10b, the temperature is higher, and the tendency to form austenite increases, but the highest temperature is still less than 80% of the melting point. This temperature also causes problems in mixing the metal within the nugget, as shown in Figure 7.11b. The experimental results showed that when the stir zone reaches temperatures close to or slightly above 80% of the melting point, the tendency to form defects related to a faulty material flow is reduced. Figure 7.10c has a stir zone reaching temperatures close to 80% of the melting point, and consequently, it has achieved the best result among the Tests 1 to 3, as shown in Figure 7.11c.

Regions with temperatures above the 80% of the melting point were observed in Figure 7.10-d and e due to the high axial forces applied. These high temperatures occur because the model used does not take into account the loss of mass. This loss of mass occurs when the viscosity of the material is reduced in a region of high temperatures and consequently, the material tends to be ejected in the form of flashes. Although this model is not valid to predict such a high thermal input accurately, it provides an excellent indication of possible defects that occur during the FSW welding (SILVA *et al.*, 2020c).

Figure 7.11 shows three experimental results for Tests 1 through 3. The results show that the problems mentioned above are due to the low temperatures reached during the FSW; in Figure 7.11a holes due to the inefficient mixing can be seen.

Figure 7.10 – Temperature cross section using a rotation of 450 rpm and different axial forces. a) 410 kN (Test 1 experimental), b) 15 kN (Test 2 experimental), c) 20 kN (Test 3 experimental) d) 25 kN and e) 30 kN.
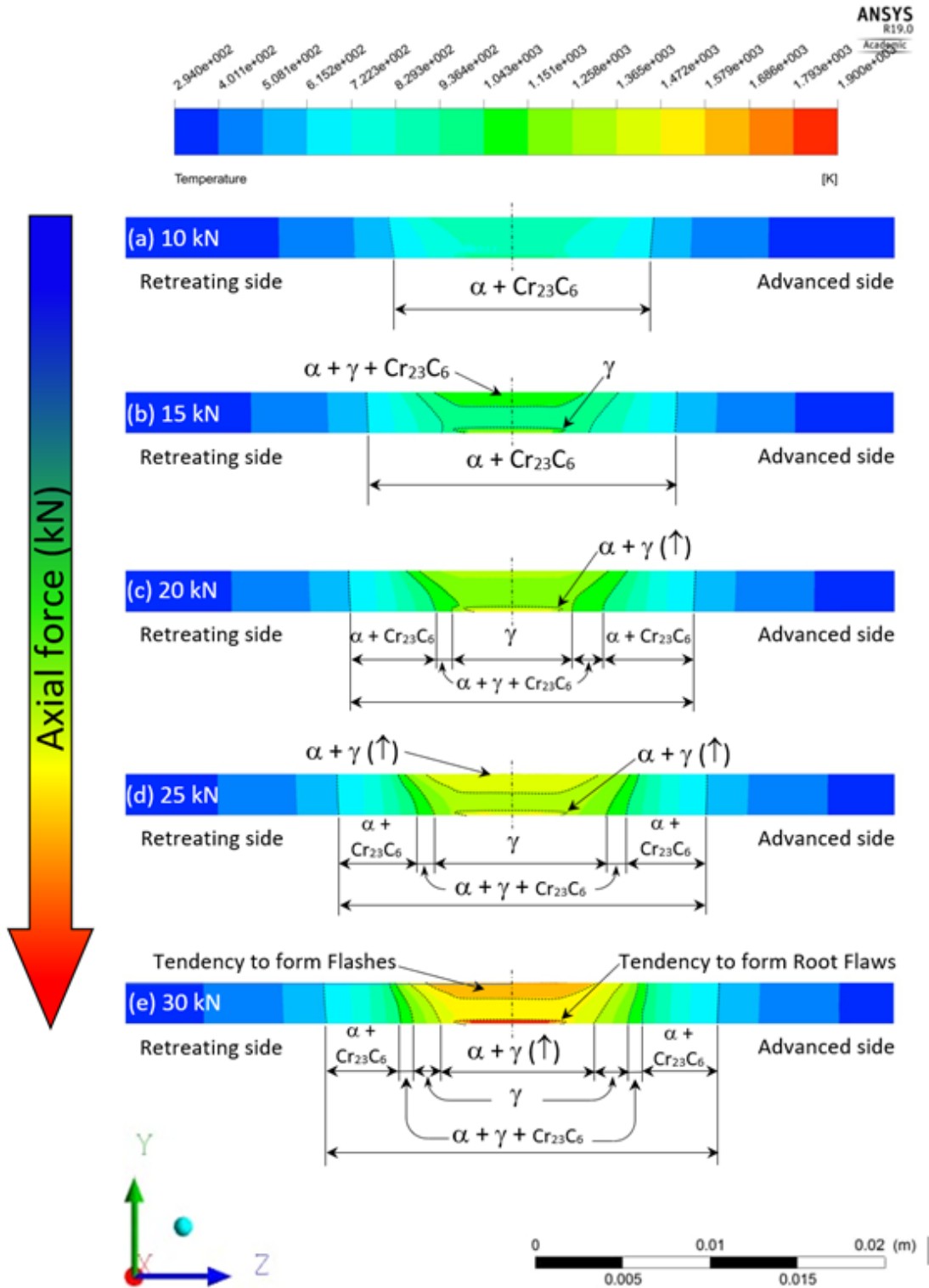
Source: The author

Figure 7.11 – Macrography of experimental tests with a rotation of 450 rpm and different axial forces. a) 10 kN (Test 1), b) 15 kN (Test 2), c) 20 kN (Test 3)
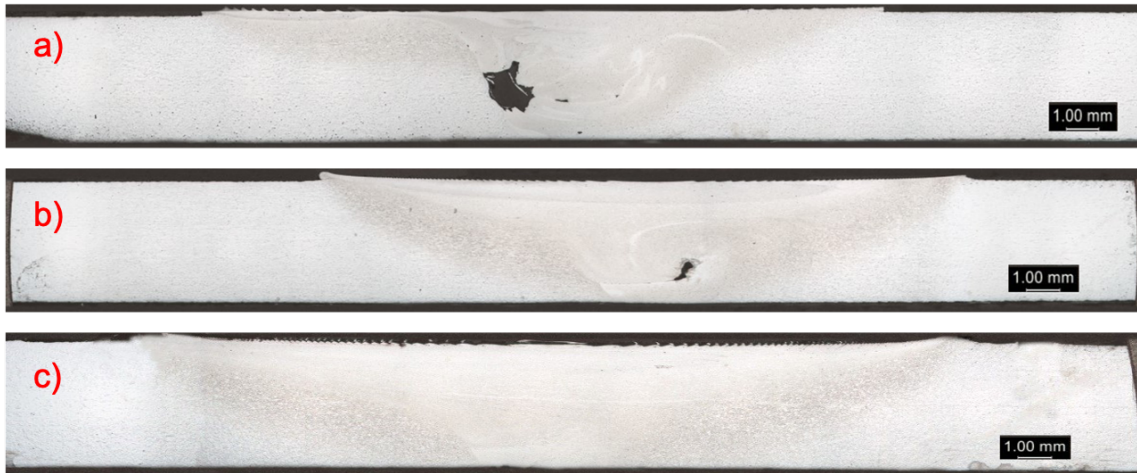
Source: The author

The effect of rotation on the welded material was also investigated. Figure 7.12 shows different simulations for tests with a rotation of 800 rpm and axial forces ranging from 10 to 30 kN. The results with 22 kN (Figure 7.12c), 25 kN(Figure 7.12d), and 30 kN (Figure 7.12e) represent the experimental Tests 4, 5, and 6, respectively. The results with 10 kN and 15 kN were simulated to observe the effect of a low axial force when the rotation is high.

Figure 7.12 clearly shows that the maximum temperature increases with the rotation when compared with the ones presented in Figure 7.10 with a rotation of 450 rpm. Figures 7.12a and 7.12b show that for small axial forces (10 and 15 kN, respectively) flash occured and also the maximum temperature reached was below the melting point of the material.

However, for Test 4 (22 kN in Figure 7.12c), the maximum temperature observed in the simulation is close to the melting point and this can favor the formation of flash because materials with lower viscosity will be expelled. As the temperature increases, the risk of defects in the welding also increases. Figures 7.12d and 7.12e show that the high temperature region is extended. In practice, these temperature levels do not occur but indicate a high risk for the formation of defects (SILVA *et al.*, 2020c).

Figure 7.12 also shows the possible phases that can be formed in the weld. The possibility to form chromium carbide ($Cr_{23}C_6$) and austenite phases exists for all the tests. However, for small axial forces, such as 10 kN in Figure 7.12a, austenite is possibly formed only at the base of the pin, in a small region that is not representative of the weld because the thickness of this region is only 0.3 mm.

Figure 7.12 – Temperature cross section with a rotation of 800 rpm and different axial forces. a) 10 kN, b) 15 kN), c) 22 kN (Test 4 experimental) d) 25 kN (Test 5 experimental), and e) 30 kN (Test 6 experimental).
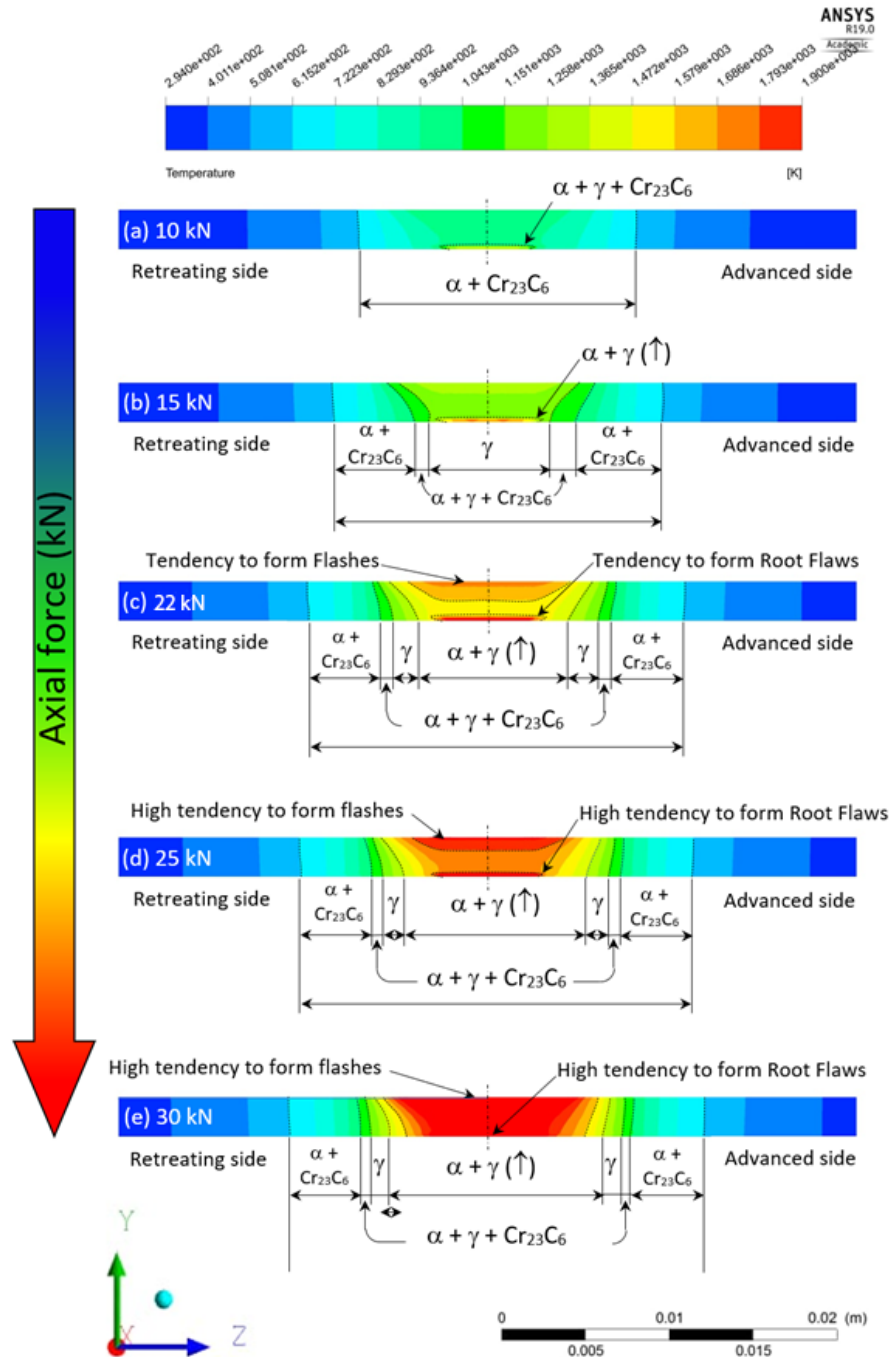
Source: The author

As mentioned before, not only low temperatures but also high temperatures impose drawbacks to the welding region. Figure 7.13 shows the top of the workpiece for Tests 3 (450 rpm 20 kN) and 4 (800 rpm - 22kN), respectively. This Figure demonstrates that the flash formation increases when the rotation is increased. As was discussed and presented above in

Figure 7.12c, such behavior occurs when the simulated temperature approaches the melting point.

Figure 7.13 – Experimental images. a) Test 3 (450 rpm - 20 kN) and b) Test 4 (800 rpm - 22 kN)
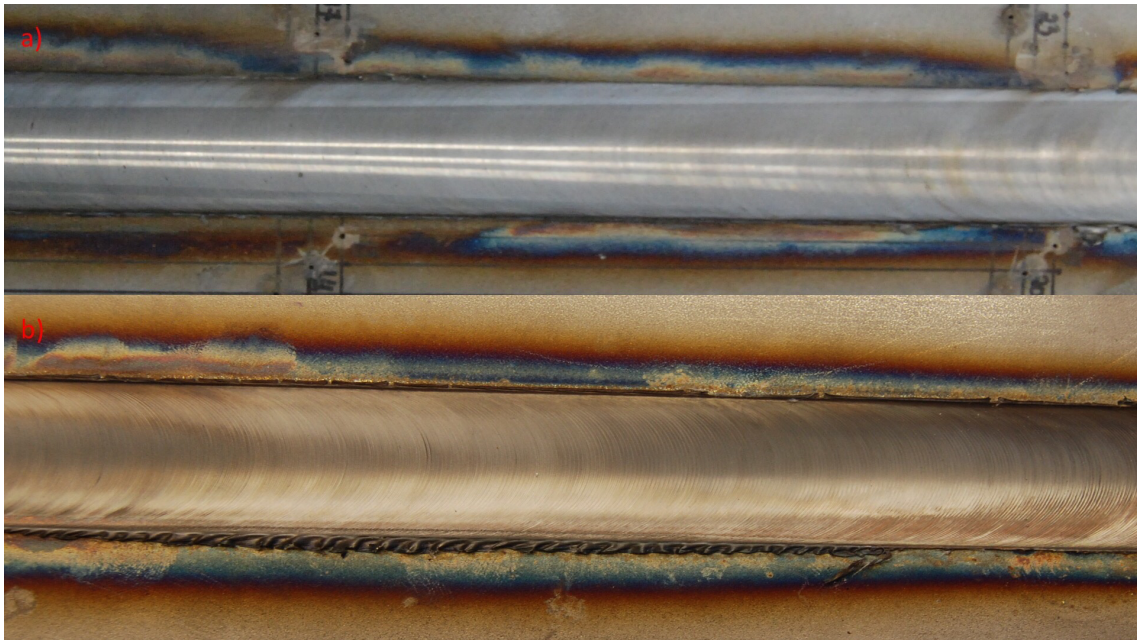
Source: The author

Figure 7.14 presents the macrography for Test 6 (800 rpm and 30 kN). This figure shows the formation of many flashes. This result was predicted in Figure 7.12e due to the high temperature verified in the simulation.

Figure 7.14 – Macrography of Test 6 with 30 kN of axial force and 800 rpm

Source: Caetano (2016)

The increase in flash formations can also be verified by the parameter Y presented by Silva *et al.* (2020c). According to the authors, the flash formation can be related to the axial pressure, rotation, and viscosity by

$$Y = \frac{P}{\omega \cdot \mu_{min}} \tag{7.24}$$

The growth of parameter Y shows the tendency of the material to generate flashes during the welding. Table 7.5 presents the parameter Y for the Tests 1 through 6 of Table 7.1. Table 7.5 shows that the flashes observed in the previous results may be associated with a high value of the parameter Y.

Table 7.5 – Experimental parameters used

	Y ($Pa/rpm \cdot Pa.s$)
Test 1	52.29
Test 2	94.35
Test 3	104.58
Test 4	129.56
Test 5	155.90
Test 6	188.29

Source: The author

These materials can undergo martensitic transformation with high cooling rates from the austenite regions. Figures 7.10 and 7.12 show that austenite can be formed in all tests, except for the 450 rpm and 10 kN (Figure 7.10-a) test.

In order to observe the effect of the cooling rates on the final structure, we evaluated the cooling rates at eight different points (four on the advanced side and four on the retreating side) for Tests 1 and 4. On each side, two points are near the pin wall and two points are near the end of the shoulder. As shown in Figure 7.15, for each position, the cooling rates were evaluated at the top and the base of the workpiece around the pin and shoulder. Tests 1 and 4 were chosen because the parameters used in these tests (rotation and axial force) were the largest parameters that reproduced the maximum temperature expected in the FSW.

Figure 7.15 – Cross section at the positions where the cooling curves were evaluated.
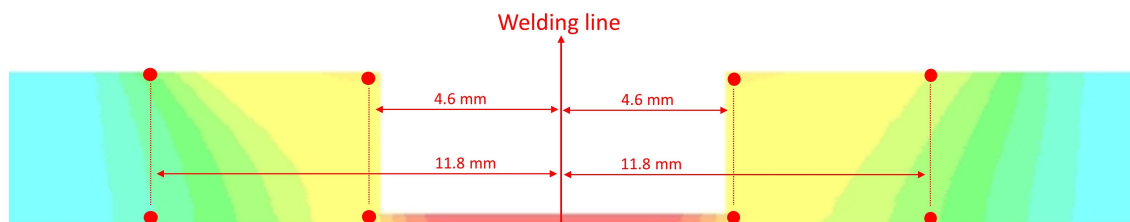
Source: The author

Figure 7.16 presents the CCT diagram and the martensitic transformation at the selected positions of Figure 15, for Tests 1 and 4. The results in Figure 7.15 show that all cooling rates are large enough to produce martensite. As discussed previously, martensite is formed from austenite during high cooling rates. The welding process is a non-equilibrium process that is submitted, in some situations, to extremely high heating and cooling rates. Therefore, it is

possible to obtain welded structures composed of martensite and ferrite, because the ferrite was not completed transformed in austenite during the heating. These results are in agreement with the experimental ones obtained by Caetano *et al.* (2019) who observed the presence of martensite in the welded materials. Furthermore, the CCT diagram does not show any carbide formations. However, during welding, carbon migration in the structure begins both in heating and cooling and this allows the formation of carbides distributed in the structure.

Figure 7.16 presents the CCT diagram and the martensitic transformation in the select positions of Figure 7.15, for tests 1 and 4. From the results shown in Figure 7.16, it is possible to observe that all cooling rates are large enough to produce martensite. As we discussed in a previous section, martensite is formed from austenite during large cooling rates. The welding process is a non-equilibrium process that is submitted, in some situations, to extremely large heating and cooling rates. Therefore, it is possible to obtain welded structures composed of martensite and ferrite, because the ferrite was not completed transformed in austenite during the heating. These results are in agreement with experimental ones obtained by Caetano *et al.* (2019) that observed the presence of martensite in the welded materials. It is also important to note that although the CCT diagram does not show carbide formation. However, during the welding, the carbon migration in the structure begins during both heating and cooling and this allows the formation of carbides distributed in the structure.

Figure 7.16 – CCT diagram with cooling curves. a) advancing side of Test 1 - 450 rpm and
10 kN, b) retreating side of Test 1 - 450 rpm and 10 kN, c) Advancing side of
simulation with 800 rpm and 22 kN, and d) retreating side of simulation with
800 rpm and 22 kN. M - Martensite, A - Austenite, F - Ferrite, C - Carbite
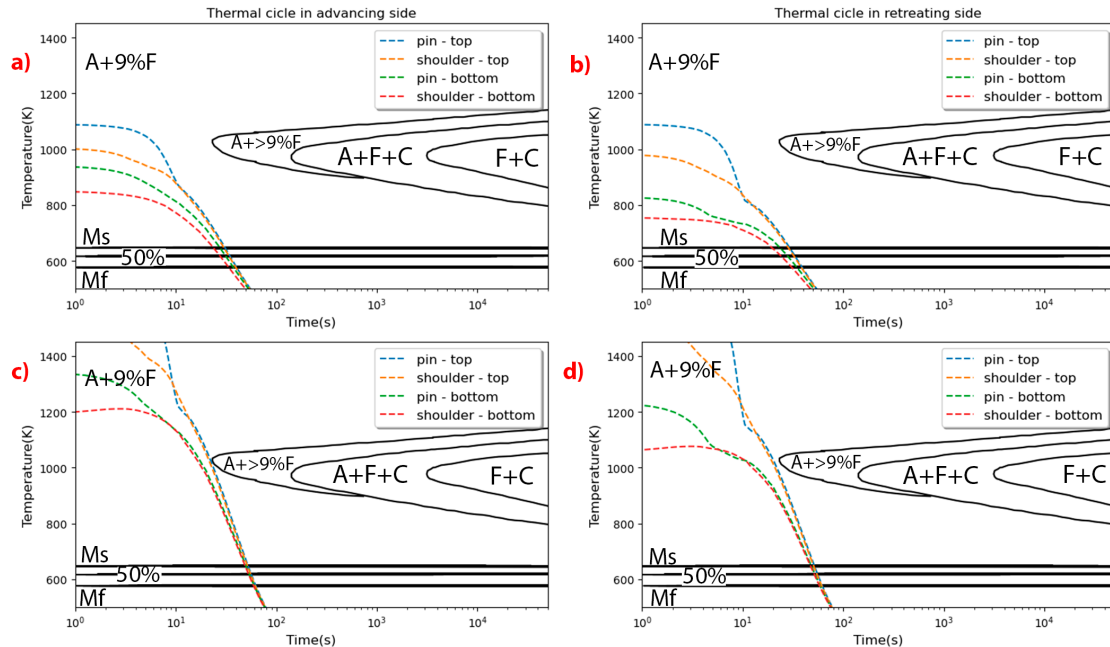
Source: Rickett *et al.* (1952)

Another important phenomenon associated with the microstructure in FSW welds
is the dynamic recrystallization, which occurs due to high temperatures and high deformation
rates verified during the process. The Zener-Hollomon parameter (Z) is used to analyze this
phenomenon because it depends on the strain rate and temperature. The Zener–Hollomon
parameter was studied by Chang *et al.* (2004), who demonstrated a linear relationship between
the Z parameter and the grain size; the grain grows when Z decreases and vice versa.

In order to observe the combined effect of temperature and strain rates in the grain
growth, the Zener–Hollomon parameter was calculated at twelve points, six on the advancing
side and six on the retreating side, as shown in Figure 7.17.

Figure 7.17 – Cross section with the positions where the Zener–Hollomon parameter was
calculated.
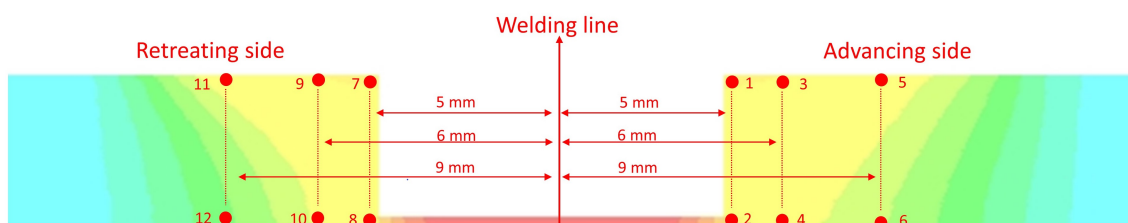
Source: The author

Table 7.6 presents the Z parameter for Test 3 (20 kN and 450 rpm) at the positions of Figure 7.17. Based on these data, it was found that Zener–Hollomon parameters of points 1-7 and 3-9 (located at the top) are smaller than the ones of points 2-8 and 4-10 (located at the base). The lowest Zener–Hollomon values (points 1-7 and 3-9) indicate that the largest grain size will be located at the top of the welded material.

However, for the points farthest from the pin (points 5-11 and 6-12), the Zener–Hollomon parameters at the top are larger than the ones at the bottom, which indicates more refined grains at the top. This behavior is contrary to the behavior observed around the pin (points 1-7, 2-8, and 3-9, 4-10). This occurs because points 5-11 (located at the top) are in the stir zone and points 6-12 (located at the bottom) are in the heat-affected zone, where there is no effect of the strain rate, as commented before.

Table 7.6 – Zener-Hollomon parameter for Test 3.

	Advancing side		Retreating side
Points	log(Z)	Points	log(Z)
1	15.67	7	15.67
2	16.19	8	17.13
3	16.49	9	16.49
4	17.03	10	17.03
5	18.64	11	18.67
6	16.24	12	17.68

Source: The author

The same grain behavior for the AISI 410S stainless steel was obtained by Andrade *et al.* (2015) who performed dissimilar welding of the AISI 410S stainless steel and AISI 304S stainless steel. The welding parameters in the current simulation were similar to the ones used by those authors. They also verified that the grain size in the stir zone at the top is smaller than that at the base. This result is in accordance with the results presented by the Z parameter at points 1-7, 3-9, 2-8, and 4-10 of the present work. The grain size at points 5-11 and 6-12 also agree with the results of Andrade *et al.* (2015), because points 5-11 are located in the stir zone and points 6-12 are located in the heat-affected zone.

7.6   Conclusions

The present work performed a numerical and experimental investigation of the parameters that affect the FSW process with AISI 410S stainless steels. Based on the simulated and experimental results of this study it was possible to conclude that when the temperature in

the stir zone was close to 80% of the melting temperature, the tendency to form weld defects was significantly reduced. Lower temperatures can cause mixing problems, and higher temperatures will give rise to flashes. The combination of the results of temperature, viscosity, and velocity in the cross-section helped predict the stir zone, the thermomechanically affected zone and the heat affected zone with good precision. The thermodynamic analyses predicted the austenitization of the materials, and the CCT diagram showed that all the austenitized regions tended to transform into martensite due to the high cooling rates. The formation of carbides in the heat affected zone can also be predicted. Having calculated the Zener–Hollomon (Z) values, it was possible to predict which regions had more refined grains as a consequence of the dynamic recrystallization. Also smaller grains were observed at the base of the stir zone compared to the top of the stir zone.

8 NUMERICAL INVESTIGATION OF DISSIMILAR FRICTION STIR WELDING OF AISI 304L AND 410S STAINLESS STEELS

8.1 Review

This article analyzed the simulation dissimilar FSW of ferritic stainless steel with authentic stainless steel in order to observe the temperatures reached and the mixed between this materials. The VOD model was used to modeled the mixed and the method was efficient in choosing the best side for each material, allowing problems related to their mixture.

8.2 Introduction

Dissimilar welding is a necessary for many industrial applications as it allows the joining of materials with different chemical compositions, structures, and properties, as pointed out by Dak e Pandey (2020) who reported on dissimilar welding in energy industries, and by Gullino *et al.* (2019) who reported on welding aluminum to steel in the automobile industry. Dissimilar welding techniques optimize the use of each material according to its specific properties for each usage or condition, as discussed in the studies of Fang *et al.* (2019) and Hosseini *et al.* (2011). Traditionally, dissimilar welding has been performed by different fusion welding processes with some success. However, such procedures have some limitations, especially regarding the metallurgical phenomenon during the solidification and cooling stages.

An example where dissimilar welding is feasible is the manufacturing of ferritic stainless steel (FSS) joints. Although, FSSs are a class of alloys with some limitations for fusion welding, their lower cost compared with other classes of stainless steels has been recognized as an advantage. They experience a monophasic solidification process, which results in ferrite as the only solid phase. This causes coarse grains in the fusion zone (FZ) and in the heat affected zone (HAZ) and consequently impairs their properties, as reported by Silva *et al.* (2008b). Pickering e FB (1976) highlighted that the grain growth in the FZ and HAZ is due to the absence of phase transformation. In these cases, Silva *et al.* (2013) suggested the use of other types of stainless steels such as austenitic steels as the filler material. Also, some low Cr ferritic stainless steels, like 409 and 410S, may be subject to martensitic transformation, as reported by Mola e Cooman (2011) and SILVA C. C. (2006). This behavior occurs because the ferrite that is partially converted into austenite at high temperatures can be converted into martensite during fast cooling as explained by Pistorius e Rooyen (1995) and Warmelo *et al.* (2007).

Ferritic stainless steels can also experience a drop in their properties due to some harmful effects caused by carbide/nitride precipitations and intermetallic phases. Silva *et al.* (2008b) reported that the formation of different kinds of precipitates in the HAZ of 444 steel, such as CrN, Cr_7C_3, $Cr_{23}C_6$, sigma, chi, and Fe2Nb Laves phase. Kuzucu *et al.* (1997) reported the formation of $M_{23}C_6$, NbC, and sigma, in ferritic stainless steel containing 17–18 wt.% Cr under heat treatment, and they also observed a decrease in toughness. Sello e Stumpf (2011) also investigated the Laves phase formation in ferritic stainless steels, and highlighted that this phase plays a significant role in toughness. These metallurgical changes may impair critical metallurgical changes such as mechanical strength, toughness, and corrosion resistance. On the other hand, austenitic stainless steels have a remarkable toughness and weldability, as pointed out by Folkhard (1988). Nonetheless, they are prone to sensitization due to chromium depletion caused by the precipitation of $Cr_{23}C_6$ carbides, as highlighted by Dayal *et al.* (2005).

Even with their limited use due to their inherent properties, FSSs are still an excellent option mainly due to their low cost. Therefore, it is crucial to overcome this lower weldability in order to expand the use of ferritic stainless steels. Ferritic stainless steels have also been used in projects associated with other steels, especially austenitic steels, which brings about the challenges of dissimilar welding.

Advances in manufacturing processes such as the solid-state welding process called Friction stir welding (FSW) that was developed by The Welding Institute (TWI) in the 1990s (THOMAS *et al.*, 1991), has opened up new perspectives for joining materials. Recently, studies on the friction stir welding (FSW) process have demonstrated that FSW is a promising joining method to avoid some of the problems related to fusion and solidification because the joining occurs in a solid-state (at a temperature of 80% of the melting point, as cited by Mishra e Ma (2005), or close to 90% of the melting point, as claimed by Qian *et al.* (2013). Besides this lower temperature peak reached during the process, the plastic deformation produced by the movement of the tool can promote the dynamic recrystallization phenomenon, as highlighted by Nandan *et al.* (2008b), and this phenomenon strongly affects the microstructure and mechanical properties. Although the FSW process has several advantages, parameter adjustment is a key issue to employ the FSW technique successfully.

There are some studies in the literature devoted to FSS welding by FSW. Cho *et al.* (2011) investigated the welding of 409 FSS by FSW, and demonstrated that it was possible to produce a high-quality defect-free welded joint. Lakshminarayanan e Balasubramanian (2010)

using a welding speed of 50 mm/min and rotation speed of 1000 rpm successfully welded a 409 FSS by FSW that resulted in joints free of volumetric defects. Caetano *et al.* (2019) investigated the relationship between rotation speed and axial force in the formation of defects in AISI 410S ferritic stainless steels welded by FSW. These authors reported that the production of joints without root flaws is achieved through the correct balance between the axial force and the rotation speed, allowing a greater immersion of the tool probe into the joint

An important feature of FSW (in terms of dissimilar welding) is that there is almost no chemical mixing. This characteristic can be observed in the study developed by Anaman *et al.* (2019), who FSW welded aluminum alloy and steel, and the results showed minimal chemical mixing. However, there is still a lack of information when the focus is on joining ferritic to austenitic stainless steels and how the main parameters can affect the quality of the joints, including volumetric defects. Recently, Caetano *et al.* (2021) developed a study on the dissimilar welding of AISI 410S and 304L steels, varying several parameters to achieve a good surface finish, no voids, and full tool penetration. Their results demonstrated that it is possible to produce dissimilar joints between AISI 410S/304L steels by the FSW process free of defects in the stir zone.

Nonetheless, a greater understanding of the parameters that affect the heat generation and the material flow are extremely important to optimize the FSW process. Advances in computational tools enable the modeling of the aforementioned conditions, providing reliable and useful data that can clarify the stirring mechanism based on the visco-elastoplastic behavior of these materials at high temperatures and therefore problems that could occur during the FSW welding can be predicted. Frigaard *et al.* (2001) was the first to propose a model to describe the heat generated in aluminum by FSW. Later on, Seidel e Reynolds (2003) proposed a model to describe the material flow around the tool, based on a 2D fluid flow that took into account the contribution of the plastic deformation on the heat generation. Sheppard e Wright (1979) developed a viscosity model as a function of the temperature and the strain rate. Subsequent studies applied this same approach to evaluate the heat generation and material flow for specific materials such as mild steel, as proposed by Nandan *et al.* (2007); austenitic steel, as pointed out by Zhu e Chao (2004); and for ferritic steel, as reported by Cho *et al.* (2013). Silva *et al.* (2020c) performed a FSW simulation of AISI 304L stainless steel using the finite volume method for a range of welding parameters. These simulations were able to predict defects, as well as flashes and holes for some welding parameters.

With advances in numerical simulations of the FSW process, many studies have addressed the modeling of dissimilar welding in which a non-uniform heat generation and strain rate must occur. The differences of the chemical and physical properties of the welded materials result in a complex behavior of material flow in the stir zone. A literature survey has shown limited information regarding simulation of dissimilar materials such as Al to Mg alloys, as reported by Patel *et al.* (2019a) who evaluated the horizontal material flow from the advancing side to the retreating side and the vertical material flow from top to bottom in FSW, with good agreement with their experimental data. In another study, Yang *et al.* (2018) evaluated the material mixing and distribution for Al-Cu dissimilar welds, introducing a local turbulent flow below the tool pin, which has been considered a pivotal factor to describe the mixing zone formation. Hernández *et al.* (2017) used the FLUENT computational fluid dynamics package to study the transient and steady-state models for the dissimilar welding of two different carbon steels with different carbon contents and concluded that the distribution of the spatial materials due to the stirring were dependent on the rotation and welding speed. Pankaj *et al.* (2020) also simulated an FSW dissimilar weld based on the combination of low carbon and high strength steels, using the finite element method (FE). The numerical model was able to predict the temperature peak successfully. Another advance includes the simulation of Al to steel in underwater welding conditions, as reported by Eyvazian *et al.* (2020). However, to the best of our knowledge, no numerical investigation of the FSW process using dissimilar ferritic to austenitic stainless steels has been performed.

Thus, an international collaboration between the Welding Research and Technology Laboratory at the Universidade Federal do Ceará, in Brazil, and the Institute of Materials Research at the Helmholtz-Zentrum Geesthacht GmbH, in Germany, was set up. This partnership has developed a series of experimental and numerical studies on the welding of similar and dissimilar stainless steels by the FSW process. The main objective of this work is to develop a reliable numerical simulation to predict the heat generation, material flow, and the tendency to form volumetric defects in dissimilar welds between AISI 410S ferritic stainless steels and AISI 304L austenitic stainless steels. In order to do this the position of the materials and some welding parameters such as rotation speed and axial force were varied. Furthermore, the numerical data was validated against a set of experimental tests.

8.3   Materials and Experimental Data

In this work, two 200x500x4 mm stainless steel plates: AISI 410S and AISI 304L were used. The total length of the weld was 500 mm. All welds were made using the HZG Gantry System at the Helmholtz-Zentrum Geesthacht (HZG) GmbH, in Germany. The position of the steel plates and the simulated parameters used in this study are shown in Table 8.1.

Table 8.1 – FSW welding Parameters

	Advancing Side	Retreating Side	Axial Force (kN)	Rotational Speed (rpm)	Weld Speed (m/s)
Teste 1	AISI 410S	**AISI 304L**	40	450	1
Teste 2	**AISI 304L**	AISI 410S			
Teste 3	AISI 410S	**AISI 304L**	40	650	1
Teste 4	**AISI 304L**	AISI 410S			
Teste 5	AISI 410S	**AISI 304L**	30	450	1
Teste 6	**AISI 304L**	AISI 410S			

Source: The author

The tool used in the experimental and simulated tests was made of Polycrystalline Cubic Boron Nitride (PCBN) and argon was used as the shield gas. The chemical compositions of the AISI 410S and the AISI 304L stainless steels are given in Table 2 and the thermal properties of the tool and the steel are shown in Table 8.3 and 8.4.

Table 8.2 – Chemical composition of stainless steels(% mass)

Material	Fe	C	Cr	Mn	Ni	P	Si	S	Mo
410S	Bal	0.025	12.8	0.3	0.21	0.023	0.37	<0.010	0.014
304L	Bal	0.026	18.5	1.21	7.94	0.029	0.32	<0.010	0.29

Source: The author

Table 8.3 – Thermal proprieties of AISI 410S stainless steel

Temperature (K)	Density (Kg m^3)	Specific heat capacity (J kg^{-1} K^{-1})	Thermal conductivity (J kg^{-1} K^{-1})
298	7800	-	-
373	7794	473	27.6
473	7786	515	27.6
673	7768	607	26.4
873	7749	-	25.1
1073	7730	691	-
1273	7712	-	21.8

Source: Cho *et al.* (2013)

Table 8.4 – Thermal proprieties of tool material and AISI 304L stainless steel

Material	Density (kg/m^3)	Thermal Conductivity $(W/m \cdot K)$	Specific Heat $(J/kg \cdot K)$
304L	$7.97 \cdot 10^3 - 6.01 \cdot 10^{-2} \cdot T$ $-1.12 \cdot 10^{-3} \cdot T^2$ $+6.16 \cdot 10^{-0.7} \cdot T^3$	$19.36 - 0.02960 \cdot T$ $+6.525 \cdot 10^{-5} \cdot T^2$ $-2.88 \cdot 10^{-8} \cdot T^3$	$431.73 + 0.2879 \cdot T$ $-0.000131237 \cdot T^2$ $+3.85 \cdot 10^{-9} \cdot T^3$
PCBN	3450	120	750

Source: Almoussawi e Smith (2018) and Nandan *et al.* (2006a)

8.4 Physical Model

8.5 Physical Model

In this study, the beginning and ending of the welding line were not analyzed, since these regions are not a representative part of the weld. Therefore, the results will focus on the intermediate section of the welding line, which has a constant heat generation and the cross-section has similar properties, geometry, and structure. The aforementioned features indicate that intermediate region can be modeled by a steady state regime (SONG *et al.*, 2014).

In the steady state simulation of the intermediate section of this work, the shoulder was assumed to be in contact with the top surface of the workpiece, as shown in Figure 1. In addition, the pin penetrates the workpiece fully. Throughout the welding period, pressure, rotation, and welding speed were considered constant and $\tau = \sigma_{yield}/\sqrt{3}$, where σ_{yield} was evaluated using the distortion energy theory considering a two-dimensional plane stress.

Figure 8.1 – Schematic diagram of the FSW simulation. a) velocity boundary conditions and b) top view of the tool.
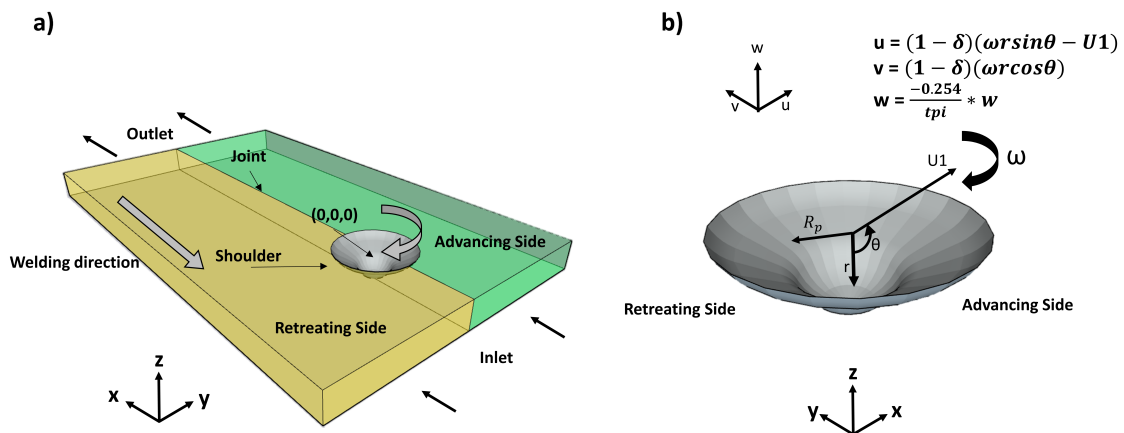
Source: The author

The materials were assumed to be non-Newtonian, incompressible, and viscoplastic

fluids. A partial sticking condition between the tool and the workpiece was assumed and the tilt angle of the tool was set to zero (NANDAN *et al.*, 2006a). The reference coordinates were fixed at the center of tool at the top of workpiece. A non-uniform grid only composed of hexahedrons was modeled using the ICEM-Mesh Software and used for all simulations. A mesh refinement was performed in order to obtain mesh-independent results.

The volume of fluid (VOF) was used to obtain the volume of each phase in the mixed zone of the dissimilar weld region as defined by ANSYS. In this method, the interface between the phases is solved by a continuity equation for one or more phases, as given by (ANSYS, 2009)

$$\frac{1}{\rho_q}\left[\frac{\partial}{\partial t}\left(\alpha_q \rho_q\right) + \nabla \cdot \left(\alpha_q \rho_q \vec{v}_q\right) = \sum_{p=1}^{n}\left(\dot{m}_{pq} - \dot{m}_{qp}\right)\right] \tag{8.1}$$

where $\dot{m}_{pq}$ is the mass transfer between phase p and phase q, in which for this simulation it was set to zero, because in the FSW the chemical mixture is minimal. ρ refers to the density of each phase and α represents the phase fraction.

8.5.1   Governing Equations

Using the aforementioned approaches, the continuity equation is given by

$$\frac{\partial u_i}{\partial x_i} = 0 \; ; \; i = 1,...,3 \tag{8.2}$$

where u_i denotes the velocity of plastic flow at the x-(1), y-(2), and z-(3) coordinates. Equation 8.2 states that the volume variation is zero. The momentum conservation equation with reference to a co-ordinate system attached to the tool using the indicial notation again, is given by (CHO *et al.*, 2013)

$$\frac{\partial \rho u_j}{\partial t} + u_i \frac{\partial u_j}{\partial x_i} = -\rho \frac{\partial P}{\partial x_j} + \frac{\partial}{\partial x_i}\left(\frac{\partial \mu u_j}{\partial x_i}\right) - \rho U \frac{\partial u_j}{\partial x_j} \tag{8.3}$$

where U is the weld velocity, ρ is the density, P is the pressure, and μ is the non-Newtonian viscosity of the material. The viscosity model used for both materials (AISI stainless steel 410S and AISI stainless steel 304L) are described in 3.3 and 3.4 respectively. The conservation energy equation is given by

$$\frac{\partial(\rho C_P T)}{\partial t} + \frac{\partial(\rho C_P u_i T)}{\partial x_i} = -\rho C_P U_1 \frac{\partial T}{\partial x_1} + \frac{\partial}{\partial x_i}\left(k \frac{\partial T}{\partial x_i}\right) + S_i + S_b \tag{8.4}$$

The simulation was performed in a steady-state regime. However, the transient terms were kept in the Equations (8.1, 8.3, and 8.4) in order to reach the steady state regime through a distorted transient. In Equation (8.4), ρ represents the density, C_P indicates the specific heat, and k refers to thermal conductivity. S_i is a source term that denotes the rate of energy per unit of volume dissipated by friction between the tool and the workpiece, and S_b is a source term that denotes the rate of energy per unit of volume generated by plastic deformation in the workpiece away from the interface. These two source terms are defined below.

8.5.2 Source Terms and Boundary Conditions

The heat sources were added to the FLUENT commercial software by means of a UDF (user-defined function). The S_i source term is defined in FLUENT as the heat flux, and is defined by

$$S_i = q_1 \frac{A_r}{V} \tag{8.5}$$

where A_r is the contact area between the tool and workpiece and V is the volume enclosing A_r. $q_1 [W/m^2]$ is the heat generated by the contact between the shoulder of the tool and the workpiece, which is defined by

$$q_1 = \left[\delta \eta \tau + (1-\delta)\mu_f P\right](\omega r - U_1 \sin\theta) \tag{8.6}$$

In the above equations, P indicates the normal pressure of the tool during welding, ω is the angular velocity, U_1 is the welding speed, η is the thermal efficiency, and the term composed by $(\omega r - U_1 \sin\theta)$ represents the relative velocity between the tool and the workpiece. $\sin\theta$ is defined by

$$\sin\theta = \frac{y}{r} \tag{8.7}$$

$$\cos\theta = -\frac{x}{r} \tag{8.8}$$

$$r = \sqrt{x^2 + y^2} \tag{8.9}$$

where r is the radius of the global axis fixed at the center of the tool.

In Eq. (8.4), the term S_b indicates the source term per volume unit generated by plastic deformation in the workpiece away from the interface. This heat source is defined in FLUENT as the heat generation rate in the boundary conditions. This source term has been calculated as $f_m\mu\Phi$, where μ designates the viscosity, and f_m is an arbitrary constant that indicates the extension of atomic mixing in the system. In this study, a value of 0.04 was used for f_m and Φ (CHO *et al.*, 2013) is given by

$$
\begin{aligned}
\Phi = 2\left(\left(\frac{\partial u_1}{\partial x_1}\right)^2 + \left(\frac{\partial u_2}{\partial x_2}\right)^2 + \left(\frac{\partial u_3}{\partial x_3}\right)^2\right) + \left(\frac{\partial u_1}{\partial x_2} + \frac{\partial u_2}{\partial x_1}\right)^2 \\
+ \left(\frac{\partial u_1}{\partial x_3} + \frac{\partial u_3}{\partial x_1}\right)^2 + \left(\frac{\partial u_3}{\partial x_2} + \frac{\partial u_2}{\partial x_3}\right)^2
\end{aligned}
\tag{8.10}
$$

The heat generated by the contact of the tool and the workpiece is split between them. The fraction that is inputted to the plate (f) is defined by (NANDAN *et al.*, 2008b)

$$
f = \frac{J_w}{J_t + J_w}
\tag{8.11}
$$

where J_i is defined by the following equation:

$$
J_i = \sqrt{\rho C_p k}
\tag{8.12}
$$

In Eq. (8.12), $i = w$ or t for the workpiece and the tool, respectively. A convection boundary condition was established on all faces of the plate. For the upper surface of the plate, the radiation flux between this face and surrounding as combined with the convection heat flux. Having established the above conditions, the boundary conditions for the bottom, side, and top of the plate are respectively given by the following equations:

$$
k\frac{\partial T}{\partial z} = h_b\left(T - T_e\right)
\tag{8.13}
$$

$$
\pm k\frac{\partial T}{\partial y} = h_s\left(T - T_e\right)
\tag{8.14}
$$

$$-k\frac{\partial T}{\partial z} = h_t\,(T - T_e) + \sigma\varepsilon(T^4 - T_a^4) \tag{8.15}$$

where h_b, h_s, and h_t are the heat convection coefficients for the bottom, side, and top of the workpiece, respectively, T_a is the environmental temperature, and k is thermal conductivity.

Under boundary conditions, the velocities generated on the materials by contact between the tool and workpiece were also prescribed. These velocities were developed after an analysis of real tool, as shown in Figure 8.2.

Figure 8.2 – Model of the tool.
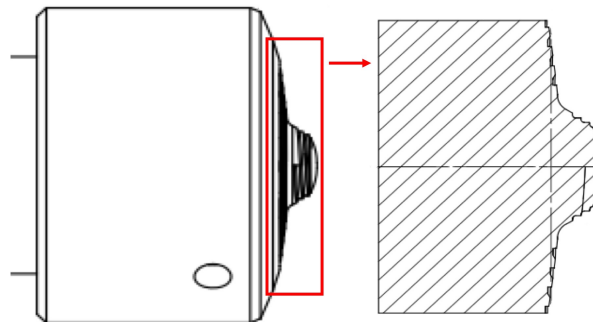
Source: The author

The threads in the tool cause two effects on the velocity field. First, a radial velocity in the opposite direction of radius growth, and second, a vertical velocity. Both effects cause a material flow towards the bottom of the workpiece. These threads are used to reduce the production of flashes. The effect of threads on the tool were included in the Fluent simulator using the UDF by the following equations:

$$u = (1 - \delta)(\omega r \sin\theta - U_1) \tag{8.16}$$

$$v = (1 - \delta)(\omega r \cos\theta) \tag{8.17}$$

$$w = \frac{-0.0254}{tpi} \cdot \omega \tag{8.18}$$

where R_p is the radius and tpi designates threads per inch.

8.5.3 AISI 410S stainless steel flow stress

The viscosity model used in the simulation of the AISI 410S stainless steel was based on the formulation of the flow stress (σ_e) proposed by Sheppard and Wright (1979)(SHEPPARD; WRIGHT, 1979), where the flow stress is a function of the effective strain rate ($\dot{\varepsilon}$) and temperature (T), which is given by

$$\sigma_e = \frac{1}{\alpha} \sinh^{-1}\left[\left(\frac{Z}{A}\right)^{\frac{1}{n}}\right] \tag{8.19}$$

where α, A, and n are the material constants and Z is the Zener–Hollomon parameter that is a function of temperature and the effective strain rate, and is given by

$$Z = \dot{\varepsilon}\exp\left(\frac{Q}{RT}\right) \tag{8.20}$$

In Eq. (8.20), Q denotes the temperature-independent activation energy and the $\dot{\varepsilon}$ designates the effective strain rate, which, assuming infinitesimal deformation is given by

$$\dot{\varepsilon} = \left(\frac{1}{2}\dot{\varepsilon}_{ij}\dot{\varepsilon}_{ji}\right)^{\frac{1}{2}} \tag{8.21}$$

$$\dot{\varepsilon}_{ij} = \frac{1}{2}\left(\frac{\partial u_i}{\partial x_j} + \frac{\partial u_j}{\partial x_i}\right) \tag{8.22}$$

The above equations were incorporated into the FLUENT Software using a User Definition Function (UDF). However, as the UDF does not have the function $\sinh^{-1}$, this function in Eq. (8.19) was replaced by

$$\sinh^{-1}\left[\left(\frac{Z}{A}\right)^{\frac{1}{n}}\right] = \ln\left\{\left(\frac{Z}{A}\right)^{\frac{1}{n}} + \sqrt{\left[\left(\frac{Z}{A}\right)^{\frac{2}{n}} + 1\right]}\right\} \tag{8.23}$$

Figure 8.3-a shows the viscosity profiles using the model described above for the AISI 410S stainless steel.

Figure 8.3 – Computed contours of viscosity (Pa.s) as a function of temperature and strain rate. a) AISI 410S stainless steel b) AISI 304L stainless steel
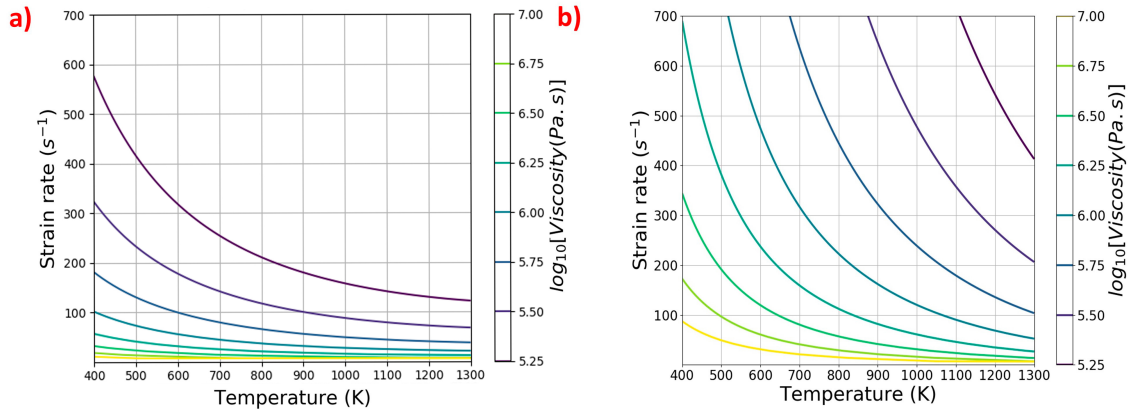
Source: The author

8.5.4 AISI 304L stainless steel flow stress

The flow stress for the AISI 304L stainless steel followed a viscosity model based on the simplified Hart's model (HART, 1976). In this model, the flow stress (σ_e) is calculated using the sum of σ_p (plastic contribution) and σ_v (viscous contribution).

$$\sigma_e = \sigma_p + \sigma_v \tag{8.24}$$

The plastic contribution indicates the flow resistance from dislocation entanglement, whereas the viscous contribution represents the frictional force. In this model, both plastic and viscosity contributions depend on the temperature and strain rate, and are given by Hart (1976) as

$$\sigma_p = k_1 \exp\left[-\left(\frac{b}{\dot{\varepsilon}}\right)^{\lambda}\right] \tag{8.25}$$

$$b = b_0 \left(\frac{k}{G}\right)^N \exp\left[-\left(\frac{Q}{RT}\right)\right] \tag{8.26}$$

$$\sigma_v = G \left(\frac{\dot{\varepsilon}}{a}\right)^{1/M} \tag{8.27}$$

$$a = a_0 \exp\left[-\left(\frac{Q^0}{RT}\right)\right] \tag{8.28}$$

where T is the absolute temperature (K) and R is the universal gas constant. The other constants are material parameters and they are determined from experiments. These parameters were determined by Cho *et al.* (2005), who developed a study about the modeling of strain hardening and texture evolution of the 304L stainless steel for FSW. The k_1 parameter is the maximum value of viscosity contribution for the stress flow. The saturation value of k_1 depends on temperature and strain rate; however, in the Hart's model it is replaced by the following equation given by (CHO *et al.*, 2005):

$$k_1 = \left(\frac{C}{\varphi} \right)^{m_0} \tag{8.29}$$

where the Fisher factor φ is given in Fisher (1966) as

$$\varphi = T.\ln \left(\frac{D_0}{\dot{\varepsilon}} \right) \tag{8.30}$$

Figure 8.3-b shows the viscosity profiles as a function of the strain rate and temperature for the AISI 304L stainless steel.

8.6   Results

In this work, a hybrid mesh composed of hexahedron and prism elements was used as shown in Figure 8.4. This mesh has 293,648 elements and 333,342 nodes. A mesh refinement study was performed and the mesh presented in Figure 8.4 provided results in terms of welding cycles independent of the grid size. Therefore, this grid was chosen for all simulations shown in this work.

Figure 8.4 – Mesh using in the simulation
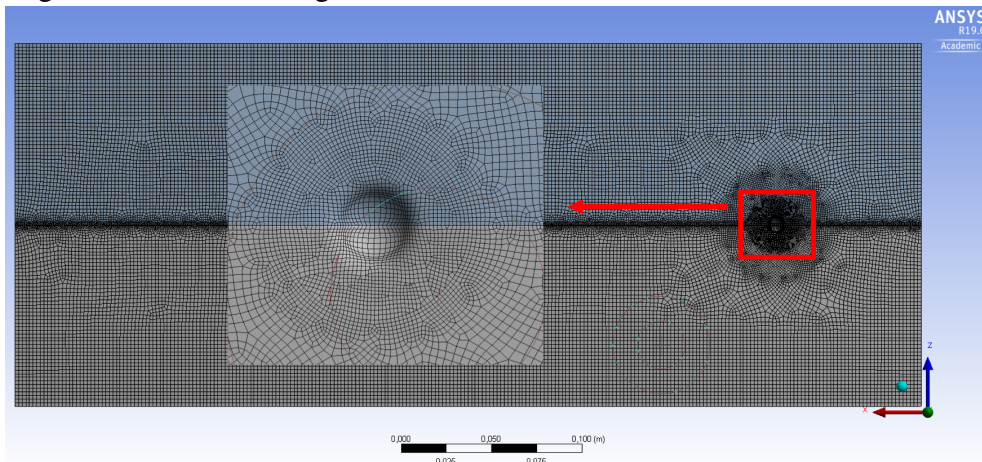
Source: The author

The welding cycles of Test 1 were compared with the experimental results measured by four thermocouples placed on the upper surface: two on each side (advancing side and retreating side). On each side, the thermocouples were positioned at a distance of 15 and 20 mm, respectively, from the center of the welding line. The diameter of the tool is 23.6 mm and, consequently the thermocouples are 3.2 and 8.2 mm from the edge of the shoulder, as shown in Figure 8.5.

Figure 8.5 – Position of the thermocouples
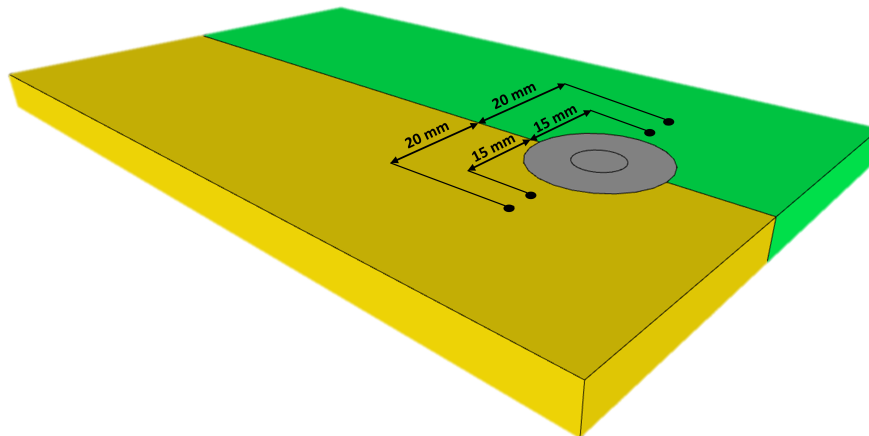
Source: The author

Figure 8.6, which presents the results for all positions mentioned above, shows that there is a good agreement between all the experimental and numerical cycles evaluated. Time, along the horizontal axis in Figure 8.6, was calculated by dividing each position along the length of the plate by the welding speed. The simulated results showed the same temperature peaks as the experimental results but a small difference in the base of the welding cycle. These results demonstrate that the heat input of the experimental and simulated results are similar.

Figure 8.6 – Comparison between experimental and simulated thermal cycle for Test 1 - 450 rpm and 40 kN.
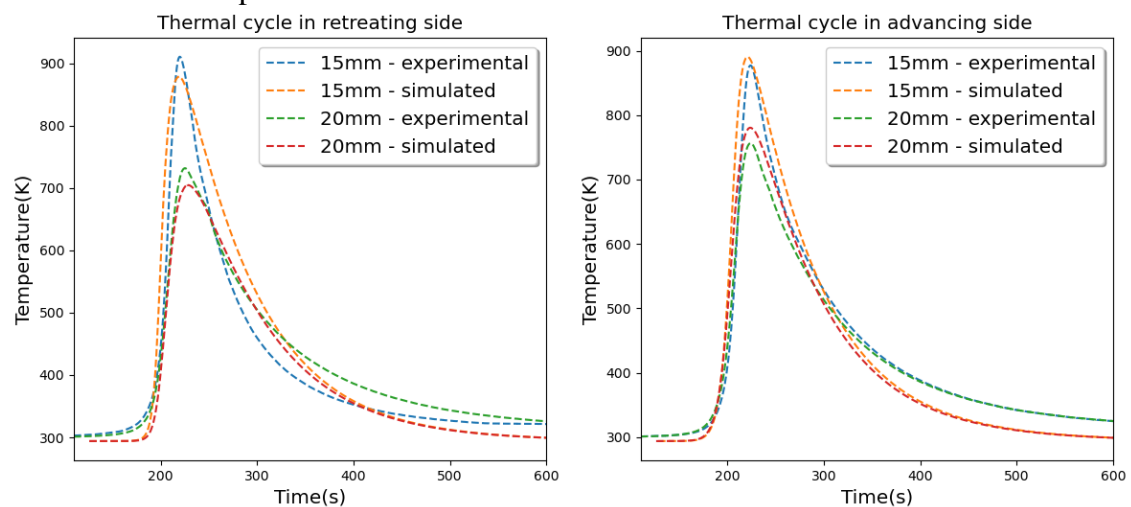
Source: The author

Temperature is an important factor that influences the results in welding. Figure 8.7 shows the cross section of the temperature field, for all tests, at the center of the pin and perpendicular to the welding velocity. As expected, the welding parameters directly influence the temperature. Figure 8.7 shows that the temperature increases when the axial force and rotation increase. Based on previous studies by the authors using similar welding procedures with these materials (SILVA *et al.*, 2020c) such behavior was expected because the friction coefficient and slip rate were kept constant during the simulation. In addition to the former effects, in dissimilar welding, the temperature is also influenced by the order in which the dissimilar materials are placed (retreating and advancing sides).

In addition to the natural asymmetry of the heat distribution that occurs between the advancing side and the retreating side, the asymmetry is accentuated by the use of different materials (SILVA *et al.*, 2020c; SILVA *et al.*, 2020b). All the tests presented in Figure 8.7 show an increase in temperature when the AISI 304L stainless steel was placed on the advancing side. This occurs because the AISI 304L stainless steel has greater strength than the AISI

410S stainless steel and, consequently the tool slides more easily when the AISI 304L stainless steel is placed on the advancing side because the AISI 304L steel has a higher flow resistance. Therefore, more heat is generated by the friction, which also increases the temperature of the surface (AL-BADOUR *et al.*, 2014).

Aval *et al.* (2011) welded the alloys AA5086 and AA6061 by FSW and these authors verified an increase in temperature when the material with greater resistance was placed on the advancing side. In the work published by Al-araji *et al.* (2011), the simulation showed the opposite behavior, but the authors attributed this difference to a limitation of the software that did not calculate the heat generated by the friction, which is the main factor responsible to increase the temperature when the position of the dissimilar materials are changed.

The results of Tests 1 through 4 (Figure 8.7-a, b, c and d) show that the temperature increased up to or higher than 80% of the melting point. However, these extremely high temperatures are not observed in practice during the FSW processes. These temperatures are consequence of a limitation of the model used here that assumes a constant friction coefficient. Further experiments to develop a variable friction coefficient function of temperature are still required. Although, this model predicted temperature levels outside the expected range for some rotations and axial forces, the model was successfully employed by Silva *et al.* (2020c) and Silva *et al.* (2020a) to predict defects such as flash formation and voids during the FSW of AISI 304L and 410S steels.

Based on simulations and experimental results, Silva *et al.* (2020c) observed that if the maximum temperature is above 80 % of the melting point or much lower than 80% of the melting point then drawbacks in the welded joint are expected. The ideal temperature for the FSW process is close to 80% of the melting point temperature of the metals being welded. The results of Tests 5 and 6 (Figure 8.7-e and f) present temperatures close to 80% of the melting point temperature, and they indicate better results with the lowest probability of flash formation.

Figure 8.7 –   Temperature cross section at the center of the pin. a) Test 1 - 450 rpm, 40 kN
with AISI 410S stainless steel on the advancing side, b) Test 2 - 450 rpm, 40
kN with AISI 304L stainless steel on the advancing side, c) Test 3 - 650 rpm,
40 kN with AISI 410S stainless steel on the advancing side, d) Test 4 - 650
rpm, 40 kN with AISI 304L stainless steel on the advancing side. e) Test 5 -
450 rpm, 30 kN with AISI 410S stainless steel on the advancing side, and f)
Test 6 - 450 rpm, 30 kN with AISI 304L stainless steel AISI on the advancing
side.
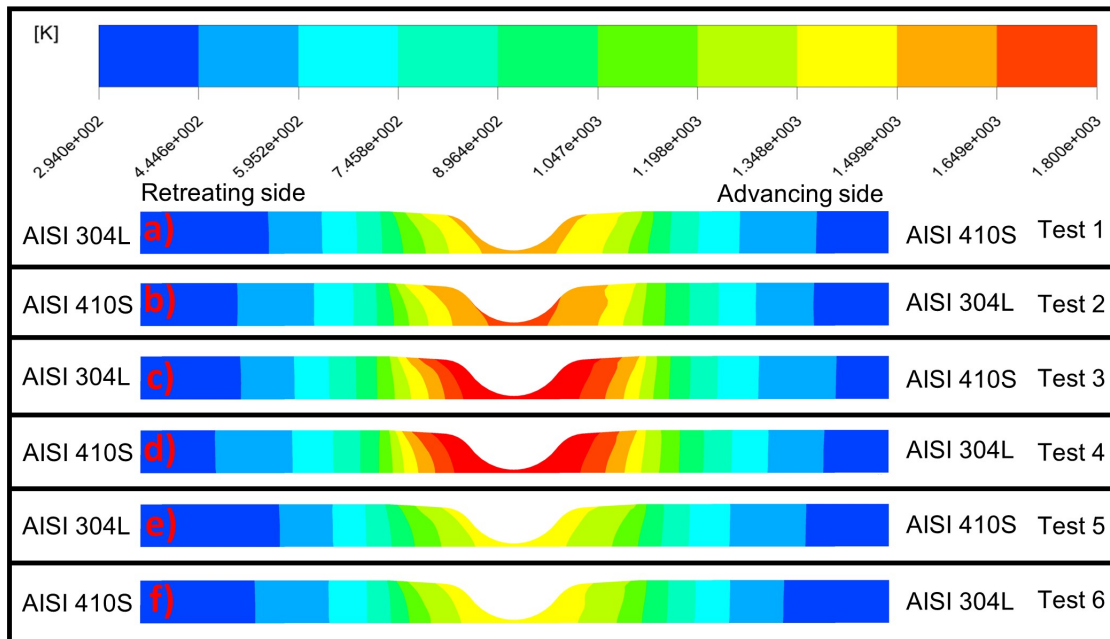
Source: The author

Figure 8.8 shows the cross section of the micrography results at the center of the
pin for Tests 1 and 5. The simulated temperature field for Test 1 (Figure 8.7-a) shows that the
maximum temperature was over 80% of the melting point (between 1499 k and 1649K), and
consequently flash formation is favored as shown (in the experimental results) in Figure 8.8-a.
However, Test 5 (Figure 8.8-b) shows a significant decrease in the number of flashes formed
compared to Figure 8.8-a (Test 1). These differences demonstrate that when the temperature is
greater than 80% of the melting point flashes are favored.

Figure 8.8 – Cross section of the micrography results at the center of the pin. a) Test 1, b) Test 5.
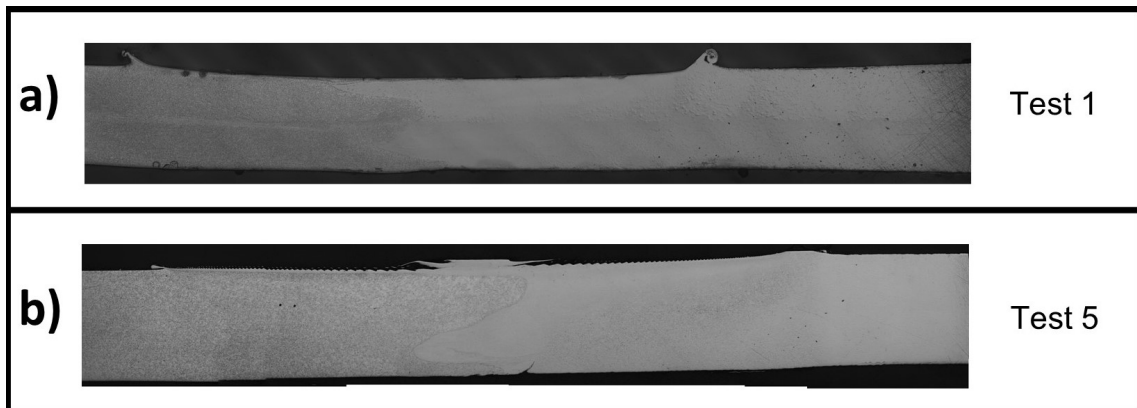
Source: The author

Figure 8.9 presents the cross section of the viscosity field at the center of the pin for all Tests investigated; the minimum viscosity found was $1.55 \cdot 10^4 kg/m.s$ and the maximum viscosity was defined in the code based on the analyze performed by Silva *et al.* (2020b). When the AISI 304L stainless steel is on the advancing side, the viscosity profile is less homogeneous, as confirmed in Figure 8.9-b and f. These figures show regions with higher viscosity (light blue regions) within the stir zone (dark blue region), as pointed out by the arrows. In Figure 8.9-d the change is not so evident, because the temperatures in these tests are considered too high for the parameters expected in FSW, which causes excessive softening of the entire simulated region.

As discussed below, the lack of homogeneity in the viscosity field can indicate an inefficient mixing of the different materials. The study developed by Chen *et al.* (2019) showed a similar behavior to those presented in Figure 8.9-a, d, and e, in which the low viscosity around the tool is homogeneous and represents the stir zone. In contrast, the lack of homogeneity in the stir zone is an indication that problems can be expected in the weld joint.

Inefficient mixing due to inversion of material sides has also been shown in the literature. Jafarzadegan *et al.* (2013) welded stainless steel 304 with st 37 steel with the latter, the low strength material, on the advancing side and they confirmed that the material flow was sufficient to fill up cavities and groove-like defects. This choice was based on the review carried out by Mishra e Ma (2005), whose work showed the need to position the less resistant material on the forward side. A similar situation occured in this study between 304L and 410S stainless steels.

Figure 8.9 – Cross section of the viscosity field in the middle of the pin. a) Test 1 - 450 rpm, 40 kN with AISI 410S stainless steel on the advancing side. b) Test 2 - 450 rpm, 40 kN with AISI 304L stainless steel on the advancing side. c) Test 3 - 650 rpm, 40 kN with AISI 410S stainless steel on the advancing side. d) Test 4 650 rpm, 40 kN with AISI 304L stainless steel on the advancing side. e) Test 5 - 450 rpm, 30 kN with AISI 410S stainless steel on the advancing side. f) Test 6 - 450 rpm, 30 kN with AISI 304L stainless steel on the advancing side
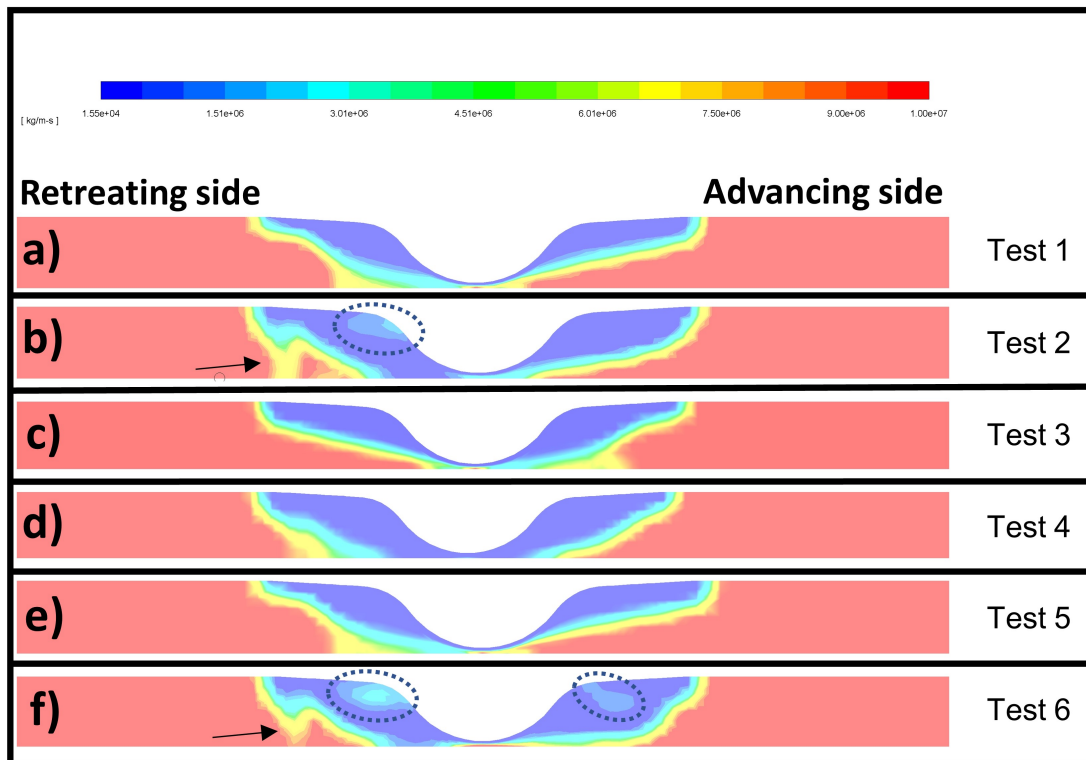
Source: The author

As the position of the material influences the final material in the weld region, a cross section of the phase fraction of the two dissimilar materials positioned at 60 cm after the tool is shown in Figure 8.10 for all tests.

Figures 8.10-b, d and f show that in all situations where the AISI 304L stainless steel was placed on the advancing side, the mixture had misshapen issues . However, when the AISI 410S stainless steel was placed on the advancing side, it showed a tendency of movement at the base and the AISI 304L steel showed a movement yield at the top, as shown in Figures 8.10-a, c and e.

Al-Badour *et al.* (2014) welded Al 6061 and Al 5083-O by the FSW process and found a similar behavior to that shown in Figure 8.10. The authors showed that when the most resistant material (Al 6061) was placed on the advancing side, the penetration into the other material was inefficient. In this study, when the 304L steel was placed on the advancing side, the

mixture did not present an efficient and homogeneous penetration (Figures 8.10-b, d, and f).

Figure 8.10 – Cross section of the phase fraction in the middle of the pin. The red color
represents 100% of the AISI 410S and the blue color represents 100% of
the AISI 304L steel. a) Test 1 - 450 rpm, 40 kN with AISI 410S stainless
steel on the advancing side, b) Test 2 - 450 rpm, 40 kN with AISI 304L
stainless steel on the advancing side, c) Test 3 - 650 rpm, 40 kN with AISI
410S stainless steel on the advancing side, d) Test 4 - 650 rpm, 40 kN with
AISI 304L stainless steel on the advancing side, e) Test 5 - 450 rpm, 30 kN
with AISI 410S stainless steel on the advancing side, and f) Test 6 - 450 rpm,
30 kN with AISI 304L stainless steel on the advancing side.
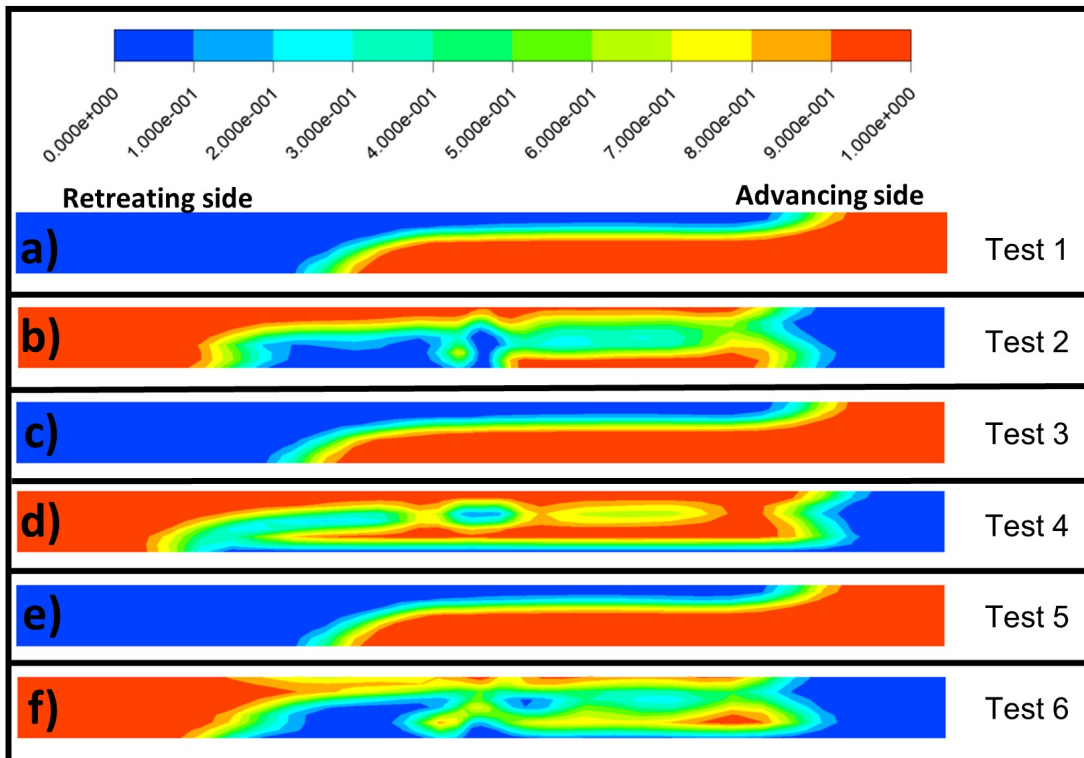
Source: The author

The behavior of the material flow observed above in the numerical simulation
presented in Figure 8.10 was compared to the experimental results in terms of macrography of
the welding region. The experimental results showed the same trend observed in the simulated
results. For instance, when the lowest-strength material was placed on the advancing side, the
AISI 410S tends to penetrate through the base and the material on the retreating side tends to
penetrate through the top, as seen in Figure 8.11.

Figure 8.11 – Welding macrography of Test 5.
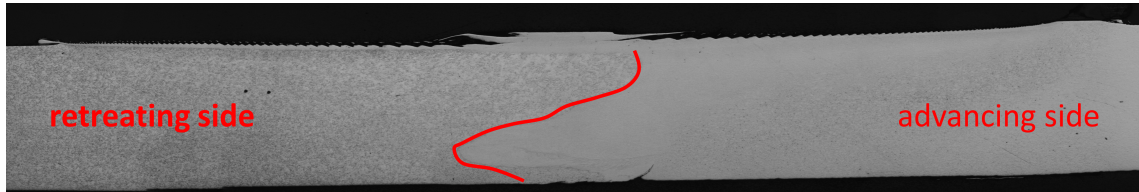
Source: The author

The above numerical results show that the simulation was able to predict which material should be placed on the retreating and advancing sides. Figure 8.12 compares the macrography results of Tests 5 and 6. Although the maximum temperature for Tests 5 and 6 presented above did not exceed 80% of the melting point, inverting the materials had a great impact on the result. Figure 8.12-b shows that when the AISI 304L stainless steel is placed on the advancing side several defects, such as flashes and voids are observed in the weld.

Figure 8.12 – Macrography results of Tests 5 and 6. (a) Experimental results with AISI 410S stainless steel on the advancing side and AISI 304L stainless steel on the retreating side (b) Experimental results with AISI 304L stainless steel on the advancing side and AISI 410S stainless steel on the retreating side
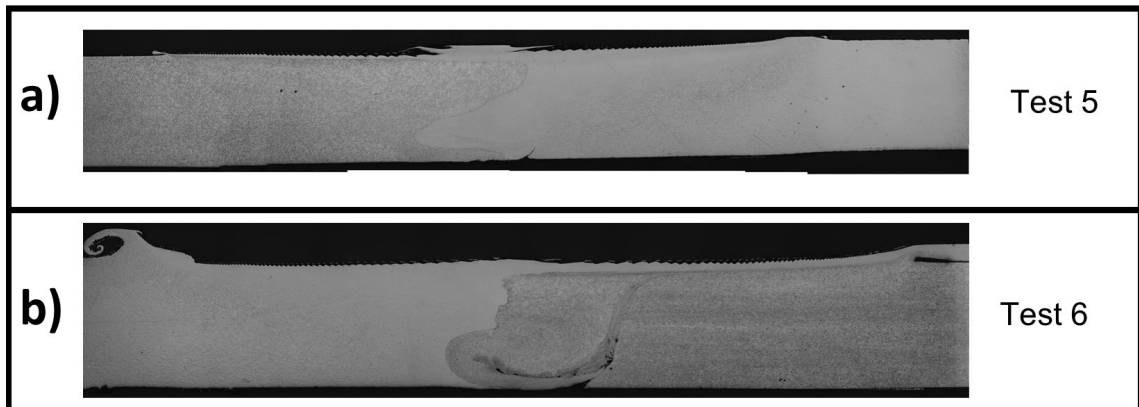
Source: The author

Figure 8.13 presents the macrography results of Test 1 as well as the simulated temperature, viscosity, and velocity fields. The low viscosity zone (Figure 8.13-c) demonstrates a similarity with the stir zone, represented by the black dotted line. The low viscosity zone has a small difference at the base of the pin and at the end of the shoulder. These differences are due to the limitations of the model, which does not consider the depression caused by the tool that extends the stir zone more than the simulation.

Another important aspect shown in Figure 8.13 is the transition between the zone with the smallest viscosity (dark blue region in Figure 8.13-c) and high viscosity (red region in Figure 8.13-c). This region of transition has reduced viscosity and zero velocity. This behavior

can be associated with the thermomechanically affected zone (TMAZ), in which the material is submitted to deformation and heating. However, this region is smaller than the stir zone. This deformation occurs in the transition between the intense movement present in the stir zone and the lack of movement in the heat affected zone (THREADGILL, 2007).

In addition to above commented zones, another region was observed, where the viscosity was not altered during the welding and did not present any speed, which is defined as the heat affected zone. Differing from the other regions, the microstructural changes results only from the temperature changes (region after blue dotted line).

Figure 8.13 – Macrography and simulated results of Test 1 with AISI 410S stainless steel on the advancing side. (a) Macrography (b) Temperature field (c) Viscosity field (d) Velocity field. * Black dotted line is the experimental stir zone and the blue dotted line is the end of thermomechanically affected zone.
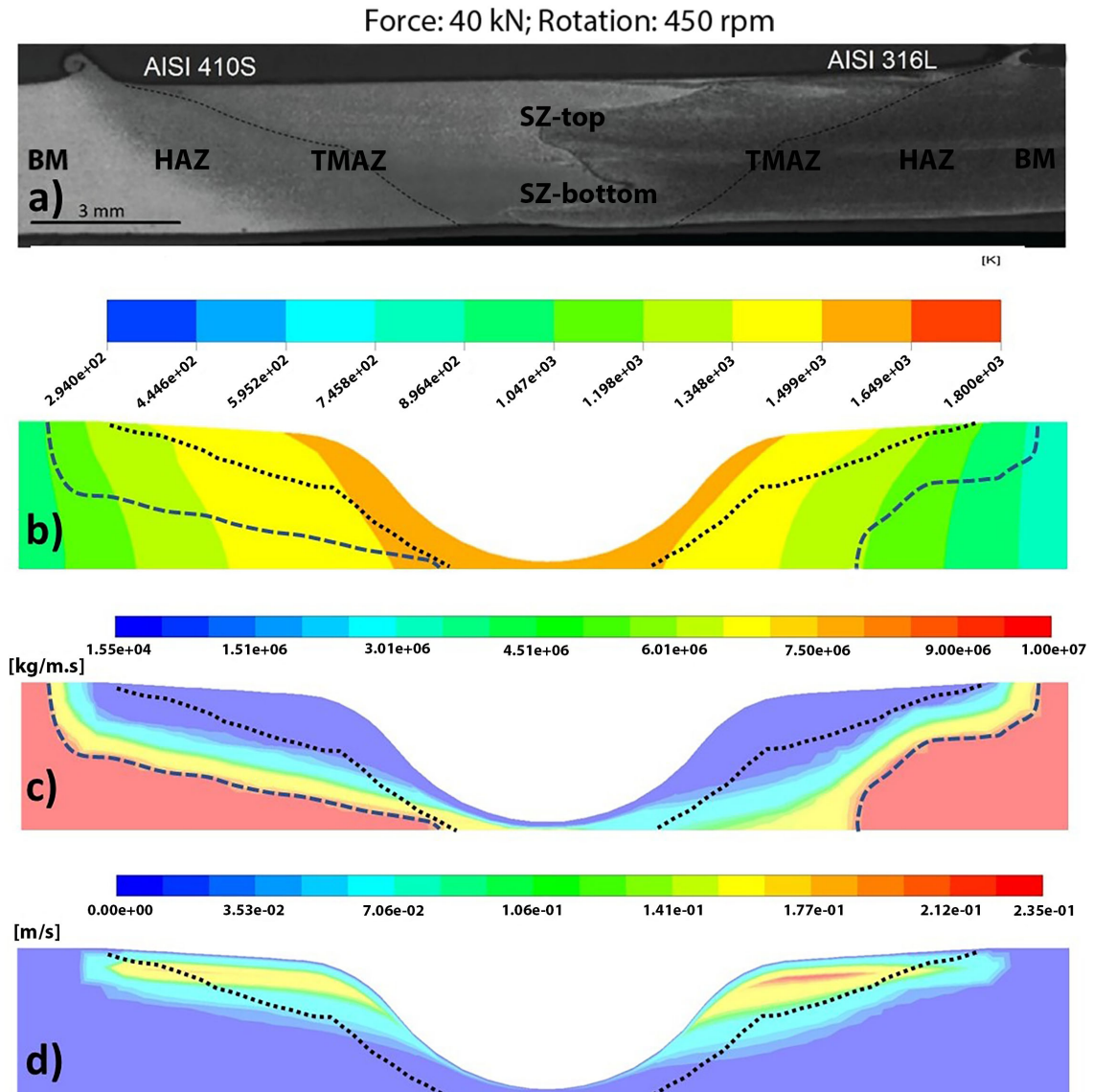
Source: The author

8.7   Conclusions

This work presented an experimental and numerical investigation of dissimilar joints of AISI 304L austenitic stainless steel with AISI 410S ferritic stainless steel using the FSW process. The equations of the model were discretized by the Finite Volume Method (FVM), and the mixing of the materials was modeled by the Volume of Fluid method (VOF) using the ANSYS-fluent simulator.

This investigation demonstrated that the temperatures predicted by the simulation were close to the experimental results. In addition, the temperature field can be used to predict possible defects when the simulated temperature reached values above 80 % of the melting point of the materials.

The viscosity of the mixing zone became heterogeneous, when the materials were positioned in an inappropriate order . A heterogeneity of the stir zone can cause material flow problems, which can give rise to voids and failures in the mixing of materials.

At extreme temperatures, the viscosity field was not able to detect problems in the stir zone, but the VOF method was efficient in predicting an inefficient mixing of the materials.

The combination of the speed, viscosity, and temperature analyzes resulted in excellent indications of the size of the thermomechanically-calibrated zone, stir zone and heat affected zone.

9 CONCLUSIONS

Based on the studies developed in this thesis it was possible to conclude.

- In the chapter 5, two viscosity models were analyzed for Ti-6Al-4V and 304. A methodology was developed to choose the maximum viscosity value to be defined. Results showed that it must be the first viscosity value in which it does not occur non-fluid movement. The values defined above or below changed the entire heat propagation profile in the material.

- The temperature results for AISI 304L and 410S stainless steels were compared with the thermocouple in different positions and all showed results close to the experimental.

- The simulated results for AISI 304L stainless steel made it possible to predict the conditions with the highest flash occurrence, using the parameter Y, that depend of rotation, minimum viscosity and axial pressure, developed in the article. The increase in the Y parameter indicated the increase in flashes in the analyzed conditions. Injecting a uniform layer particles before the tool of the fluid model it was possible to determine the conditions most likely to form wormholes, because after tool was observed regions where there was not particles

- Combining the temperature results of 410S steel with thermodynamic simulations, it was possible to predict the phases formed in the studied conditions. In all conditions, the formation of chromium carbides ($Cr_{23}C_6$) and austentic was observed. Analyzing the cooling speed of the simulations, it was possible to conclude that in all regions where the austenite temperature was reached, martensite formation occurs.

- The Y parameter developed in the study of AISI 304L stainless steel was applied to AISI 410S stainless steel and also in predicted the conditions with the greatest possibility of flash formation.

- The VOF method was effective in simulating the mixture of the two materials during dissimilar welding, which made it possible to predict the best position of each material during welding, in addition to accurately predicting the temperatures resulting from the interaction of the two different materials.

BIBLIOGRAPHY

ABDOLLAH-ZADEH, A.; EGHBALI, B. Mechanism of ferrite grain refinement during warm deformation of a low carbon Nb-microalloyed steel. **Materials Science and Engineering A**, v. 457, n. 1-2, p. 219–225, 2007. ISSN 09215093.

AGUILAR, S.; TABARES, R.; SERNA, C. Microstructural Transformations of Dissimilar Austenite-Ferrite Stainless Steels Welded Joints. **Journal of Materials Physics and Chemistry**, v. 1, n. 4, p. 65–68, 2013. ISSN 2333-4436.

AL-ARAJI, N. M.; KADUM, K. M.; AL-DAYNI, A. A. Effect of friction stir welding pressure on the microstructure and mechanical properties of weld joints. **International Journal of Scientific & Engineering Research**, v. 2, n. 12, p. 1–5, 2011.

AL-BADOUR, F.; MERAH, N.; SHUAIB, A.; BAZOUNE, A. Thermo-mechanical finite element model of friction stir welding of dissimilar alloys. **International Journal of Advanced Manufacturing Technology**, v. 72, n. 5-8, p. 607–617, 2014. ISSN 14333015.

ALIZADEH-SH, M.; MARASHI, S. P.; POURANVARI, M. Resistance spot welding of AISI 430 ferritic stainless steel: Phase transformations and mechanical properties. **Materials and Design**, Elsevier Ltd, v. 56, p. 258–263, 2014. ISSN 18734197. Disponível em: <http://dx.doi.org/10.1016/j.matdes.2013.11.022>.

ALMOUSSAWI, M.; SMITH, A. J. Thermo-Mechanical Effect on Poly Crystalline Boron Nitride Tool Life During Friction Stir Welding (Dwell Period). **Metals and Materials International**, The Korean Institute of Metals and Materials, v. 24, n. 3, p. 560–575, 2018. ISSN 20054149.

AMUDA, M.; AKINLABI, E.; MRIDHA, S. **Ferritic Stainless Steels: Metallurgy, Application and Weldability**. [S.l.]: Elsevier Ltd., 2016. 1–18 p. ISBN 9780128035818.

ANAMAN, S. Y.; CHO, H. H.; DAS, H.; LEE, J. S.; HONG, S. T. Microstructure and mechanical/electrochemical properties of friction stir butt welded joint of dissimilar aluminum and steel alloys. **Materials Characterization**, Elsevier, v. 154, n. April, p. 67–79, 2019. ISSN 10445803.

ANDERSSON, J. O.; HELANDER, T.; HÖGLUND, L.; SHI, P.; SUNDMAN, B. Thermo-Calc & DICTRA, computational tools for materials science. **Calphad: Computer Coupling of Phase Diagrams and Thermochemistry**, v. 26, n. 2, p. 273–312, 2002. ISSN 03645916.

ANDRADE, T. C.; SILVA, C. C.; MIRANDA, H. C. de; MOTTA, M. F.; FARIAS, J. P.; BERGMAN, L. A.; SANTOS, J. F. dos. Microestrutura de uma solda dissimilar entre o aço inoxidável ferrítico AISI 410S e o aço inoxidável austenítico AISI 304L soldado pelo processo FSW. **Rev. Soldag. Insp.**, v. 20, n. 4, p. 467–478, 2015. ISSN 19806973.

ANSYS. **Volume Fraction Equation**. 2009. Disponível em: <http://www.afs.enea.it/project/neptunius/docs/fluent/html/th/node299.htm>.

ANTUNES, P. D.; CORREA, E. O.; BARBOSA, R. P.; SILVA, E. M.; PADILHA, A. F.; GUIMARAES, P. M. Effect of weld metal chemistry on stress corrosion cracking behavior of AISI 444 ferritic stainless steel weldments in boiling chloride solution. **Materials and Corrosion**, v. 64, n. 5, p. 415–421, 2013. ISSN 09475117.

ARBEGAST, W. J. A flow-partitioned deformation zone model for defect formation during friction stir welding. **Scripta Materialia**, v. 58, n. 5, p. 372–376, 2008. ISSN 13596462.

AVAL, H. J.; SERAJZADEH, S.; KOKABI, A. H. Evolution of microstructures and mechanical properties in similar and dissimilar friction stir welding of AA5086 and AA6061. **Materials Science and Engineering A**, Elsevier B.V., v. 528, n. 28, p. 8071–8083, 2011. ISSN 09215093. Disponível em: <http://dx.doi.org/10.1016/j.msea.2011.07.056>.

BALASUBRAMANIAN, V.; SHANMUGAM, K.; LAKSHMINARAYANAN, A. K. Effect of autogenous arc welding processes on fatigue crack growth behaviour of ferritic stainless steel joints. **ISIJ International**, v. 48, n. 4, p. 489–495, 2008. ISSN 09151559.

BATISTÃO, B. F.; BERGMANN, L. A.; GARGARELLA, P.; ALCÂNTARA, N. G. d.; SANTOS, J. F. dos; KLUSEMANN, B. Characterization of dissimilar friction stir welded lap joints of AA5083 and GL D36 steel. **Journal of Materials Research and Technology**, v. 9, n. 6, p. 15132–15142, 2020. ISSN 22387854.

BELADI, H.; KELLY, G. L.; HODGSON, P. D. Ultrafine grained structure formation in steels using dynamic strain induced transformation processing. **International Materials Reviews**, v. 52, n. 1, p. 14–28, 2007. ISSN 09506608.

BILGIN, M. B.; MERAN, C. The effect of tool rotational and traverse speed on friction stir weldability of AISI 430 ferritic stainless steels. **Materials and Design**, Elsevier Ltd, v. 33, n. 1, p. 376–383, 2012. ISSN 02641275. Disponível em: <http://dx.doi.org/10.1016/j.matdes.2011.04.013>.

BOND, A. P.; LIZLOVS, E. A. Intergranular Corrosion of Ferritic Stainless Steels. **Journal of The Electrochemical Society**, The Electrochemical Society, v. 116, n. 9, p. 1305, 1969. ISSN 00134651.

CAETANO, G.; MOTTA, M.; MIRANDA, H.; FARIAS, J.; BERGMANN, L.; SANTOS, J. dos; SILVA, C. Assessment of Joint Configuration and Welding Parameters for the dissimilar joining of AISI 304L and AISI 410S stainless steels by the Friction Stir Welding. **Submitted to J Mater Process Technol**, 2021.

CAETANO, G. d. Q. **Avaliação da Determinação do Grau de Sensitização de Componentes Soldados e Não Soldados Utilizando uma Célula Eletroquímica Portátil.** Fortaleza: [s.n.], 2012. 1 - 67 p.

CAETANO, G. d. Q.; SILVA, C. C.; MOTTA, M. F.; MIRANDA, H. C.; FARIAS, J. P.; BERGMANN, L. A.; SANTOS, J. F. dos. Influence of rotation speed and axial force on the friction stir welding of AISI 410S ferritic stainless steel. **Journal of Materials Processing Technology**, Elsevier B.V., v. 262, p. 430–436, 2018. ISSN 09240136.

CAETANO, G. D. Q.; SILVA, C. C.; MOTTA, M. F.; MIRANDA, H. C.; FARIAS, J. P.; BERGMANN, L. A.; SANTOS, J. F. Intergranular corrosion evaluation of friction stir welded AISI 410S ferritic stainless steel. **Journal of Materials Research and Technology**, Brazilian Metallurgical, Materials and Mining Association, v. 8, n. 2, p. 1878–1887, 2019. ISSN 22387854.

CAETANO, G. Q. **Soldagem similar de aços inoxidáveis ferríticos e austeníticos pelo processo "friction stir welding" (Joining of similar ferritic and austenitic stainless steels**

by the "friction stir welding" process). Tese (Doutorado) — Universidade Federal do Ceará, Campus do Pici - Bloco 729 CEP 60.440-554 - Fortaleza - CE, 2016.

CHANG, C. I.; LEE, C. J.; HUANG, J. C. Relationship between grain size and Zener-Holloman parameter during friction stir processing in AZ31 Mg alloys. **Scripta Materialia**, v. 51, n. 6, p. 509–514, 2004. ISSN 13596462.

CHEN, G.; WANG, G.; SHI, Q.; ZHAO, Y.; HAO, Y.; ZHANG, S. Three-dimensional thermal-mechanical analysis of retractable pin tool friction stir welding process. **Journal of Manufacturing Processes**, Elsevier, v. 41, n. March, p. 1–9, 2019. ISSN 15266125.

CHO, H. H.; HAN, H. N.; HONG, S. T.; PARK, J. H.; KWON, Y. J.; KIM, S. H.; STEEL, R. J. Microstructural analysis of friction stir welded ferritic stainless steel. **Materials Science and Engineering A**, Elsevier B.V., v. 528, n. 6, p. 2889–2894, 2011. ISSN 09215093.

CHO, H. H.; HONG, S. T.; ROH, J. H.; CHOI, H. S.; KANG, S. H.; STEEL, R. J.; HAN, H. N. Three-dimensional numerical and experimental investigation on friction stir welding processes of ferritic stainless steel. **Acta Materialia**, v. 61, n. 7, p. 2649–2661, 2013. ISSN 13596454.

CHO, J. H.; BOYCE, D. E.; DAWSON, P. R. Modeling strain hardening and texture evolution in friction stir welding of stainless steel. **Materials Science and Engineering A**, v. 398, n. 1-2, p. 146–163, 2005. ISSN 09215093.

COSTA, A. L. V. da; MEI, P. R.; others. **Aços e ligas especiais**. [S.l.]: Editora Blucher, 2010. 664 p. ISBN 9788521205180.

DAK, G.; PANDEY, C. A critical review on dissimilar welds joint between martensitic and austenitic steel for power plant application. **Journal of Manufacturing Processes**, Elsevier, v. 58, n. August, p. 377–406, 2020. ISSN 15266125.

DAYAL, R. K.; PARVATHAVARTHINI, N.; RAJ, B. Influence of metallurgical variables on sensitisation kinetics in austenitic stainless steels. **International Materials Reviews**, v. 50, n. 3, p. 129–155, 2005. ISSN 09506608.

DEHGHAN-MANSHADI, A.; HODGSON, P. D. Effect of δ-ferrite co-existence on hot deformation and recrystallization of austenite. **Journal of Materials Science**, v. 43, n. 18, p. 6272–6277, 2008. ISSN 00222461.

DELEU, E.; DHOOGE, A.; TABAN, E.; KALUÇ, E. Possibilities and limitations to improve the weldability of low carbon 12Cr Ferritic stainless steel for expanded industrial applications. **Welding in the World**, v. 53, n. 9-10, 2009. ISSN 00432288.

DENG, Z.; LOVELL, M. R.; TAGAVI, K. A. Influence of Material Properties and Forming Velocity on the Interfacial Slip Characteristics of Cross Wedge Rolling. **Journal of Manufacturing Science and Engineering**, v. 123, n. 4, p. 647, 2001. ISSN 10871357. Disponível em: <http://manufacturingscience.asmedigitalcollection.asme.org/article.aspx?articleid=1484966>.

DERAZKOLA, H. A.; EYVAZIAN, A.; SIMCHI, A. Submerged friction stir welding of dissimilar joints between an Al-Mg alloy and low carbon steel: Thermo-mechanical modeling, microstructural features, and mechanical properties. **Journal of Manufacturing Processes**, Elsevier, v. 50, n. November 2019, p. 68–79, 2020. ISSN 15266125. Disponível em: <https://doi.org/10.1016/j.jmapro.2019.12.035>.

DERAZKOLA, H. A.; SIMCHI, A. An investigation on the dissimilar friction stir welding of T-joints between AA5754 aluminum alloy and poly(methyl methacrylate). **Thin-Walled Structures**, Elsevier Ltd, v. 135, n. September 2018, p. 376–384, 2 2019. ISSN 02638231. Disponível em: <https://doi.org/10.1016/j.tws.2018.11.027https://linkinghub.elsevier.com/retrieve/pii/S0263823118311200>.

DEVINE, T. M.; RITTER, A. M. Sensitization of 12 Wt Pct chromium, titanium-stabilized ferritic stainless steel. **Metallurgical Transactions A**, v. 14, n. 8, p. 1721–1728, 1983. ISSN 1543-1940.

EMAMI, S.; SAEID, T. A comparative study on the microstructure development of friction stir welded 304 austenitic, 430 ferritic, and 2205 duplex stainless steels. **Materials Chemistry and Physics**, Elsevier B.V., v. 237, n. July, p. 121833, 2019. ISSN 02540584.

EYVAZIAN, A.; HAMOUDA, A.; TARLOCHAN, F.; DERAZKOLA, H. A.; KHOD-ABAKHSHI, F. Simulation and experimental study of underwater dissimilar friction-stir welding between aluminium and steel. **Journal of Materials Research and Technology**, Korea Institute of Oriental Medicine, v. 9, n. 3, p. 3767–3781, 2020. ISSN 22387854. Disponível em: <https://doi.org/10.1016/j.jmrt.2020.02.003>.

FANG, Y.; JIANG, X.; MO, D.; ZHU, D.; LUO, Z. A review on dissimilar metals' welding methods and mechanisms with interlayer. **International Journal of Advanced Manufacturing Technology**, The International Journal of Advanced Manufacturing Technology, v. 102, n. 9-12, p. 2845–2863, 2019. ISSN 14333015.

FERREIRA, A. C.; CAMPANELLI, L. C.; SUHUDDIN, U. F. H.; ALCÂNTARA, N. G. de; SANTOS, J. F. dos. Correction to: Investigation of internal defects and premature fracture of dissimilar refill friction stir spot welds of AA5754 and AA6061 (The International Journal of Advanced Manufacturing Technology, (2020), 106, 7-8, (3523-3531), 10.1007/s00170-019-0. **International Journal of Advanced Manufacturing Technology**, The International Journal of Advanced Manufacturing Technology, v. 110, n. 5-6, p. 1677, 2020. ISSN 14333015.

FISHER, E. S. Temperature dependence of the elastic moduli in alpha uranium single crystals, part iv ($298°$ to $923°$ K). **Journal of Nuclear Materials**, v. 18, n. 1, p. 39–54, 1966. ISSN 00223115.

FOLKHARD, E. **Welding Metallurgy of Stainless Steels**. Vienna: Springer Vienna, 1988. v. 53. 1689–1699 p. ISSN 1098-6596. ISBN 978-3-7091-8967-2. Disponível em: <http://link.springer.com/10.1007/978-3-7091-8965-8>.

FRIGAARD, .; GRONG, .; MIDLING, O. T. A process model for friction stir welding of age hardening aluminum alloys. **Metallurgical and Materials Transactions A**, v. 32, n. 5, p. 1189–1200, 2001. ISSN 1073-5623. Disponível em: <http://link.springer.com/10.1007/s11661-001-0128-4>.

GADAKH, V. S.; KUMAR, A. FSW tool design using TRIZ and parameter optimization using Grey Relational Analysis. **Materials Today: Proceedings**, Elsevier Ltd, v. 5, n. 2, p. 6655–6664, 2018. ISSN 22147853. Disponível em: <https://doi.org/10.1016/j.matpr.2017.11.322>.

GIBSON, B. T.; LAMMLEIN, D. H.; PRATER, T. J.; LONGHURST, W. R.; COX, C. D.; BALLUN, M. C.; DHARMARAJ, K. J.; COOK, G. E.; STRAUSS, A. M. Friction stir welding: Process, automation, and control. **Journal of Manufacturing Processes**, The Society of Manufacturing Engineers, v. 16, n. 1, p. 56–73, 2014. ISSN 15266125.

GULLINO, A.; MATTEIS, P.; AIUTO, F. D. Review of aluminum-to-steel welding technologies for car-body applications. **Metals**, v. 9, n. 3, p. 1–28, 2019. ISSN 20754701.

HART, E. W. Constitutive Relations for the Nonelastic Deformation of Metals. **Journal of Engineering Materials and Technology**, AIP, v. 98, n. 3, p. 193, 1976. ISSN 00944289. Disponível em: <http://aip.scitation.org/doi/abs/10.1063/1.46201http://materialstechnology.asmedigitalcollection.asme.org/article.aspx?articleid=1422121>.

HATTEL, J.; SCHMIDT, H.; TUTUM, C. Thermomechanical modelling of friction stir welding. In: DAVID, S.; DEBROY, T.; DUPONT, J.; KOSEKI, T.; SMARTT, H. (Ed.). **Thermomechanical Modelling of Friction Stir Welding**. United States: ASM International, 2009. p. 1–10. Trends in Welding Research: 8th International Conference ; Conference date: 01-06-2008 Through 06-06-2008.

HE, X.; GU, F.; BALL, A. A review of numerical analysis of friction stir welding. **Progress in Materials Science**, Elsevier Ltd, v. 65, p. 1–66, 2014. ISSN 00796425.

HERNÁNDEZ, C. A.; FERRER, V. H.; MANCILLA, J. E.; MARTÍNEZ, L. C. Three-dimensional numerical modeling of the friction stir welding of dissimilar steels. **International Journal of Advanced Manufacturing Technology**, v. 93, n. 5-8, p. 1567–1581, 2017. ISSN 14333015.

HIRT, C.; NICHOLS, B. Volume of fluid (VOF) method for the dynamics of free boundaries. **Journal of Computational Physics**, v. 39, n. 1, p. 201–225, 1 1981. ISSN 00219991. Disponível em: <http://link.springer.com/10.1007/s40998-018-0069-1https://linkinghub.elsevier.com/retrieve/pii/0021999181901455>.

HOSSEINI, H. S.; SHAMANIAN, M.; KERMANPUR, A. Characterization of microstructures and mechanical properties of Inconel 617/310 stainless steel dissimilar welds. **Materials Characterization**, Elsevier Inc., v. 62, n. 4, p. 425–431, 2011. ISSN 10445803. Disponível em: <http://dx.doi.org/10.1016/j.matchar.2011.02.003>.

HOU, X.; YANG, X.; CUI, L.; ZHOU, G. Influences of joint geometry on defects and mechanical properties of friction stir welded AA6061-T4 T-joints. **Materials and Design**, Elsevier Ltd, v. 53, p. 106–117, 2014. ISSN 18734197.

HU, J. c.; SONG, H. m.; YU, M.; JIANG, L. z. Thermo-Calc Calculation and Experimental Study of Microstructure of SUS 410S and SUS 430 Ferrite Stainless Steels at High Temperature. **Journal of Iron and Steel Research International**, v. 14, n. 5 SUPPL. 1, p. 183–188, 2007. ISSN 1006706X.

JAFARZADEGAN, M.; ABDOLLAH-ZADEH, A.; FENG, A. H.; SAEID, T.; SHEN, J.; ASSADI, H. Microstructure and Mechanical Properties of a Dissimilar Friction Stir Weld between Austenitic Stainless Steel and Low Carbon Steel. **Journal of Materials Science and Technology**, Elsevier Ltd, v. 29, n. 4, p. 367–372, 2013. ISSN 10050302. Disponível em: <http://dx.doi.org/10.1016/j.jmst.2013.02.008>.

KAH, P.; RAJAN, R.; MARTIKAINEN, J.; SUORANTA, R. **Investigation of weld defects in friction-stir welding and fusion welding of aluminium alloys**. [S.l.]: International Journal of Mechanical and Materials Engineering, 2015.

KAINUMA, S.; KATSUKI, H.; IWAI, I.; KUMAGAI, M. Evaluation of fatigue strength of friction stir butt-welded aluminum alloy joints inclined to applied cyclic stress. **International Journal of Fatigue**, v. 30, n. 5, p. 870–876, 2008. ISSN 01421123.

KHAN, N. Z.; SIDDIQUEE, A. N.; KHAN, Z. A.; SHIHAB, S. K. Investigations on tunneling and kissing bond defects in FSW joints for dissimilar aluminum alloys. **Journal of Alloys and Compounds**, Elsevier B.V, v. 648, p. 360–367, 2015. ISSN 09258388. Disponível em: <http://dx.doi.org/10.1016/j.jallcom.2015.06.246>.

KIM, J. K.; LEE, B. J.; LEE, B. H.; KIM, Y. H.; KIM, K. Y. Intergranular segregation of Cr in Ti-stabilized low-Cr ferritic stainless steel. **Scripta Materialia**, Acta Materialia Inc., v. 61, n. 12, p. 1133–1136, 2009. ISSN 13596462.

KIM, S. D.; YOON, J. Y.; NA, S. J. A study on the characteristics of FSW tool shapes based on CFD analysis. **Welding in the World**, Welding in the World, v. 61, n. 5, p. 915–926, 2017. ISSN 00432288.

KIM, S. I.; YOO, Y. C. Continuous dynamic recrystallization of AISI 430 ferritic stainless steel. **Metals and Materials International**, v. 8, n. 1, p. 7–13, 2002. ISSN 12259438.

KIM, Y. G.; FUJII, H.; TSUMURA, T.; KOMAZAKI, T.; NAKATA, K. Three defect types in friction stir welding of aluminum die casting alloy. **Materials Science and Engineering A**, v. 415, n. 1-2, p. 250–254, 2006. ISSN 09215093.

KNUTSEN, R. D.; BALL, A. Influence of inclusions on the corrosion behavior of a 12 wt% chromium steel. **Corrosion**, v. 47, n. 5, p. 359–368, 1991. ISSN 00109312.

KOKAWA, H.; PARK, S. H.; SATO, Y. S.; OKAMOTO, K.; HIRANO, S.; INAGAKI, M. Microstructures in friction stir welded 304 austenitic stainless steel. **Welding in the World**, v. 49, n. 3-4, p. 34–40, 2005. ISSN 00432288.

KONG, H. S.; ASHBY, M. F. Friction-Heating Maps and Their Applications. **MRS Bulletin**, v. 16, n. 10, p. 41–48, 1991. ISSN 19381425.

KUMAR, K.; KAILAS, S. V.; SRIVATSAN, T. S. Influence of Tool Geometry in Friction Stir Welding. **Materials and Manufacturing Processes**, v. 23, n. 2, p. 188–194, 1 2008. ISSN 1042-6914. Disponível em: <http://www.tandfonline.com/doi/abs/10.1080/10426910701774734>.

KUZUCU, V.; AKSOY, M.; KORKUT, M.; YILDIRIM, M. The effect of niobium on the microstructure of ferritic stainless steel. **Materials Science and Engineering: A**, v. 230, n. 1-2, p. 75–80, 7 1997. ISSN 09215093. Disponível em: <http://journals.sagepub.com/doi/10.1243/13506501JET401https://linkinghub.elsevier.com/retrieve/pii/S0921509397000105>.

KWON, Y. J.; SHIGEMATSU, I.; SAITO, N. Dissimilar friction stir welding between magnesium and aluminum alloys. **Materials Letters**, v. 62, n. 23, p. 3827–3829, 2008. ISSN 0167577X.

LAKSHMINARAYANAN, A. K.; BALASUBRAMANIAN, V. An assessment of microstructure, hardness, tensile and impact strength of friction stir welded ferritic stainless steel joints. **Materials and Design**, Elsevier Ltd, v. 31, n. 10, p. 4592–4600, 2010. ISSN 02641275.

LAKSHMINARAYANAN, A. K.; BALASUBRAMANIAN, V. Assessment of fatigue life and crack growth resistance of friction stir welded AISI 409M ferritic stainless steel joints. **Materials Science and Engineering A**, Elsevier B.V., v. 539, p. 143–153, 2012. ISSN 09215093.

LAKSHMINARAYANAN, A. K.; SHANMUGAM, K.; BALASUBRAMANIAN, V. Effect of Autogenous Arc Welding Processes on Tensile and Impact Properties of Ferritic Stainless Steel Joints. **Journal of Iron and Steel Research International**, Central Iron and Steel Research Institute, v. 16, n. 1, p. 62–68, 2009. ISSN 1006706X.

LEE, S.; KWON, D.; LEE, Y. K.; KWON, O. Transformation strengthening by thermomechanical treatments in C-Mn-Ni-Nb steels. **Metallurgical and Materials Transactions A**, v. 26, n. 5, p. 1093–1100, 1995. ISSN 10735623.

LI, B.; SHEN, Y.; HU, W. The study on defects in aluminum 2219-T6 thick butt friction stir welds with the application of multiple non-destructive testing methods. **Materials and Design**, v. 32, n. 4, p. 2073–2084, 2011. ISSN 02641275.

LIPPOLD, J.; KOTECKI, D. **Welding Metallurgy and Weldability of Stainless Steels**. 1. ed. [S.l.]: Wiley, 2005. 376 p. ISBN 0471473790, 9780471473794.

LOMOLINO, S.; TOVO, R.; SANTOS, J. D. On the fatigue behaviour and design curves of friction stir butt-welded Al alloys. **International Journal of Fatigue**, v. 27, n. 3, p. 305–316, 2005. ISSN 01421123.

MA, Z. Y.; FENG, A. H.; CHEN, D. L.; SHEN, J. Recent Advances in Friction Stir Welding/Processing of Aluminum Alloys: Microstructural Evolution and Mechanical Properties. **Critical Reviews in Solid State and Materials Sciences**, v. 43, n. 4, p. 269–333, 2018. ISSN 15476561.

MARCHATTIWAR, A.; SARKAR, A.; CHAKRAVARTTY, J. K.; KASHYAP, B. P. Dynamic recrystallization during hot deformation of 304 austenitic stainless steel. **Journal of Materials Engineering and Performance**, v. 22, n. 8, p. 2168–2175, 2013. ISSN 10599495.

MENG, X.; HUANG, Y.; CAO, J.; SHEN, J.; SANTOS, J. F. dos. Recent progress on control strategies for inherent issues in friction stir welding. **Progress in Materials Science**, v. 115, n. June 2020, 2021. ISSN 00796425.

MEYER, A. M.; TOIT, M. D. The influence of interstitial diffusion across the fusion line on the haz microstructure and properties in 12% chromium type 1.4003 steels. **Welding in the World**, v. 52, n. 11-12, p. 42–49, 2008. ISSN 00432288.

MEYGHANI, B.; AWANG, M.; WU, C. Finite element modeling of friction stir welding (FSW) on a complex curved plate. **Journal of Advanced Joining Processes**, v. 1, n. January, p. 100007, 2020. ISSN 26663309.

MISHRA, A. **Friction Stir Welding Of Dissimilar Metal: A Review Study on corrosion resistance of Friction stir welded similar joints of Aluminium alloy.** Tese (Doutorado), 2018. Disponível em: <https://www.researchgate.net/publication/322551618>.

MISHRA, A. K.; SHOESMITH, D. W. Effect of Alloying Elements on Crevice Corrosion Inhibition of Nickel-Chromium-Molybdenum-Tungsten Alloys Under Aggressive Conditions: An Electrochemical Study. **Corrosion**, v. 70, n. 7, p. 721–730, 2014. ISSN 0010-9312.

MISHRA, R.; MA, Z. Friction stir welding and processing. **Materials Science and Engineering: R: Reports**, v. 50, n. 1-2, p. 1–78, 8 2005. ISSN 0927796X. Disponível em: <https://linkinghub.elsevier.com/retrieve/pii/S0927796X05000768>.

MOLA, J.; COOMAN, B. C. D. Quenching and partitioning processing of transformable ferritic stainless steels. **Scripta Materialia**, Acta Materialia Inc., v. 65, n. 9, p. 834–837, 2011. ISSN 13596462.

NANDAN, R.; DEBROY, T.; BHADESHIA, H. Recent advances in friction-stir welding – Process, weldment structure and properties. **Progress in Materials Science**, v. 53, n. 6, p. 980–1023, 2008. ISSN 0079-6425.

NANDAN, R.; LIENERT, T. J.; DEBROY, T. Toward reliable calculations of heat and plastic flow during friction stir welding of Ti-6Al-4V alloy. **International Journal of Materials Research**, v. 99, n. 4, p. 434–444, 4 2008. ISSN 1862-5282.

NANDAN, R.; ROY, G. G.; DEBROY, T. Numerical Simulation of Three-Dimensional Heat Transfer and Plastic Flow During Friction Stir Welding. **Metallurgical and Materials Transactions**, v. 37A, n. 4, p. 1247–1259, 2006. ISSN 1073-5623.

NANDAN, R.; ROY, G. G.; LIENERT, T. J.; DEBROY, T. Numerical modelling of 3D plastic flow and heat transfer during friction stir welding of stainless steel. **Science and Technology of Welding and Joining**, v. 11, n. 5, p. 526–537, 2006. ISSN 1362-1718.

NANDAN, R.; ROY, G. G.; LIENERT, T. J.; DEBROY, T. Three-dimensional heat and material flow during friction stir welding of mild steel. **Acta Materialia**, v. 55, n. 3, p. 883–895, 2007. ISSN 13596454.

NIEKERK, C. J. V.; TOIT, M. D.; ERWEE, M. W. Sensitization of aisi 409 ferritic stainless steel during low heat input arc welding. **Welding in the World**, v. 56, n. 5-6, p. 54–64, 2012. ISSN 00432288.

O'BRIEN, R. L.; SOCIETY., A. W. **Welding handbook. Volume 2, Volume 2,**. Miami, Fla.: American Welding Society, 1991. ISBN 0871713543 9780871713544.

PACKER, S. Tool geometries and tool materials for friction stir welding high melting temperature materials. In: **Proceedings of the 1st International Joint Symposium on Joining and Welding**. Elsevier, 2013. p. 473–476. Disponível em: <http://dx.doi.org/10.1533/9781782421641.473https://linkinghub.elsevier.com/retrieve/pii/B9781782421634500778>.

PADMANABAN, G.; BALASUBRAMANIAN, V. Selection of FSW tool pin profile, shoulder diameter and material for joining AZ31B magnesium alloy - An experimental approach. **Materials and Design**, Elsevier Ltd, v. 30, n. 7, p. 2647–2656, 2009. ISSN 02641275.

PANKAJ, P.; TIWARI, A.; BISWAS, P.; RAO, A. G.; PAL, S. A three-dimensional heat transfer modelling and experimental study on friction stir welding of dissimilar steels. **Journal of the Brazilian Society of Mechanical Sciences and Engineering**, Springer Berlin Heidelberg, v. 42, n. 9, 2020. ISSN 18063691.

PARK, N.; SHIBATA, A.; TERADA, D.; TSUJI, N. Flow stress analysis for determining the critical condition of dynamic ferrite transformation in 6Ni-0.1C steel. **Acta Materialia**, Acta Materialia Inc., v. 61, n. 1, p. 163–173, 2013. ISSN 13596454.

PARK, S. H.; SATO, Y. S.; KOKAWA, H.; OKAMOTO, K.; HIRANO, S.; INAGAKI, M. Corrosion properties in friction stir welded 304 austenitic stainless steel. **Welding Research Abroad**, v. 52, n. 4, p. 1–6, 2006. ISSN 00432318.

PARK, S. H. C.; SATO, Y. S.; KOKAWA, H.; OKAMOTO, K.; HIRANO, S.; INAGAKI, M. Rapid formation of the sigma phase in 304 stainless steel during friction stir welding. **Scripta Materialia**, v. 49, n. 12, p. 1175–1180, 12 2003. ISSN 13596462.

PARK, S. H. C.; SATO, Y. S.; KOKAWA, H.; OKAMOTO, K.; HIRANO, S.; INAGAKI, M. Corrosion resistance of friction stir welded 304 stainless steel. **Scripta Materialia**, v. 51, n. 2, p. 101–105, 7 2004. ISSN 13596462. Disponível em: <https://linkinghub.elsevier.com/retrieve/pii/S1359646204002143>.

PATEL, N.; BHATT, K.; MEHTA, V. Influence of Tool Pin Profile and Welding Parameter on Tensile Strength of Magnesium Alloy AZ91 During FSW. **Procedia Technology**, Elsevier B.V., v. 23, p. 558–565, 2016. ISSN 22120173. Disponível em: <http://linkinghub.elsevier.com/retrieve/pii/S2212017316300640>.

PATEL, N. P.; PARLIKAR, P.; DHARI, R. S.; MEHTA, K.; PANDYA, M. Numerical modelling on cooling assisted friction stir welding of dissimilar Al-Cu joint. **Journal of Manufacturing Processes**, Elsevier, v. 47, n. September, p. 98–109, 2019. ISSN 15266125. Disponível em: <https://doi.org/10.1016/j.jmapro.2019.09.020>.

PATEL, V.; LI, W.; VAIRIS, A.; BADHEKA, V. Recent Development in Friction Stir Processing as a Solid-State Grain Refinement Technique: Microstructural Evolution and Property Enhancement. **Critical Reviews in Solid State and Materials Sciences**, Taylor & Francis, v. 44, n. 5, p. 378–426, 2019. ISSN 15476561.

PICKERING, F. B.; FB, P. PHYSICAL METALLURGY OF STAINLESS STEEL DEVELOPMENTS. 1976.

PISTORIUS, P. G. H.; ROOYEN, G. T. van. Composition and properties of ferritic stainless steels with good weldability. **Welding in the World / Le Soudage dans le Monde**, v. 36, p. 65–72, 1995.

PRADEEP, A. A Review on Friction Stir Welding of Steel. **International Journal of Engineering Research and Development**, v. 3, n. 11, p. 2278–67, 2012. ISSN 1662-8985.

QIAN, J.; LI, J.; SUN, F.; XIONG, J.; ZHANG, F.; LIN, X. An analytical model to optimize rotation speed and travel speed of friction stir welding for defect-free joints. **Scripta Materialia**, Acta Materialia Inc., v. 68, n. 3-4, p. 175–178, 2013. ISSN 13596462.

RANJAN, R.; KHAN, A. R.; PARIKH, C.; JAIN, R.; MAHTO, R. P.; PAL, S.; PAL, S. K.; CHAKRAVARTY, D. Classification and identification of surface defects in friction stir welding: An image processing approach. **Journal of Manufacturing Processes**, The Society of Manufacturing Engineers, v. 22, p. 237–253, 2016. ISSN 15266125.

REYNOLDS, A. P.; TANG, W.; GNAUPEL-HEROLD, T.; PRASK, H. Structure, properties, and residual stress of 304L stainless steel friction stir welds. **Scripta Materialia**, v. 48, n. 9, p. 1289–1294, 2003. ISSN 13596462.

RICKETT, R. L.; WHITE, W. F.; WALTON, C. S.; BUTLER, J. C. ISOTHERMAL TRANSFORMATION, HARDENING, AND TEMPERING OF 12-PERCENT CHROMIUM STEEL. **TRANSACTIONS OF THE AMERICAN SOCIETY FOR METALS**, METALLURGICAL SOC AMER INST MINING METALL PETROL ENG INC 420 COMMONWEALTH DR˜..., v. 44, p. 138–175, 1952.

ROLLETT, A.; HUMPHREYS, F. J.; ROHRER, G. S.; HATHERLY, M. **Recrystallization and Related Annealing Phenomena**. [S.l.]: Elsevier Science, 2004. ISBN 9780080540412.

SANTACREU, P.; SAEDLOU, S.; FAIVRE, L.; ACHER, A.; LESEUX, J. Ferritic stainless steel grade with improved durability for high temperature exhaust manifold. **SAE 2011 World Congress and Exhibition**, 2011. ISSN 2688-3627.

SATHIYA, P.; ARAVINDAN, S.; HAQ, A. N. Effect of friction welding parameters on mechanical and metallurgical properties of ferritic stainless steel. **The International Journal of Advanced Manufacturing Technology**, v. 31, n. 11-12, p. 1076–1082, 1 2007. ISSN 0268-3768. Disponível em: <http://link.springer.com/10.1007/s00170-005-0285-5>.

SATO, Y. S.; NELSON, T. W.; STERLING, C. J. Recrystallization in type 304L stainless steel during friction stirring. **Acta Materialia**, v. 53, n. 3, p. 637–645, 2005. ISSN 13596454.

SATO, Y. S.; NELSON, T. W.; STERLING, C. J.; STEEL, R. J.; PETTERSSON, C. O. Microstructure and mechanical properties of friction stir welded SAF 2507 super duplex stainless steel. **Materials Science and Engineering A**, v. 397, n. 1-2, p. 376–384, 2005. ISSN 09215093.

SCHMIDT, H.; HATTEL, J.; WERT, J. An analytical model for the heat generation in friction stir welding. **Modelling and Simulation in Materials Science and Engineering**, IOP Publishing, v. 12, n. 1, p. 143–157, nov 2003. Disponível em: <https://doi.org/10.1088/0965-0393/12/1/013>.

SEIDEL, T. U.; REYNOLDS, A. P. Two-dimensional friction stir welding process model based on fluid mechanics. **Science and Technology of Welding and Joining**, v. 8, n. 3, p. 175–183, 2003. ISSN 1362-1718. Disponível em: <http://www.tandfonline.com/doi/full/10.1179/136217103225010952>.

SELLARS, C. M.; TEGART, W. J. M. Hot Workability. **International Metallurgical Reviews**, v. 17, n. 1, p. 1–24, 1972. ISSN 0367-9020.

SELLO, M. P.; STUMPF, W. E. Laves phase precipitation and its transformation kinetics in the ferritic stainless steel type AISI 441. **Materials Science and Engineering A**, Elsevier B.V., v. 528, n. 3, p. 1840–1847, 2011. ISSN 09215093.

SHANMUGAM, K.; LAKSHMINARAYANAN, A. K.; BALASUBRAMANIAN, V. Effect of weld metal properties on fatigue crack growth behaviour of gas tungsten arc welded AISI 409M grade ferritic stainless steel joints. **International Journal of Pressure Vessels and Piping**, Elsevier Ltd, v. 86, n. 8, p. 517–524, 2009. ISSN 03080161.

SHEPPARD, T.; WRIGHT, D. S. Determination of flow stress: part1 constitutive equation for aluminum alloys at elevated temperatures. **Metal technology**, June, n. June, p. 215–223, 1979. ISSN 0307-1693.

SILVA, C.; FARIAS, J.; SANT'ANA, H. B. Resistance evaluation of distillation tower welded metal plate linings to corrosion caused by heavy crude oil. **Boletim Tecnico da PETROBRAS**, v. 51, p. 9–35, 2008.

SILVA, C. C.; FARIAS, J. P.; MIRANDA, H. C.; GUIMARÃES, R. F.; MENEZES, J. W.; NETO, M. A. Microstructural characterization of the HAZ in AISI 444 ferritic stainless steel welds. **Materials Characterization**, v. 59, n. 5, p. 528–533, 2008. ISSN 10445803.

SILVA, C. C.; MIRANDA, H. C.; SANT'ANA, H. B. de; FARIAS, J. P. Austenitic and ferritic stainless steel dissimilar weld metal evaluation for the applications as-coating in the petroleum processing equipment. **Materials and Design**, v. 47, p. 1–8, 2013. ISSN 18734197.

SILVA C. C., A. N. J. d. C. S. H. B. F. J. P. ALTERAÇÕES MICROESTRUTURAIS NA ZAC DO AÇO INOXIDÁVEL AISI 410S – EFEITOS SOBRE A RESISTÊNCIA À CORROSÃO. **Rev. Soldag. Insp.**, v. 11, p. 188–199, 2006.

SILVA, Y. C.; ANDRADE, T. C.; OLIVEIRA, F. J. V. J. Experimental and numerical investigation of the influence of the friction stir welding parameters of the AISI 410S ferritic stainless steel joints. 2020.

SILVA, Y. C.; JÚNIOR, F. J. O.; MARCONDES, F.; SILVA, C. C. Analysis of viscosity function models used in friction stir welding. **Journal of the Brazilian Society of Mechanical Sciences and Engineering**, Springer Berlin Heidelberg, v. 42, n. 8, p. 1–13, 2020. ISSN 18063691.

SILVA, Y. C.; JÚNIOR, F. J. O.; SANTOS, J. F. dos; MARCONDES, F.; SILVA, C. Numerical investigation of the influence of FSW parameters on the heat and mass transfer of austenitic stainless steels. **Welding in the World**, 2020. ISSN 18786669.

SMITH, W. F. **Structure and properties of engineering alloys**. 2. ed. [S.l.]: McGraw-Hill, 1993. ISBN 0070591725,9780070591721.

SONG, K. J.; DONG, Z. B.; FANG, K.; ZHAN, X. H.; WEI, Y. H. Cellular automaton modelling of dynamic recrystallisation microstructure evolution during friction stir welding of titanium alloy. **Materials Science and Technology**, v. 30, n. 6, p. 700–711, 2014. ISSN 0267-0836.

SONI, N.; CHANDRASHEKHAR, S.; KUMAR, A.; CHARY, V. R. Defects Formation during Friction Stir Welding: A Review. **International Journal of Engineering and Management Research**, v. 7, p. 121–125, 2017.

SU, H.; WU, C. S.; PITTNER, A.; RETHMEIER, M. Thermal energy generation and distribution in friction stir welding of aluminum alloys. **Energy**, v. 77, p. 720–731, 2014. ISSN 03605442.

SU, Y.; LI, W.; PATEL, V.; VAIRIS, A.; WANG, F. Formability of an AA5083 aluminum alloy T-joint using SSFSW on both corners. **Materials and Manufacturing Processes**, v. 34, n. 15, p. 1737–1744, 2019. ISSN 15322475.

SUNDQVIST, J.; MANNINEN, T.; HEIKKINEN, H. P.; ANTTILA, S.; KAPLAN, A. F. Laser surface hardening of 11% Cr ferritic stainless steel and its sensitisation behaviour. **Surface and Coatings Technology**, Elsevier, v. 344, n. March, p. 673–679, 2018. ISSN 02578972.

TABAN, E.; DELEU, E.; DHOOGE, A.; KALUC, E. Laser welding of modified 12% Cr stainless steel: Strength, fatigue, toughness, microstructure and corrosion properties. **Materials and Design**, Elsevier Ltd, v. 30, n. 4, p. 1193–1200, 2009. ISSN 02641275. Disponível em: <http://dx.doi.org/10.1016/j.matdes.2008.06.030>.

TANG, W.; GUO, X.; MCCLURE, J. C.; MURR, L. E.; NUNES, A. Heat Input and Temperature Distribution in Friction Stir Welding. **Journal of Materials Processing and Manufacturing Science**, v. 7, p. 163–172, 10 1998.

THOMAS, W.; NICHOLAS, E. Friction stir welding for the transportation industries. **Materials & Design**, v. 18, n. 4-6, p. 269–273, 1997. ISSN 02613069.

THOMAS, W. M.; THREADGILL, P. L.; NICHOLAS, E. D. Feasibility of friction stir welding steel. **Science and Technology of Welding and Joining**, v. 4, n. 6, p. 365–372, 1999. ISSN 13621718.

THOMAS, W. M. W.; NORRIS, I.; NICHOLAS, E. D.; NEEDHAM, J. C.; MURCH, M. G.; TEMPLE-SMITH, P.; DAWES, C. J. **Friction stir welding process developments and variant techniques**. 1991. 1–21 p.

THREADGILL, P. L. Terminology in friction stir welding. **Science and Technology of Welding and Joining**, v. 12, n. 4, p. 357–360, 2007. ISSN 13621718.

TOIT, M. D.; ROOYEN, G. T. V.; SMITH, D. An overview of the heat-affected zone sensitization and stress corrosion cracking behaviour of 12 % chromium type 1.4003 ferritic stainless steel. **Welding in the World**, v. 51, n. 9-10, p. 41–50, 2007. ISSN 00432288.

UDAY, M. B.; FAUZI, M. N.; ZUHAILAWATI, H.; ISMAIL, A. B. Advances in friction welding process: A review. **Science and Technology of Welding and Joining**, v. 15, n. 7, p. 534–558, 2010. ISSN 13621718.

ULYSSE, P. Three-dimensional modeling of the friction stir-wedling process. **Int. J. Machine tools \& Manufacture**, v. 42, n. July, p. 1549–1557, 2002. ISSN 0890-6955. Disponível em: <papers2://publication/uuid/5E81FD02-81F7-4313-BC1A-F89895B65F8F>.

VILLARET, V.; DESCHAUX-BEAUME, F.; BORDREUIL, C.; ROUQUETTE, S.; CHOVET, C. Influence of filler wire composition on weld microstructures of a 444 ferritic stainless steel grade. **Journal of Materials Processing Technology**, Elsevier B.V., v. 213, n. 9, p. 1538–1547, 2013. ISSN 09240136.

VITEK, J. M.; DAVID, S. A. Sigma Phase Transformation in Austenitic Stainless Steels. **Welding Journal (Miami, Fla)**, v. 65, n. 4, 1986. ISSN 00432296.

WARMELO, M. van; NOLAN, D.; NORRISH, J. Mitigation of sensitisation effects in unstabilised 12%Cr ferritic stainless steel welds. **Materials Science and Engineering A**, v. 464, n. 1-2, p. 157–169, 2007. ISSN 09215093.

WEN, Q.; LI, W. Y.; WANG, W. B.; WANG, F. F.; GAO, Y. J.; PATEL, V. Experimental and numerical investigations of bonding interface behavior in stationary shoulder friction stir lap welding. **Journal of Materials Science and Technology**, v. 35, n. 1, p. 192–200, 2019. ISSN 10050302.

WILLIAMS, S. W. Welding of airframes using friction stir. **Air & Space Europe**, v. 3, n. 3-4, p. 64–66, 2001. ISSN 12900958.

YADUWANSHI, D. K.; BAG, S.; PAL, S. Numerical modeling and experimental investigation on plasma-assisted hybrid friction stir welding of dissimilar materials. **Materials and Design**, Elsevier Ltd, v. 92, p. 166–183, 2016. ISSN 18734197.

YANG, C. L.; WU, C. S.; LV, X. Q. Numerical analysis of mass transfer and material mixing in friction stir welding of aluminum/magnesium alloys. **Journal of Manufacturing Processes**, v. 32, p. 380–394, 2018. ISSN 15266125.

YOSHIKAWA, G.; MIYASAKA, F.; HIRATA, Y.; KATAYAMA, Y.; FUSE, T. Development of numerical simulation model for FSW employing particle method. **Science and Technology of Welding and Joining**, v. 17, n. 4, p. 225–263, 2012. ISSN 13621718.

ZHANG, H.; LIU, H. Characteristics and Formation Mechanisms of Welding Defects in Underwater Friction Stir Welded Aluminum Alloy. **Metallography, Microstructure, and Analysis**, v. 1, n. 6, p. 269–281, 2012. ISSN 21929262.

ZHANG, H. W.; ZHANG, Z.; CHEN, J. T. The finite element simulation of the friction stir welding process. **Materials Science and Engineering A**, v. 403, n. 1-2, p. 340–348, 2005. ISSN 09215093.

ZHANG, S.; CHEN, G.; LIU, Q.; LI, H.; ZHANG, G.; WANG, G.; SHI, Q. Numerical analysis and analytical modeling of the spatial distribution of heat flux during friction stir welding. **Journal of Manufacturing Processes**, Elsevier, v. 33, n. May, p. 245–255, 2018. ISSN 15266125.

ZHAO, L.; PARK, N.; TIAN, Y.; SHIBATA, A.; TSUJI, N. Combination of dynamic transformation and dynamic recrystallization for realizing ultrafine-grained steels with superior mechanical properties. **Scientific Reports**, Nature Publishing Group, v. 6, n. December, p. 1–11, 2016. ISSN 20452322.

ZHENG, Q.; FENG, X.; SHEN, Y.; HUANG, G.; ZHAO, P. Effect of plunge depth on microstructure and mechanical properties of FSW lap joint between aluminum alloy and nickel-base alloy. **Journal of Alloys and Compounds**, Elsevier Ltd, v. 695, p. 952–961, 2017. ISSN 09258388.

ZHOU, C.; YANG, X.; LUAN, G. Effect of kissing bond on fatigue behavior of friction stir welds on Al 5083 alloy. **Journal of Materials Science**, v. 41, n. 10, p. 2771–2777, 2006. ISSN 00222461.

ZHU, X. K.; CHAO, Y. J. Numerical simulation of transient temperature and residual stresses in friction stir welding of 304L stainless steel. **Journal of Materials Processing Technology**, v. 146, n. 2, p. 263–272, 2004. ISSN 09240136.

ZHU, Y.; CHEN, G.; CHEN, Q.; ZHANG, G.; SHI, Q. Simulation of material plastic flow driven by non-uniform friction force during friction stir welding and related defect prediction. **Materials and Design**, Elsevier Ltd, v. 108, p. 400–410, 2016. ISSN 18734197.

APPENDIX A –   AISI 304 STAINLESS STEEL CONSTANTS - ARTICLE 1

$C_{P-workpiece}(J/kg \cdot K)$	$276 + 0.851 \cdot T - 0.000851 \cdot T^2 + 3 \cdot 10^{-7} \cdot T^3$
$k_{workpiece}(W/m \cdot K)$	$14.3 - 0,00902 \cdot T + 4.52 \cdot 10^{-5} \cdot T^2 - 2,49 \cdot 10^{-8} \cdot T^3$
$\rho_{workpiece}(kg/m^3)$	7200
$P_N(MPa)$	109
$R_s(mm)$	9.53
$R_p(mm)$	3.17
$U_1(mm/s)$	1.693
$C_{P-tool}(J/kg \cdot K)$	$158 + 1.06 \cdot T - 1.63 \cdot T^2$
η	0.5
$k_{tool}(W/m \cdot K)$	$0.367 - 2.29 \cdot T + 1.25 \cdot 10^{-7} \cdot T^2$
$\rho_{tool}(kg/m^3)$	19400
δ	0.7
μ	0.4
$\omega(RPM)$	300
$a_0(s^{-1})$	$1.36 \cdot 10^{35}$
$b_0(s^{-1})$	$8.03 \cdot 10^{26}$
$G(Pa)$	$73.1 \cdot 10^9$
$k_0(Pa)$	$150 \cdot 10^6$
$Q(J/mol)$	$410 \cdot 10^3$
$Q_0(j/mol)$	$91 \cdot 10^3$
λ	0.15
M	7.8
N	5
$C(Pa)$	$132 \cdot 10^6$
$D_0(s^{-1})$	10^8

m_0	2.148
n_0	6
$R(J/mol \cdot K)$	8.3144621

APPENDIX B – TI-6AL-4V ALLOY CONSTANTS - ARTICLE 1

$C_{P-workpiece}(J/kg \cdot K)$ $622 - 0.367 \cdot T - 0.000545 \cdot T^2 + 2.39 \cdot 10^{-8} \cdot T^3$

$k_{workpiece}(W/m \cdot K)$ $19.2 + 0,0189 \cdot T - 1.53 \cdot 10^{-5} \cdot T^2 + 1.41 \cdot 10^{-8} \cdot T^3$

$\rho_{workpiece}(kg/m^3)$ 7200

$\theta(MPa)$ $9.09 \cdot 10^2 + 1.11 \cdot T - 3.05 \cdot 10^{-3} \cdot T^2 + 1.26 \cdot 10^{-6} \cdot T^3$

$P_N(MPa)$ 60.0

$R_s(mm)$ 9.5

$R_p(mm)$ 3.95

$U_1(mm/s)$ 1.6

$C_{P-tool}(J/kg \cdot K)$ $128.3 - 3.279 \cdot 10^{-2} \cdot T + 3.41 \cdot 10^{-6} \cdot T^2$

$k_{tool}(W/m \cdot K)$ $153.5 - 9.56 \cdot 10^{-2} \cdot T + 5.23 \cdot 10^{-5} \cdot T^2$

$\rho_{tool}(kg/m^3)$ 19400

δ_0 0.7

μ_0 0.4

η 0.7

$\omega(RPM)$ 275

$A(s^{-1})$ 229.725

$\alpha(MPa^{-1})$ 0.0066

$Q(J/mol)$ 501000

n 5

P 0.08

APPENDIX C – FERRITIC STAINLESS STEELS CONSTANTS - ARTICLE 2

X	0.025
$R_s(mm)$	11.8
$R_p(mm)$	4.6
δ_0	0.4
μ_0	0.6
η	$0.200 + 3.966 \cdot 10^{-4} \cdot T$
$A(s^{-1})$	$(1.802 \cdot 10^6 + 1.742 \cdot 10^8 \cdot X - 6.503 \cdot 10^7 \cdot X^2) \cdot 10^{-6n}$
$\alpha(MPa^{-1})$	$(1.068 + 1.702 \cdot 10^{-4} \cdot T - 2.808 \cdot 10^{-7} \cdot T^2) \cdot 10^{-6}$
$Q(J/mol)$	49809
λ	1